WHERE PLANETS END AND STARS BEGIN: TRANSITING BROWN DWARFS AS EMPIRICAL TRACERS OF FORMATION

By

Noah Vowell

A DISSERTATION

Submitted to
Michigan State University
in partial fulfillment of the requirements
for the degree of

Astrophysics and Astronomy—Doctor of Philosophy

2026

ABSTRACT

Despite over three decades of exoplanet science and an order of magnitude more for stellar binaries, we have still not definitively constrained the transition between planetary and stellar formation. A key population for uncovering that transition is the brown dwarfs because they occupy the mass regime between planets and stars. Currently planets, brown dwarfs, and stars are distinguished via theoretically defined mass thresholds based on where fusion occurs. These definitions inform our understanding of their interior physics, however, they don't cleanly map onto distinct formation mechanisms. Planets form through core accretion while stars form via collapse/fragmentation. The brown dwarfs encompass the region where the tail-ends of these formation mechanisms overlap, but it is not well understood exactly where that transition takes place. This thesis aims to address this problem by utilizing a newly cultivated population of brown dwarfs that transit their host stars.

In this thesis, we first present our efforts to expand the population of transiting brown dwarfs in order to begin making population level inferences about their formation and evolution. We do this through targeted discovery and characterization of new brown dwarf companions detected by NASA's Transiting Exoplanet Survey Satellite. We outline the discovery and characterization of 12 new transiting brown dwarf and low-mass stellar companions, including a particularly unique brown dwarf system: HIP 33609. With a newly expanded population of transiting brown dwarfs, we then analyze the eccentricity and metallicity distributions, finding that they do not support a 43 M_J transition as suggested by previous literature. We establish this system as one of the most extreme discoveries to date and confirm its membership in the previously unknown stellar association, MELANGE-6. We then measure the sky-projected orbital obliquity of HIP 33609 and find that the brown dwarf resides in a low obliquity orbit. HIP 33609 b's architecture allows us to put strong constraints on its formation and evolutionary pathway since it is most consistent with a stellar-like formation mechanism followed by coplanar high eccentricity migration. We provide insight into trends emerging in the obliquity distribution of brown dwarfs, showing that they may be indicative of a quiescent evolutionary history. We conclude by summarizing our results that rule out 43 M_J as the transition point between planetary and stellar formation. We instead show

evidence that most brown dwarfs appear to form through a stellar mechanism suggesting a much lower boundary. Finally we lay out the path forward for making more robust inferences about brown dwarf formation and evolution with current facilities like Gaia and the James Webb Space Telescope as well as next generation observatories like the Roman Space Telescope and Vera Rubin observatory.

TABLE OF CONTENTS

LIST OF ABBREVIATIONS

BD	Brown Dwarf
RV	Radial Velocity
SED	Spectral Energy Distribution
2MASS	2-Micron All-Sky Survey
DENIS	Deep Near-Infrared Sky survey
SDSS	Sloan Digital Sky Survey
CoRoT	Convection, Rotation and planetary Transits
KELT	Kilodegree Extremely Little Telescope
TESS	Transiting Exoplanet Survey Satellite
Gaia DR4	Gaia Data Release 4
LDC	Limb Darkening Coefficient
JWST	James Webb Space Telescope

CHAPTER 1

INTRODUCTION

1.1 What are Brown Dwarfs?

Brown dwarfs (BDs) are objects that bridge the gap in mass between planets and stars. These three classes are physically distinguished from each other based on the presence, and type, of nuclear fusion that takes place in their cores. Planets, the least massive of these, do not undergo nuclear fusion of any kind and derive their luminosity solely from residual and external heat. At the high-mass end, stars grow massive enough to ignite and sustain hydrogen fusion in their cores. The BDs also ignite nuclear fusion similar to stars, however, they only burn deuterium, a heavy isotope of hydrogen making up roughly 0.002% of the primordial hydrogen in the universe. This period is also is generally short-lived, lasting about $10^6 - 10^8$ years depending on the BD's mass (Burrows et al., 2001). Once deuterium burning is exhausted, the associated nuclear energy generation ceases, and the pressure support it provides against gravitational contraction is lost. The shutting off of deuterium fusion signifies the transition to the final stage of a BD's life where it will slowly cool and contract for the rest of cosmic time so long as it is unperturbed. This cooling causes BDs to decrease in temperature and luminosity over time. As a result, any given temperature and luminosity does not uniquely determine the mass of a BD without an independent age constraint. Young, low-mass BDs can exhibit the same effective temperatures and luminosities as older, more massive ones BDs (Baraffe et al., 2003; Phillips et al., 2020). This fundamental degeneracy between mass, temperature, luminosity, and age is displayed in Figure 1.1.

Once deuterium fusion has ended, long-term structural evolution is governed by a transition from thermal pressure support to electron degeneracy pressure support. That source of internal pressure also helps distinguish the BDs from planets, where Coulomb effects dominate, and stars, which are supported by thermal gas pressure. As BDs cool and contract, their interiors become increasingly degenerate leading to counterintuitive physical properties. One of the most striking of these properties is that BD radii are only weakly dependent on the mass. Despite spanning nearly an order of magnitude in mass, BDs span a comparatively narrow range in radius remaining

close to the size of Jupiter. The correlation mass and radius even inverts with more the massive brown dwarfs being physically smaller than their less massive counterparts at late times when the interior becomes sufficiently degenerate. Thus there is an analogous degeneracy in radius to the one displayed in 1.1.

Because the main distinguishing feature of a BD is the presence of deuterium fusion, but not fully-fledged hydrogen fusion, one can constrain the parameter space that is "BDs" by constraining the fundamental limits of these fusion processes. In other words, the lower limit of deuterium fusion marks the transition from planets to BDs, while the lower limit of hydrogen fusion marks the transition from BDs to stars. These transition points are generally accepted to occur at 13 M_J and 80 M_J respectively. However, the mass off a celestial object is not the only property that governs the ignition of fusion in its core. Fusion only ignites under sufficient central temperature and pressure conditions which are also sensitive to the object's metallicity, opacity, and even rotation (albeit minorly). These effects blur the boundaries between planets, BDs, and stars making the classification of objects near edges of each regime difficult (Spiegel et al., 2011; Baraffe et al., 1998).

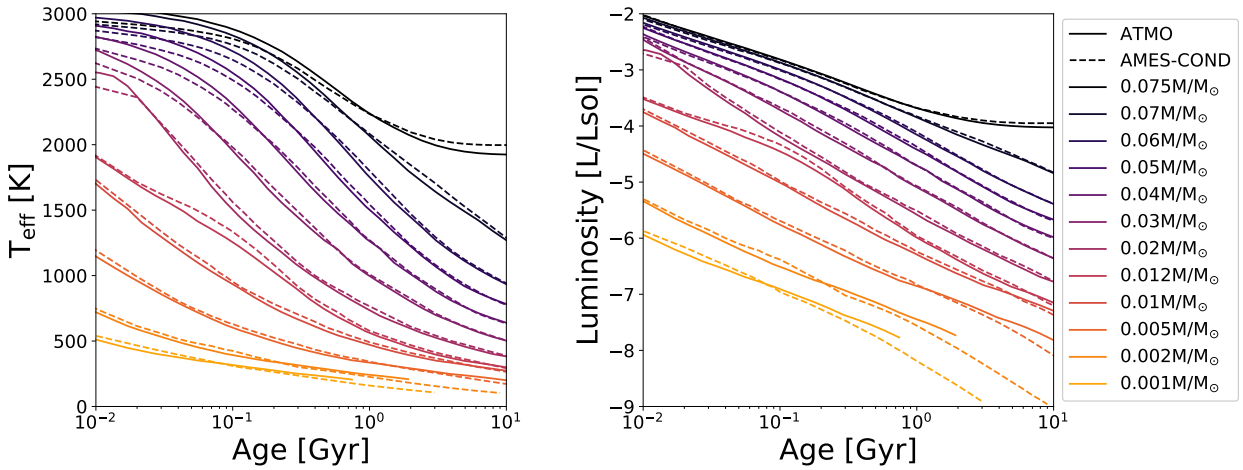

Figure 1.1 Adapted from Figure 7 of Phillips et al. (2020). Evolutionary models for brown dwarfs in effective temperature versus age (Left), and luminosity versus age (Right). Colors correspond to brown dwarfs of different masses. Solid and dashed lines show the models from Phillips et al. (2020) and Baraffe et al. (2003) respectively. The degeneracies between mass-temperature-luminosity-age are clearly shown. Note that there is an equivalent degeneracy in radius.

1.2 History of Brown Dwarfs

Celestial objects too small to ignite sustained hydrogen fusion in their cores were theorized as early as early as Chandrasekhar (1939). However, it wasn't until 1963 that the fundamental properties of such strange objects would be begin to be explored in more detail when Kumar (1963) presented the first framework for the structure of these substellar objects and correctly predicted many of the key BD features that we know of today. Kumar (1963), and others, initially referred to these objects as "black dwarfs" until Jill Tarter suggested the term used today (brown dwarfs) in her PhD thesis to distinguish them from the theoretical end stage of white dwarfs which were already generally referred to as black dwarfs (Tarter, 1975).

1.2.1 The First Directly Imaged Brown Dwarfs

Several decades would pass before the objects of Chandrasekhar's and Kumar's theories would be definitively found. The first unambiguous BD discoveries were published in 1995 with the discovery of Teide 1 (Rebolo et al., 1995) and Gliese 229B (Oppenheimer et al., 1995), a young brown dwarf in the Pleiades and a brown dwarf companion to an M-dwarf respectively. These discoveries kicked off a period of rapid BD discovery, primarily from the 2-Micron All-Sky Survey (2MASS; Kirkpatrick et al., 1997), Deep Near-Infrared Sky survey (DENIS; Delfosse et al., 1997), and Sloan Digital Sky Survey (SDSS; Strauss et al., 1999; Fan et al., 2000). Because these BDs were discovered via direct imaging, they were characterized based on what we could directly observe from their own light via photometry and spectroscopy. We could directly measure BD temperatures, luminosities, and atmospheric compositions, however, it remains difficult derive unobservable parameters from models. This is due to the aforementioned degeneracies inherent to BDs making it difficult to calibrate our substellar evolutionary models since independent constraints mass, temperature, luminosity, and age are all required.

This early work on directly imaged BDs in the field led to the creation of several new spectral classes beyond the M-dwarfs (which mark the end of the main sequence). These new spectral classes would distinguish progressively cooler objects by identifying key transitions the chemical compositions of their atmospheres. The hottest and most luminous BDs immediately following the

M-dwarfs would be named L-dwarfs with effective temperatures ranging from $\sim 1400 - 2200$ K. These BDs have atmospheres dominated by alkali metals and CO similar to the M-dwarfs, however, they vitally lack the M-dwarfs' characteristic TiO and VO lines forming their own distinct spectral class (Kirkpatrick et al., 1999). T-dwarfs make up the next spectral class with effective temperatures $\sim 500 - 1400$ K. These lower temperatures come with weakening alkali lines and a shift in the carbon chemistry as CH_4 becomes the dominant carbon bearing molecule (Burgasser et al., 2002). Finally, Y-dwarfs make up the coolest spectral class with objects with temperatures < 500 K. They retain strong CH_4 absorption but are distinguished from the T-dwarfs by the emergence of NH_3 features (Cushing et al., 2011).

1.2.2 Brown Dwarfs in the Era of Exoplanet Discovery

The early work on isolated/widely-separated BDs in the field driven by direct imaging and spectroscopy established BDs as a distinct physical population. However, parallel to much of this work, exoplanet science was taking off with the discovery of the first exoplanet, 51 Pegasi b (Mayor & Queloz, 1995). This discovery and the significant majority of the ones that followed for several years were made by observing the gravitational effect that a nearby orbiting planet has on its host star. The planet and the host star orbit their center of mass, and (so long as the orbit isn't being viewed face-on) the radial component of the stars motion can be measured through the Doppler effect. As the star moves towards and away from us throughout its orbit, its light will be blue-shifted and red-shifted respectively, where the magnitude and direction of the shift in wavelength is dependent on the magnitude and direction of the radial velocity (RV). Tracking the radial velocity over time produces an RV curve from which several parameters of the system can be directly measured or inferred from Kepler's 3rd Law. That is:

$$\frac{M_p^3 \sin^3 i}{(M_p + M_*)^2} = \frac{PK^3}{2\pi G}(1 - e^2)^{3/2} \tag{1.1}$$

where M_p, M_* are the masses of the planet and star, i is the orbital inclination, P is the orbital period, K is the semi-amplitude of the RV curve, G is the gravitational constant, and e is the orbital eccentricity.

The pioneers of exoplanet discovery showed how this technique could be a powerful way to discover nearby, low-mass companions to stars, where the detectability of a companion was directly related the semi-amplitude K, and period P of the RV curve. Too small an amplitude or too long an orbital period would result in an RV curve indistinguishable from a flat line, biasing the RV detections to higher masses and shorter orbital periods. The early RV surveys capable of detecting giant planet companions would thus be sensitive to more massive companions as well, namely BDs and low-mass stars. And while these surveys were successful in discovering giant planets and low-mass stars, there was a noticeable dearth of BD mass companions Latham et al. (1998). Despite the fact that close-in BDs seemed intrinsically rare, several dozens of them would still be discovered via RVs opening the way for true demographic studies. The deficit of short-period BDs would be more rigorously constrained and dubbed "the brown dwarf desert" raising questions about whether these objects represent the most extreme cases of the planetary population or a failed extension of the stellar binary population (Ma & Ge, 2014).

While these early RV samples enabled statistical studies on BD demographics, more detailed characterization of any individual system remained difficult. Further characterization was primarily held back by another fundamental degeneracy between the companion mass and inclination of its orbit relative to the line of sight which could not be solved by RVs alone. However, in systems where the orbit of the companion is edge-on, we should see that companion pass in front of its star from our line-of-sight once per orbital period. This event, called a transit, would definitively constrain the inclination of the orbit, breaking the mass-inclination degeneracy. Not only that, but a transit event would also allow observers to constrain other important systematic properties such as the impact parameter of the orbit, the host star's density, and the relative size of the companion. The combination of these two methods provide a much more complete understanding of the companion's physical and architectural properties than either method can accomplish on its own. While both methods only constrain mass and radius of the companion relative to its host star, it typically trivial to turn these into true mass and radius measurements by constraining the host

star's properties through its spectral energy distribution[1] (SED).

The wealth of additional information provided by the transit method, comes with the trade-off that relatively few systems possess the precise architecture required in order to observe a transit. Therefore, when exoplanet scientists began implementing the first transit surveys in the early 2000s, they were sacrificing their overall yield of exoplanet detections in exchange for the ability to more rigorously characterize each individual system. Once again, these techniques would apply at least equally as well to BD discovery. Since BD radii are only weakly dependent on their mass (as mentioned above) their sizes are comparable to those of giant planets, making them easily detectable for any exoplanet transit surveys. In fact, giant planets, BDs, and low-mass stars are all approximately 1 Jupiter radius making them indistinguishable from transits alone. Only a mass constraint from RVs can allow one to distinguish between these three objects.

While the early ground-based transit surveys showed that detecting Jupiter-sized companions was possible, none would be discovered until the first space-based transit survey when the CoRoT (Convection, Rotation and planetary Transits) space telescope (Auvergne et al., 2009) discovered CoRoT-3b (Deleuil et al., 2008). Shortly after, the ground-based Kilodegree Extremely Little Telescope (KELT) survey discovered KELT-1 b, a $\sim 27\ M_J$ brown dwarf in a 1.2 day orbit around a mid-F star (Siverd et al., 2012). KELT-1 b became one of the most studied BD systems, highlighting the value of characterizing the secondary eclipse[2] in addition to the transit. Follow-up observations of KELT-1 b's secondary eclipse enabled the first detailed constraints on the atmospheric properties of a transiting BD, demonstrating that eclipse measurements could constrain their atmospheric circulation and heat redistribution in ways analogous to studies of hot Jupiters (e.g., Beatty et al., 2014).

The launch of NASA's flagship exoplanet transit hunter Kepler (Borucki et al., 2010) and ongoing ground-based surveys would continue to discover only a handful of transiting BDs over

[1]Fitting luminosity measurements at various different wavelengths to the modeled stellar SEDs provides the bolometric luminosity and effective temperature of the host star, enabling determination of the stellar radius through the Stefan–Boltzmann law and the mass via stellar evolutionary models.

[2]The secondary eclipse occurs when the companion passes behind the host star. The primary eclipse is typically referred to as a transit when referring to substellar companions.

the next decade. This apparent rarity of short-period transiting BDs would appear consistent with the idea of the "brown dwarf desert" from RV studies, however, the launch of NASA's Transiting Exoplanet Survey Satellite (*TESS* ; Ricker et al., 2015) mission would provide some vital context to this picture.

By the time *TESS* launched in April 2018, only $\sim$ 15 transiting BDs had been discovered compared to the $>$ 100 RV detected BDs. *TESS* revolutionized the search for transiting BDs, providing the initial detection of nearly every transiting BD discovered since its launch. Today, $\sim$ 70 are known, due in part to this work. The explosion in transiting BD discoveries from *TESS* is likely due to a combination of many factors, but the most important of which are *TESS*'s unparalleled sky coverage and its focus on nearby, brighter stars. Ground-based surveys had also searched nearby stars but lacked the sheer amount of sky coverage required in order to find these rare objects in any significant quantities. On the other hand, most of Kepler's target stars were had brightness $V > 13$ making follow-up very difficult. That is, while Kepler surely *detected* many transiting BDs with its exquisite photometric precision, the host stars were simply too faint to gather the RVs required to confirm a BD mass companion rather than a giant planet or low-mass star.

1.3 Brown Dwarfs as Big Planets and Small Stars

The growing number of BD companions to FGK stars revealed that the companion mass function is not just a smooth continuation of the planetary or stellar mass regimes, but rather some combination of the two. This has lead many BD astronomers to suggest that we redefine the BDs based on whether they form like planets or like stars (Burrows et al., 2001; Chabrier et al., 2014; Carmichael et al., 2021). While this idea is enticing, it necessitates being able to observationally differentiate BDs based on their formation pathways. Something that remains challenging even today.

1.3.1 Brown Dwarf Formation Mechanisms

A key distinguishing feature between planets and stars (aside from their mass regimes) is their formation mechanisms. Generally, they can be split up into two distinct pathways: A "bottom-up" approach that forms less massive bodies (i.e. planets) via core accretion (Pollack et al., 1996) and

a "top-down" approach that forms more massive bodies (i.e. stars) via direct gravitational collapse, either within a circumstellar disk or at the core scale (Adams et al., 1989; Bate, 2012; Kratter & Lodato, 2016). In this picture, the BDs encompass a region where the tail-ends of these formation mechanisms overlap with each other, but it is generally not well understood exactly where the transition occurs between planet-like and star-like formation.

Planet formation theory entails the rapid formation of a massive core via accretion of solid material in the circumstellar disk, a process generally referred to as core accretion. If sufficient material is accreted before the gas disk disperses, then a runaway gas accretion phase occurs resulting in the formation of a giant planet. The upper limit for the mass of these planets is ultimately dependent on the availability of gas that it may accrete. Thus, the upper mass limit is sensitive to the fundamental properties of the disk that govern the availability of the gas such as the disk mass, viscosity, and lifetime (Mordasini et al., 2009). Core accretion models generally predict that the formation of giant planets becomes inefficient in the range of $5 - 20\ M_J$ (Mordasini et al., 2012). This framework also predicts a strong dependence on the metallicity of the host star, since the formation of a massive core is dependent on the availability of solid material in the circumstellar disk. This idea is consistent with the long established giant planet-metallicity correlation (Gonzalez, 1997; Santos et al., 2003; Fischer & Valenti, 2005).

Stellar formation theory on the other hand, forms objects through direct gravitational collapse and fragmentation. The lowest mass stellar companions (e.g. M-dwarfs and massive BDs) are thought to form through hierarchical fragmentation of the protostellar core and/or fragmentation of the disk (McKee & Ostriker, 2007). Fragmentation occurs in a collapsing cloud only when that cloud can efficiently cool, radiating away the energy generated by compressional heating on a dynamical timescale. But, as fragmentation and collapse progresses, density continues to increase causing a corresponding increase in optical depth. This ends up extending the radiative cooling timescale as collapse and fragmentation occur until it exceeds the dynamical timescale of the fragment. Once this happens, fragmentation is now longer possible setting a lower limit on the mass of the fragment, and thus the object it forms (Low & Lynden-Bell, 1976; Rees, 1976). The

lower limit for this process is predicted to be between $1 - 5\ M_J$ (Whitworth & Stamatellos, 2006).

Clearly, these fundamental limits on planet and stellar formation overlap. Core accretion can theoretically produce objects upwards of 20 M_J, whereas star formation can even produce Jupiter analogs. While understanding the theoretical limits of these processes is relatively straightforward, tuning their relative efficiencies in this extreme mass regime remains challenging. Thus it's still unclear which pathway is the dominant formation pathway in this overlapping mass regime. Determining the dominant formation mechanism as a function of companion mass would provide empirical constraints on where planet formation ends and where star formation begins, which can be fed back into their respective models. This unresolved question is what ultimately motivates this thesis: to constraint the transition between planet to star formation.

1.3.2 Brown Dwarf Properties as Tracers of Formation

Brown dwarfs occupy this mass range where planetary and stellar formation intersect, and vitally, the fusion-based boundaries that distinguish them from planets and stars are not directly linked to these formation pathways. This can make them powerful probes for tracing the physical boundary between the planetary and stellar regimes by identifying observable properties that can be traced back to one formation mechanism over the other. Properties like orbital architecture, mass-ratio, and host star composition are expected to have distinct distributions for planetary versus stellar companions. For example, stellar binaries display a larger variance in eccentricity than giant planets do (Moe & Di Stefano, 2017; Rodriguez et al., 2023). Their host stars also tend to have roughly solar metallicities, whereas planet hosts are noticeably more metal-rich (Moe & Di Stefano, 2017; Fischer & Valenti, 2005). These predicted differences provide a framework for identifying where the dominant formation mechanism changes, and several studies have attempted to leverage them to empirically constrain the planetary-stellar boundary.

For example, Grether & Lineweaver (2006) analyzed a sample of all known RV companions to FGK stars at the time with $P_{orb} < 5$ years. Their 198 total companions ranged in mass from $10^{-3}\ M_\odot < M_2 < 10^{0}\ M_\odot$. That is approximately $1\ M_J < M_2 < 10^{3}\ M_J$. They found that the companion mass function has a significant deficit in the BD mass regime centered at $M_2 = 31^{+25}_{-15}\ M_J$

(see, Figure 1.2). This study served as one of the earliest attempts at quantifying the BD desert, implying that companions on opposite sides of the desert had distinct formation and evolutionary mechanisms.

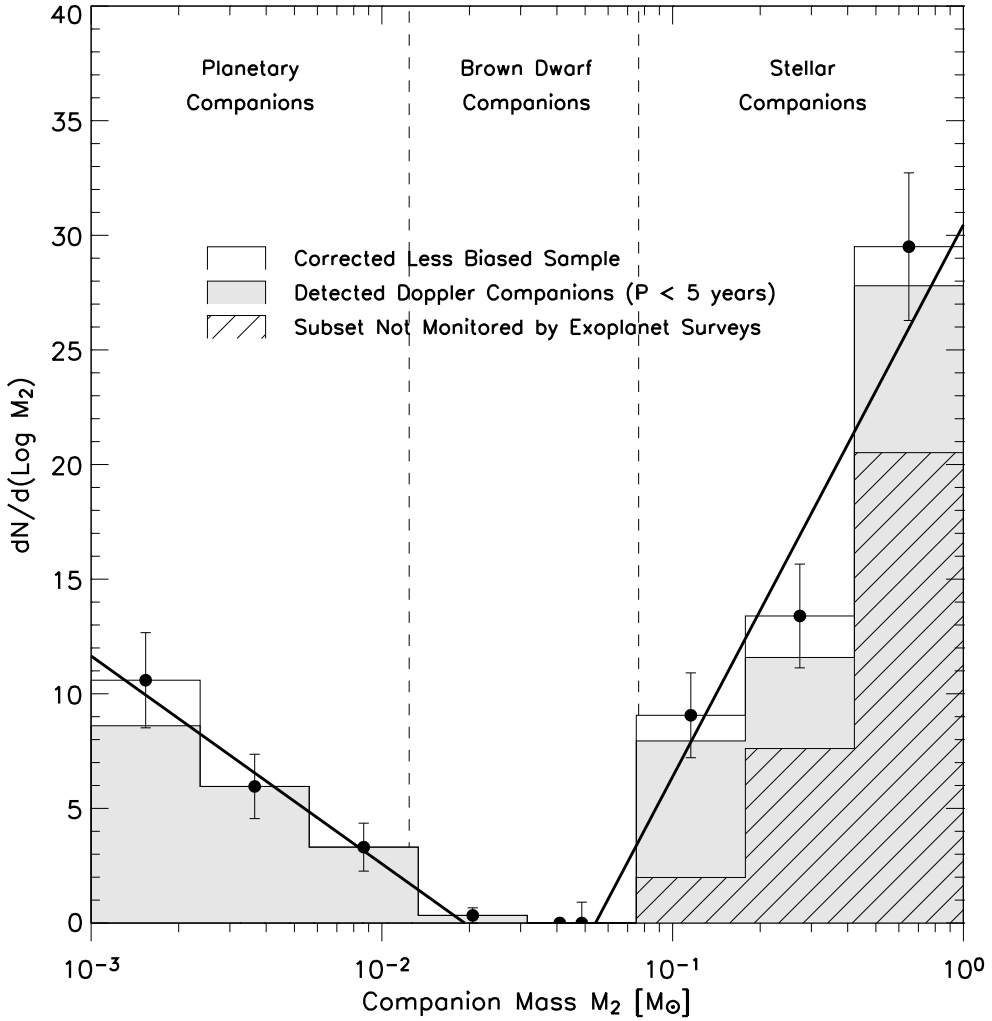

Figure 1.2 Adapted from Figure 9 of Grether & Lineweaver (2006). Histogram of the companions to Sun-like stars closer than 50 pc plotted against mass. The trough of the BD desert is clearly shown at 10^{-2} – 10^{-1} $M_{\odot}$ representing the first quantitative estimate for the transition between planets and stars.

Ma & Ge (2014) conducted a similar analysis nearly a decade later with a sample of all RV detected companions ranging from 10 $M_J < M_2 < 100$ M_J. They once again recovered the BD desert placing tighter constraints on minimum of the companion mass function: $M_{2,min} = 43^{+14}_{-23}\, M_J$. They also noticed a distinct transition in the eccentricity distribution at the same location (see, Figure

1.3). BDs with masses $M_2 < 43\ M_J$ displayed similar eccentricities to giant planets, whereas those with masses $M_2 > 43\ M_J$ more closely resembled stellar binaries. The authors interpreted these trends as evidence of a transition from a core accretion dominated regime to a fragmentation dominated one.

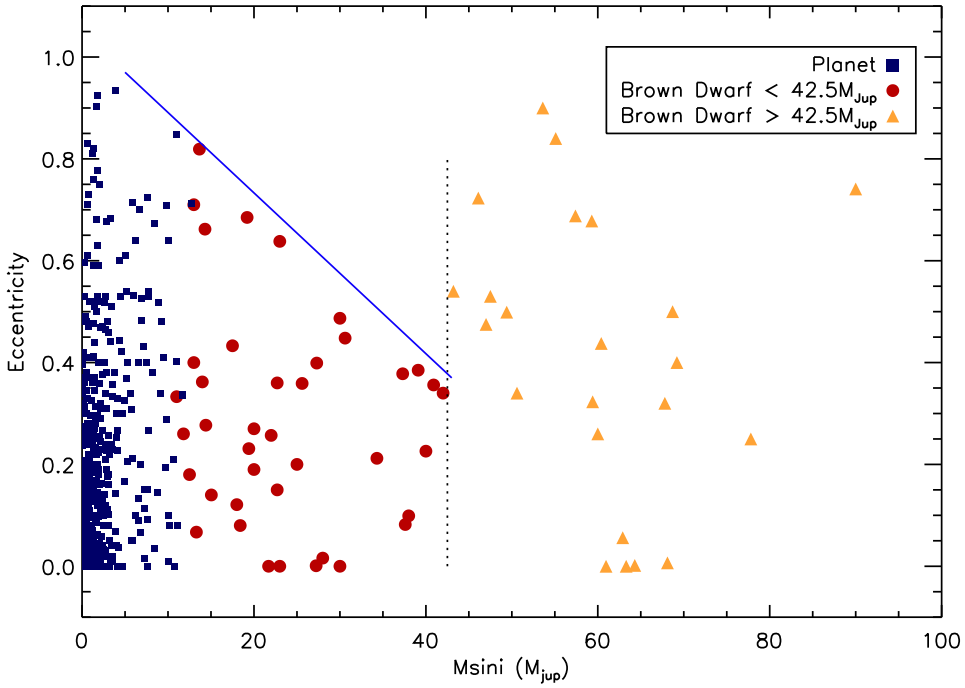

Figure 1.3 Adapted from Figure 5 of Ma & Ge (2014). Orbital eccentricity versus $M \sin i$ for RV companions to Sun-like stars. Blue boxes depict planetary companions, red circles depict low mass BDs and yellow triangles represent high-mass BDs. The blue solid line is a qualitative guide for the low-mass eccentricity trend and the vertical dashed line at 42.5 M_J represents the break in the eccentricity trend. Ma & Ge (2014) claim that the change in the eccentricity distribution at 42.5 M_J is indicative of the transition from planetary to stellar formation.

The transiting BD discoveries of the 2010's opened up a new sample with better characterized companions from which we could test our understanding of BD formation. Schlaufman (2018) compiled a sample of the 27 known transiting companions with masses $10\ M_J < M_2 < 300\ M_J$ to analyze the distribution of host star metallicities. The study's focus on transiting systems ensured no significant bias from the mass-inclination degeneracy present in RV-only data as well as low contamination since observing mutually consistent RV and transit signals rules out nearly all sources of false positives for massive companions. Schlaufman (2018) found that the well-known planet-metallicity correlation (Gonzalez, 1997; Santos et al., 2003; Fischer & Valenti, 2005) significantly

weakened above $10 - 20\ M_J$ implying a significant drop-off in the efficiency of core accretion and the onset of fragmentation as the dominant formation mechanism.

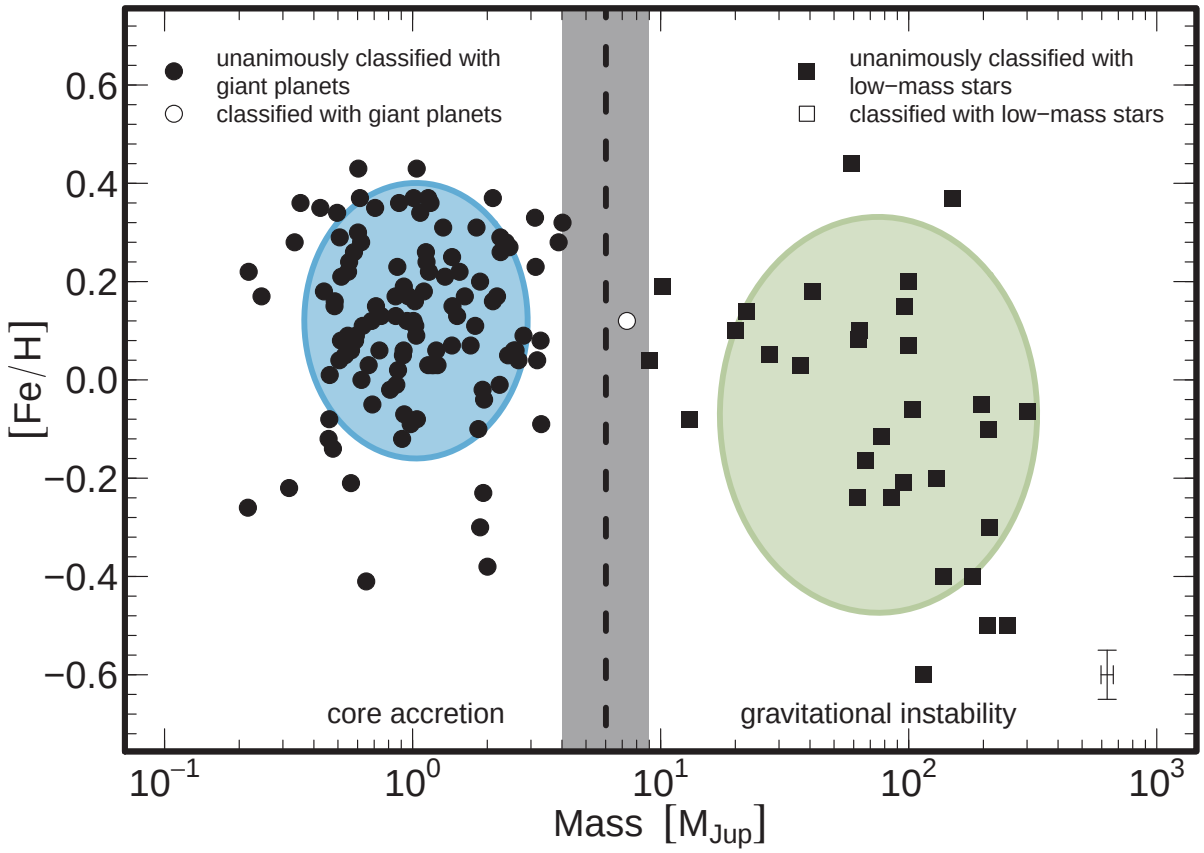

Figure 1.4 Adapted from Figure 1 of Schlaufman (2018). Metallicity versus companion mass for all transiting companions between $10^{-1}\ M_J - 10^3\ M_J$. Solid symbols represent objects that were unanimously classified by their clustering analysis as giant planets (circles) or low-mass stars (boxes), while open symbols represent systems where the classification was not unanimous. The gray shaded region separates the unanimous classification regions and the black dashed line is the midpoint of that region. The blue and green regions are the best fit two-component Gaussian mixture models, while the black cross in the lower right corner of the plot indicates the typical uncertainty.

Collectively these studies show that the transition from planet to star formation is not clear-cut, as the various populations, techniques, and investigated parameters suggest that the boundary is not strictly defined by the companion mass. Furthermore, these constraints have also been limited by heterogeneous data-sets, small sample sizes, and/or observational degeneracies that complicate the interpretation of companion demographics. This highlights the need for a well-characterized,

statistically significant sample of transiting BD companions from which more robust conclusions can be drawn. This thesis attempts to address that need by making significant contributions to the known population of transiting BDs to curate a more statistically robust sample, and then leveraging that sample's demographics to place new empirical constraints on the planetary-stellar boundary.

1.4 Outline

Chapter 2 of this thesis marks the first step towards expanding the transiting BD sample. It contains the work published in Vowell et al. (2023) presenting the discovery of a new, benchmark transiting BD, HIP 33609 b. Here we outline the initial discovery process for the transiting BD, ruling out false positive scenarios. We describe the use of the `EXOFASTv2` software (Eastman et al., 2019) for characterizing transiting BD companions and show that HIP 33609 b is a warm, eccentric transiting BD around a bright, massive B-type star making it an excellent candidate for further study and characterization. We also present the discovery of a new comoving group of stars (MELANGE-6) which contains HIP 33609 allowing us to constrain the age of the system. We use our independently constrained age to directly test BD evolutionary models, and compare HIP 33609 b to growing population of massive transiting companions.

In chapter 4, we further characterize the HIP 33609 system with the work published in Vowell et al. (2026), presenting a measurement of its stellar obliquity[3]. We find that HIP 33609 b is on a low obliquity orbit ($|\lambda| = 12.7 \pm 1.3°$) and show that its physical and orbital properties are most consistent with a stellar-like, fragmentation formation mechanism followed by a phase of coplanar, high eccentricity migration. We go on to show that BD stellar obliquities can inform us about transiting BD formation and evolution when taken as an ensemble, finding that the small sample of BD stellar obliquities appear to be most consistent with formation in isolated conditions and relatively quiescent migration.

In chapter 4, we expand our discovery efforts by presenting the discovery and confirmation of 11 new transiting BDs and low-mass stars which was published in Vowell et al. (2025). Armed with a statistically significant sample size, we perform a direct comparison between transiting

[3]Stellar obliquity is the relative angle between the host stars rotation axis, and an orbiting companion's orbital plane.

BD demographics and results of Ma & Ge (2014). We analyze the eccentricity and metallicity distributions of the transiting BD sample and show that they are inconsistent with the 42 M_J transition point suggested by (Ma & Ge, 2014). We also perform a deeper characterization on one of our most interesting transiting BDs, TOI-5882 b. We take note of Li in the host star's atmosphere (a characteristic often associated with young stars) and systematically rule out any other signs of youth using various indicators. The presence of this Li combined with a lack of any other signs of youth leads us to suggest that the TOI-5882 system may be a rare example of planetary engulfment.

Finally, we summarize the work presented in this thesis in chapter 5 and discuss the next steps. We show that a new population of astrometrically detected BDs is on the horizon with the upcoming release of Gaia DR4, and present a plan for analyzing their stellar obliquities. We explain that these systems can be utilized to make powerful inferences about BD formation and migration by comparing their stellar obliquity distribution to the growing sample of transiting BD stellar obliquities.

CHAPTER 2

HIP 33609 B: AN ECCENTRIC BROWN DWARF TRANSITING A V=7.3 RAPIDLY ROTATING B-STAR

This chapter presents the work published in (Vowell et al., 2023).

2.1 Abstract

We present the discovery and characterization of HIP 33609 b, a transiting warm brown dwarf orbiting a late B-star, discovered by NASA's Transiting Exoplanet Survey Satellite (*TESS*) as TOI-588 b. HIP 33609 b is a large ($R_b = 1.580^{+0.074}_{-0.070}\ R_J$) brown dwarf on a highly eccentric ($e = 0.560^{+0.029}_{-0.031}$) orbit with a 39-day period. The host star is a bright (V = 7.3 mag), $T_{\rm eff} = 10,400^{+800}_{-660}$ K star with a mass of $M_* = 2.383^{+0.10}_{-0.095}\ M_\odot$ and radius of $R_* = 1.863^{+0.087}_{-0.082}\ R_\odot$, making it the hottest transiting brown dwarf host star discovered to date. We obtained radial velocity measurements from the CHIRON spectrograph confirming the companion's mass of $M_b = 68.0^{+7.4}_{-7.1}\ M_J$ as well as the host star's rotation rate ($v \sin i_* = 55.6 \pm 1.8$ km/s). We also present the discovery of a new comoving group of stars, designated as MELANGE-6, and determine that HIP 33609 is a member. We use a combination of rotation periods and isochrone models fit to the cluster members to estimate an age of 150 ± 25 Myr. With a measured mass, radius, and age, HIP 33609 b becomes a benchmark for substellar evolutionary models.

2.2 Introduction

Brown dwarfs (BDs), defined as objects that fuse only deuterium at some point in their lifetime, occupy the region in mass between planets and stars. The mass range corresponding to this historical definition runs between a lower limit of 11-16 Jupiter Masses (MJ), where an object begins to fuse deuterium (Spiegel et al., 2011) and an upper limit of 75-80 MJ where hydrogen fusion begins (Baraffe et al., 2002). However, these fusion based transitions that distinguish BDs from planets and stars may occur at masses that depend on multiple factors. Specifically, the environment that the object formed in, the effects of convection on the object, and its metallicity can influence these traditional mass limits (Spiegel et al., 2011). Therefore, it may be preferable to define BDs in the context of their formation and evolution, an idea suggested by Chabrier et al. (2014), Burrows et al.

(2001), and Carmichael et al. (2021).

It is likely that some BDs form and evolve in similar ways to giant planets, providing the opportunity for comparative studies with the known exoplanet sample and possibly gaining insight into the evolutionary pathways of BDs. We know that planets can migrate through quiet mechanisms like disk-driven migration (D'Angelo et al., 2003) as well as dynamical interactions such as planet-planet scattering or Kozai-Lidov cycles (Kozai, 1962; Lidov, 1962; Fabrycky & Tremaine, 2007). Such dynamical interactions lead to a fraction of the population residing in close-in, highly misaligned as well as highly eccentric orbits (Rasio & Ford, 1996; Wu & Lithwick, 2011a). We can measure these misalignments using Doppler tomography (Collier Cameron et al., 2010; Zhou et al., 2016) and the Rossiter-McLaughlin effect. These techniques constrain the orbital obliquity of the companion by tracking the effects of the transiting planet's shadow on the rotationally broadened stellar spectral line profile or on the apparent radial velocity of the host star. If BDs are indeed subject to the same dynamical interactions as planets, then we should expect to see similar signatures in the transiting BD population.

In order to fully understand the formation and evolutionary history of BDs, we need robust, well-tested models for substellar evolution. Current substellar evolutionary models show that BDs rapidly contract in the first billion years after formation (Baraffe et al., 2003; Saumon & Marley, 2008; Burrows et al., 2001; Phillips et al., 2020), and then continue slowly contracting out to $\sim$10 Gyr. Combining this with the fact that BDs are held up by electron degeneracy pressure and therefore, at late times, tend to have radii that decrease with mass reveals the significance of obtaining precise age estimates for transiting BDs. Thus, in order to test our models of substellar evolution, we need precise, independent measurements of BD radii, masses, and ages. Through the combined efforts of NASA's Transiting Exoplanet Survey Satellite (*TESS*; Ricker et al., 2015), ground-based follow-up programs, and ESA's Gaia mission (Gaia Collaboration et al., 2022) we are able to obtain precise measurements of transiting BD radii and masses with transit photometry, radial velocity measurements, spectral energy distributions (SEDs), and Gaia parallaxes.

Precisely measuring the age of the BD, while difficult, is vital to furthering our understanding of

BD evolution because it provides a direct test of substellar evolutionary models. Unfortunately, only 4 of the 37 published transiting BD systems have precisely measured ages ($> 3\sigma$) determined either through stellar cluster memberships (Gillen et al., 2017; Beatty et al., 2018; David et al., 2019) or leveraging gyrochronology and lithium abundances (Carmichael et al., 2021). The simplest method for obtaining precise ages of BDs would be to discover more around host stars that are members of clusters. This kind of targeted discovery is already underway for planets by the *TESS* Hunt for Young and Maturing Exoplanets (THYME) consortium (Newton et al., 2019) and can also be applied to BDs in order to better understand their evolutionary pathways.

In this paper, we present the discovery of HIP 33609 bfrom NASA's *TESS* mission. HIP 33609 badds to the growing number of transiting BDs discovered by *TESS* that is approaching a population large enough to begin performing robust demographic analyses. It is also a benchmark system for testing BD formation and evolution since it has an age measurement from membership in a stellar association, and its host star is both the brightest (V = 7.3 mag) and hottest ($T_{\rm eff} = 10,400^{+800}_{-660}$ K) star with a transiting BD companion discovered so far. HIP 33609 b's high orbital eccentricity ($e = 0.560^{+0.029}_{-0.031}$) could be indicative of a dynamically active past, and we should therefore search for additional evidence of past interactions (such as a large stellar obliquity). In §2.3 we present our follow up photometric and spectroscopic observations obtained through the *TESS* Follow-up Observing Program (TFOP) Working Group. We establish HIP 33609's cluster membership and age in §2.4. In §3.4 we describe our global modeling methodology using `EXOFASTv2` (Eastman et al., 2013, 2019) as well a separate analysis on the effects of gravity darkening. We place HIP 33609 bin context with other transiting substellar companions and discuss future characterization prospects in §2.6. We present our conclusions in §2.7.

2.3 Observations

To measure the mass and orbital parameters of the HIP 33609 system, we used a combination of photometric (Figures 2.1 and 2.2) and spectroscopic (Figure 2.3) observations. The observations, gathered through the *TESS* Follow-up Observing Program (TFOP), were part of the vetting process to rule out false positive scenarios. We describe these observations in the following sub-sections.

Table 2.1 Literature and Measured Properties for HIP 33609

Other identifiers			
	TOI-588		
	TIC 130415266		
	HD 52470		
	HIP 33609		
	TYC 8122-01924-1		
	2MASS J06585996-4701240		
	TESS Sector	[6, 8, 33, 34, 35*]	
Parameter	Description	Value	Reference
α_{J2000}‡	Right Ascension (RA)	06:58:59.966	1
δ_{J2000}‡	Declination (Dec)	-47:01:24.121	1
G	Gaia G mag.	7.26±0.02	1
B_P	Gaia B_P mag.	7.27±0.02	1
R_P	Gaia R_P mag.	7.30±0.02	1
T	TESS mag.	7.312±0.006	2
B_T	Tycho B_T mag.	7.271±0.02	3
V_T	Tycho V_T mag.	7.284±0.02	3
J	2MASS J mag.	7.245±0.020	4
H	2MASS H mag.	7.326±0.031	4
K_S	2MASS K_S mag.	7.278±0.027	4
WISE1	*WISE1* mag.	7.263±0.036	5
WISE2	*WISE2* mag.	7.326±0.030	5
WISE3	*WISE3* mag.	7.354±0.030	5
WISE4	*WISE4* mag.	7.4±0.1	5
μ_α	Gaia DR3 proper motion in RA (mas yr^{-1})	-9.505±0.073	1
μ_δ	Gaia DR3 proper motion in DEC (mas yr^{-1})	-4.467±0.071	1
$v \sin i_\star$	Rotational velocity (km s^{-1})	55.6±1.8	§2.3.3
$\pi^\dagger$	Gaia DR3 Parallax (mas)	6.49±0.05	1

NOTES: The uncertainties of the photometry have a systematic error floor applied.
‡ RA and Dec are in epoch J2000. The coordinates come from Vizier where the Gaia RA and Dec have been precessed and corrected to J2000 from epoch J2015.5.
† Values have been corrected for the -0.30 μas offset as reported by Lindegren et al. (2018) but this is not significant for these systems.
References are: [1](Gaia Collaboration et al., 2022),[2](Høg et al., 2000), [3]Stassun et al. (2018),[4]Cutri et al. (2003), [5]Cutri et al. (2012)

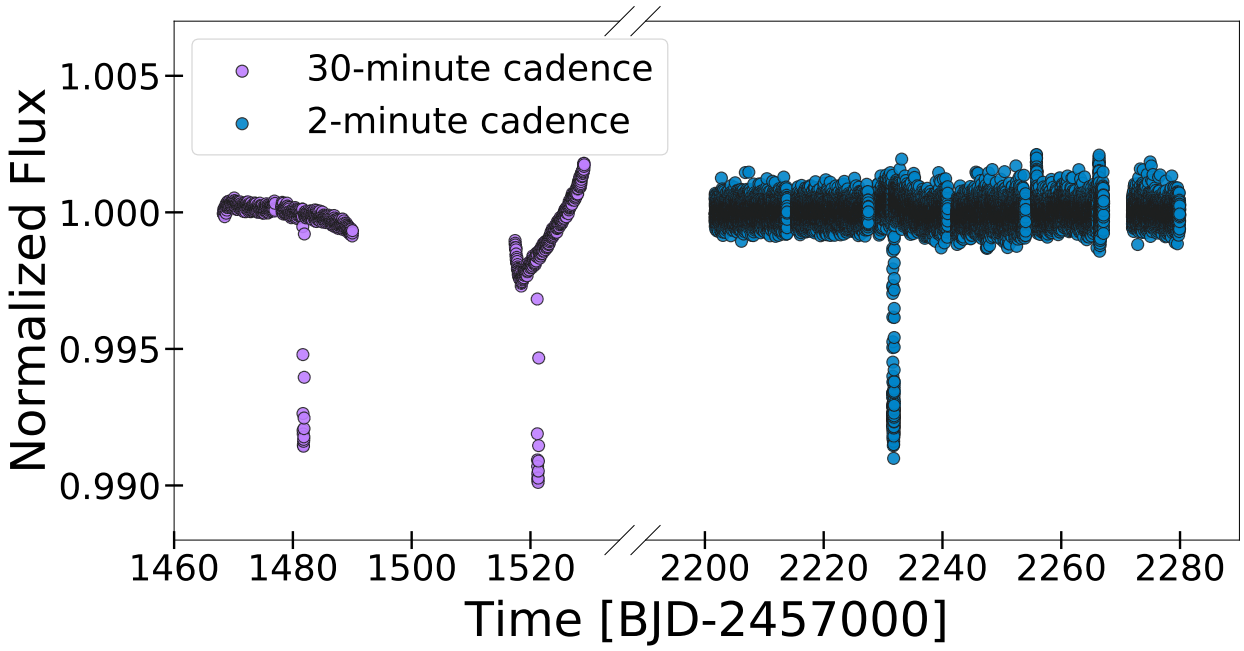

Figure 2.1 The *TESS* light curves from sectors 6, 8, 33, 34, and 35 extracted using the techniques described in §2.3.1. We note that the gap in flux located at BJD 2459270 is caused by a period of coarse pointing. These poor data were removed in our fit as described in §2.3.1.

2.3.1 *TESS* Photometry

TESS observes a 24°x96° patch of the sky for approximately 27 days before moving to a new sector (Ricker et al., 2015). In the prime mission, it observed its entire field of view at 30-minute cadence, and a pre-selected set of stars were observed at 2-minute cadence, resulting in >80% of the entire sky being observed. *TESS* just completed its first extended mission in which it observed a portion of the ecliptic plane, the region of sky observed by the *K2* mission (Howell et al., 2014) which repurposed the Kepler spacecraft to observe the ecliptic plane after the loss of the spacecraft's 2nd of four reaction wheels. This region was not observed during the TESS prime mission, but a portion was observed over a 5-month period in the first extended mission, and another portion will be observed over a 4-month period in the second extended mission which started 2 September 2022. A subset of ~2,000 of the 20,000 preselected targets in the extended missions[1] are observed at 20-second cadence in addition to 2-minute cadence, and the exposure time for the Full Frame Images (FFI) was reduced to 10 minutes in the first extended mission, and further reduced to just

[1] `https://heasarc.gsfc.nasa.gov/docs/tess/the-tess-extended-mission.html`

200 seconds in the second extended mission. HIP 33609 b was first observed during the primary mission in the sector 6 FFIs at 30-minute cadence in 2018 and then again in sector 8 in 2019. *TESS* then observed HIP 33609 again during its first extended mission at 2-minute cadence in 2021 during sectors 33, 34, and 35.

TESS observations are downloaded, reduced, and analyzed on the ground. The original detection of a transiting signal around HIP 33609 was made by the MIT Quick Look Pipeline (QLP), and it was then vetted as a *TESS* Object of Interest (TOI-588, Table 2.1) using the process described by Guerrero et al. (2021). In subsequent observations, the data collected by TESS at 2-minute cadence were processed by the Science Processing Operations Center (SPOC) pipeline (Jenkins et al., 2016) based at NASA Ames Research Center where the image data were calibrated, and light curves were extracted for each target, which were then searched for transiting planet signatures. We then downloaded these SPOC PDC-SAP light curves (Smith et al., 2012; Stumpe et al., 2012, 2014) from the Mikulski Archive for Space Telescopes (MAST) using the *Lightkurve 2* software (Lightkurve Collaboration et al., 2018). The SPOC transit search over sectors 34 and 35 triggered on the single transit of HIP 33609 b in sector 34, but at the wrong period. Nevertheless, the difference image centroiding test located the source of the transit signature within 1.2 ± 2.8 arcsec. We conducted a Lomb-Scargle period search on the 2-minute, normalized light curve with the transits masked out to search for stellar rotation from star spots. We searched for periods ranging from 0.1 to 10 days and found no significant signal as expected from a relatively quiet B-type star.

We found a total of 4 transits of HIP 33609 in sectors 6, 8, 34, and 35. However, we discarded the sector 35 transit due to poor data quality caused by a period of unstable pointing of the *TESS* spacecraft. During this period, the stars moved around significantly on the detector, introducing large systematic errors.

For our global analysis, we used the SPOC 2-minute light curve for the sector 34 transit, but we re-extracted the 30-minute FFI light curves for sectors 6 and 8 using a custom FFI pipeline based on the procedure described by Vanderburg et al. (2019). In brief, we performed aperture photometry on a series of 20 apertures, decorrelated each extracted light curve against the background flux

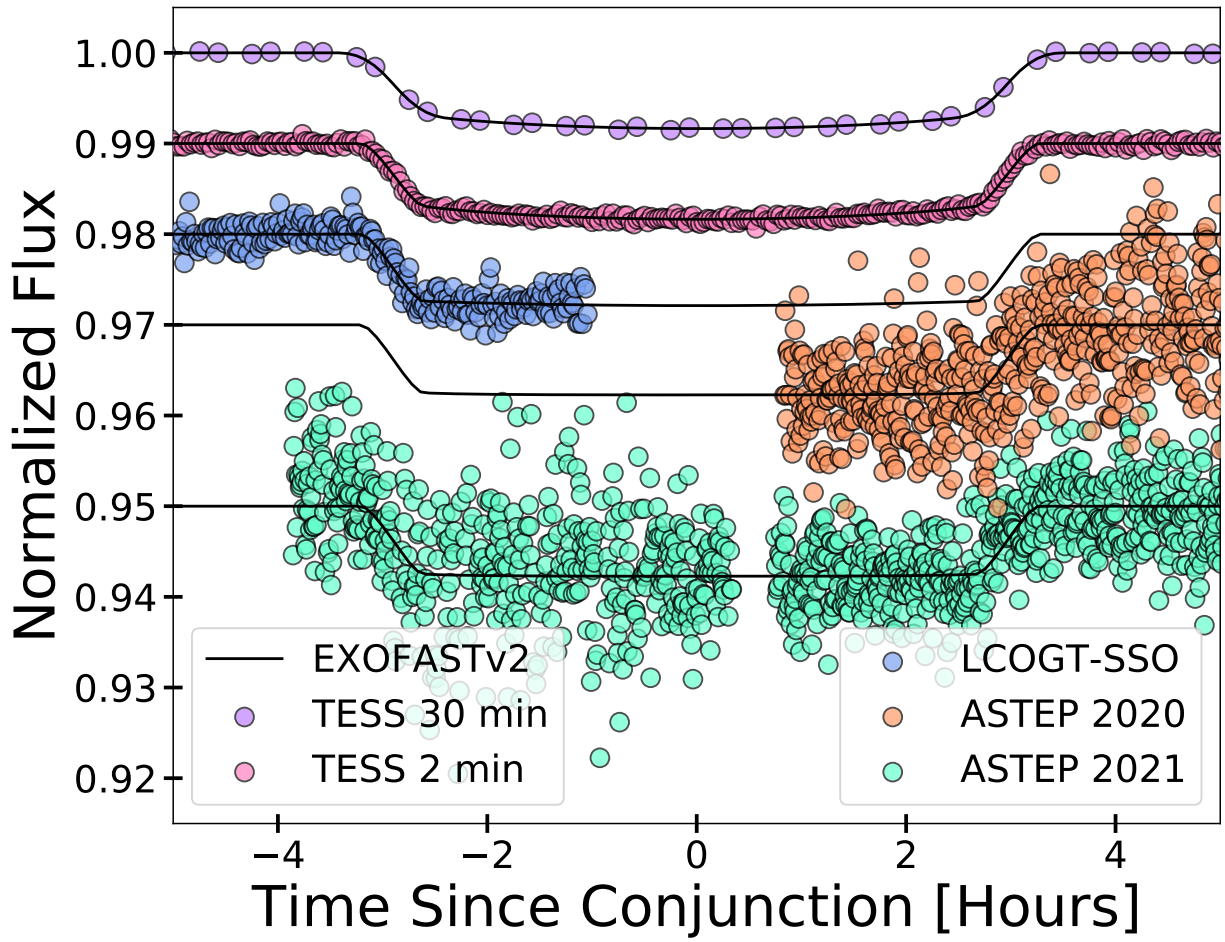

Figure 2.2 The *TESS* and ground-based follow-up transits for HIP 33609 bdescribed in sections §2.3.1 and §2.3.2. The model for each transit is shown as a black solid line.

outside the aperture and the mean value and standard deviation of pointing excursions during each exposure (measured from the spacecraft quaternion time series), and selected the light curve from the aperture that maximized photometric precision. We then removed any long-term instrumental and stellar variability signals by fitting a spline to the flux using *Keplerspline*[2] and then dividing the light curve by the best fit model (Vanderburg & Johnson, 2014). We then removed most of the out-of-transit baseline from both light curves keeping only half a transit duration on each side of the transit since these data provide little to no information to the global fit while simultaneously being computationally expensive to model. These light curves were fit simultaneously with all available data on the HIP 33609 system (see §2.5.1).

[2]`https://github.com/avanderburg/keplerspline`

2.3.2 Ground-based Photometric Follow-up

In order to rule out contamination by a background eclipsing binary and refine the ephemeris, we observed HIP 33609 as a part of SubGroup 1 (seeing limited photometry) of the *TESS* Follow-up Observing Program (TFOP). We obtained these observations using the Las Cumbres Observatory Global Telescope (LCOGT) telescope network (Brown et al., 2013) and the 40 cm ASTEP-400 telescope (Abe et al., 2013; Guillot et al., 2015). Both facilities confirm the existence of a transit on the target star, HIP 33609, and confirm that there are no nearby stars that exhibit variability.

We observed an ingress of HIP 33609 b on 08 December 2020 UT from LCOGT-SSO on the 1 m telescope in the y-band at 25 s cadence with a pixel scale of 0.389". We observed an egress on 12 August 2020 UT and a full transit (save for a brief gap mid-transit due to a brief noon twilight) on 23 June 2021 UT with ASTEP using a 25 s exposure time with a pixel scale of 0.93". More transit observations were attempted by LCOGT and ASTEP, however they were at too low S/N to provide value to our global fit while increasing the computational cost. We therefore discard these transits and only show the 3 ground based transits used in our analysis. We reduced these data sets and extracted the light curves using `AstroImageJ` (Collins et al., 2017). We detrended the LCO light curve against airmass and detrended the ASTEP light curves against both airmass and sky/pixels. See §D in the appendix of Collins et al. (2017) for a detailed description of the detrending parameters.

2.3.3 CHIRON Spectroscopy

We observed HIP 33609 on 39 separate nights from 24 January 2020 UT through 2 November 2021 UT (Table 2.2) using the CHIRON spectrograph on the 1.5 m SMARTS telescope located at the Cerro Tololo Inter-American Observatory (CTIO) in Chile (Tokovinin et al., 2013; Paredes et al., 2021). CHIRON is a high resolution echelle spectrograph fed with an image slicer through a single multi-mode fiber which achieves a spectral resolving power of R = 80,000 over the range 410 to 870 nm. We used these spectra to constrain the stellar parameters of the host star and extract the radial velocities (RVs). In order to extract the RVs, we derived the line profiles from our observed spectra by performing a least squares deconvolution (Donati et al., 1997; Zhou et al., 2020). We

Table 2.2. The radial velocity measurements for the HIP 33609 system.

BJD_{TDB}	RV ($m\ s^{-1}$)	σ_{RV} ($m\ s^{-1}$)	BJD_{TDB}	RV ($m\ s^{-1}$)	σ_{RV} ($m\ s^{-1}$)
2458872.64968	32201.9	769.6	2459364.44268	31314.1	873.7
2458874.68716	29813.7	1029.1	2459497.86645	32346.2	1247.6
2459265.59795	31140.8	1125.7	2459498.86337	33896.8	823.9
2459271.58653	29249.9	1019.7	2459502.88700	31873.6	702.7
2459276.56080	28538.2	842.3	2459505.82903	31722.4	1189.3
2459281.57067	30041.5	1049.7	2459506.88278	29142.3	896.2
2459286.69996	33204.2	974.2	2459508.84044	29556.2	785.5
2459294.55752	32251.1	1093.2	2459509.76436	27200.5	998.3
2459303.54558	32293.7	1167.0	2459510.79825	27373.0	1564.7
2459321.52137	30560.4	900.5	2459511.77084	27838.5	820.2
2459323.52343	30998.6	992.5	2459512.81732	27742.1	886.0
2459331.46144	31450.3	685.8	2459513.82850	29202.6	853.4
2459333.48087	31801.6	1571.2	2459514.80241	29779.1	889.0
2459336.46010	32079.4	868.0	2459515.76514	30906.6	792.1
2459340.49478	32912.0	930.0	2459516.81742	31576.8	917.3
2459342.47356	31829.6	1002.2	2459517.82665	30789.3	711.5
2459344.46994	32443.8	1230.7	2459518.73563	31764.7	927.9
2459347.50808	31687.2	979.7	2459519.81360	31232.3	1781.9
2459351.46803	26993.6	1195.5	2459520.79849	33014.2	944.1
2459361.44832	30419.7	591.6			

deconvolved against synthetic spectral templates generated using the ATLAS9 model atmospheres (Kurucz, 1992) with our rotational broadening kernel applied.

We measured the projected rotational velocity $v \sin i_*$ of the host star by modeling the line profiles from our spectra with a convolution of kernels as prescribed by Zhou et al. (2018). They consisted of rotation and radial-tangential macroturbulence kernels from Gray (2005) and an instrumental broadening kernel which is represented as a Gaussian with a width equivalent to the instrumental resolution. From this analysis, we found that HIP 33609 has a projected rotational velocity of $v \sin i_* = 55.6 \pm 1.8$ km/s. We constrained the stellar atmospheric parameters such as metallicity and effective temperature by comparing our spectra to an interpolated library of spectra classified by the Stellar Parameter Classification (SPC) package (Buchhave et al., 2012). However, we only utilized this analysis as a consistency check as determining stellar parameters through spectra is highly uncertain for rapidly rotating B-type stars like HIP 33609 (Gaudi et al., 2017). Therefore, we adopt the stellar parameters derived in our global fit which are constrained by simultaneously fitting to the SED and stellar isochrones.

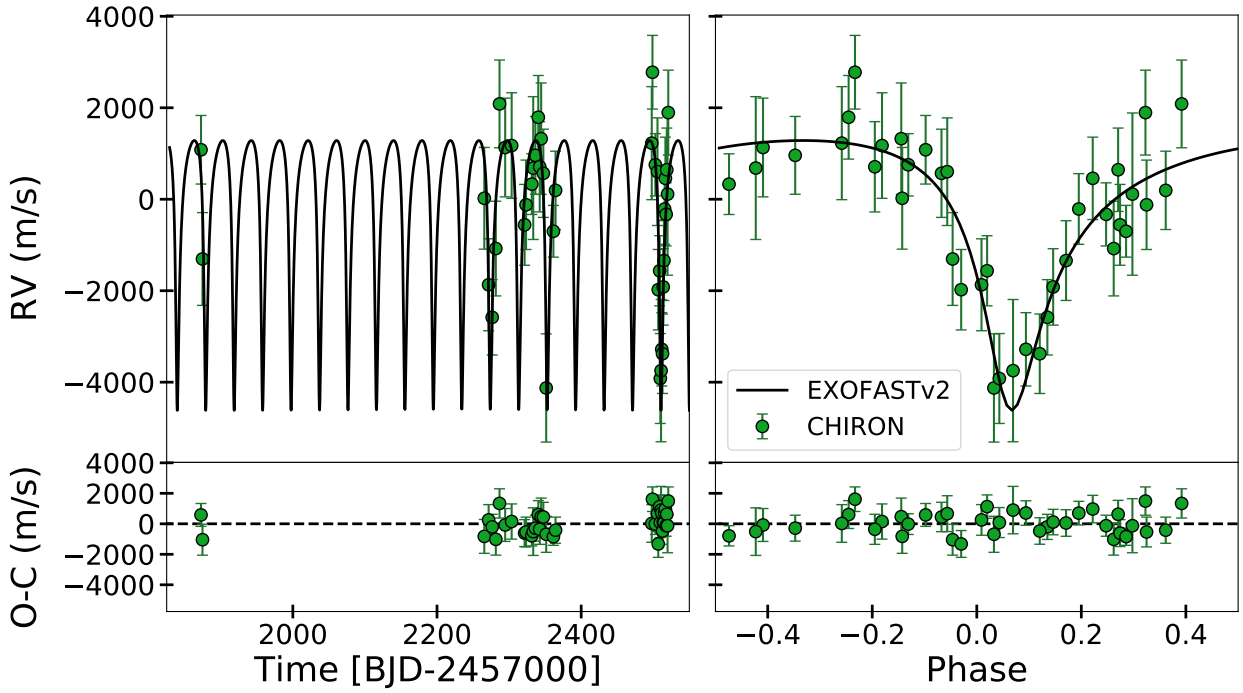

Figure 2.3 The radial velocity observations from CHIRON unphased (left) and phased to our best fit ephemeris (right).

2.3.4 Spectral Energy Distribution

We fit the broadband SED simultaneously as a part of our global `EXOFASTv2` analysis (see §2.5.1). However, we also performed a separate analysis of the SED in order to independently determine the basic stellar parameters and serve as a consistency check for our global analysis. We analyzed the SED of the star together with the *Gaia* DR3 parallax (with no systematic offset applied; see, e.g., Stassun & Torres, 2021), in order to determine an empirical measurement of the stellar radius, following the procedures described in Stassun & Torres (2016); Stassun et al. (2017); Stassun & Torres (2018). We pulled the $B_T V_T$ magnitudes from *Tycho-2*, the JHK_S magnitudes from *2MASS*, the W1–W4 magnitudes from *WISE*, and the G $G_{\rm BP}$ $G_{\rm RP}$ magnitudes from *Gaia*. We also used the UV measurements at 157–274 nm from the TD1 UV satellite (Boksenberg et al., 1973; Thompson et al., 1978). Together, the available photometry spans the full stellar SED over the wavelength range 0.15–22 μm (see Figure 2.4).

We performed a fit to the SED using Kurucz stellar atmosphere models, with the main parameters being the effective temperature ($T_{\rm eff}$), surface gravity ($\log g$), and metallicity ([Fe/H]), for which

we adopted the spectroscopically determined values: $T_{\rm eff} = 10,570^{+850}_{-710}$, $\log g = 4.259^{+0.057}_{-0.063}$, [Fe/H]= $-0.26^{+0.38}_{-0.61}$. The remaining free parameter was the extinction A_V, which we limited to the maximum line-of-sight value from the Galactic dust maps of Schlegel et al. (1998). The resulting fit has a reduced χ^2 of 1.5 and best fit $A_V = 0.20 \pm 0.03$. Integrating the model SED gives the bolometric flux at Earth, $F_{\rm bol} = 5.12 \pm 0.24 \times 10^{-8}$ erg s^{-1} cm^{-2}. Taking the $F_{\rm bol}$ and $T_{\rm eff}$ together with the *Gaia* parallax yields the stellar radius, $R_\star = 1.81 \pm 0.27$ R$_\odot$. In addition, we used the empirical relations of Torres et al. (2010), to estimate the stellar mass $M_\star = 2.38 \pm 0.14$ M$_\odot$, which is consistent with the value of 2.18 ± 0.66 M$_\odot$ determined empirically via $R_\star$ and $\log g$.

Finally, we can extrapolate the model atmosphere below 0.1 nm (see Stassun & Torres, 2016) to estimate the XUV radiation in the BD's environment, for which we find $F_{\rm XUV} = 302^{+532}_{-208}$ erg s^{-1} cm^{-2} at a distance of 1 AU from the star. Overall, we find this analysis is consistent at the 1σ level with the results of our global analysis, and so we adopt the results of our `EXOFASTv2` fit since it simultaneously fits all available data.

2.3.5 High Resolution Imaging

If an exoplanet host star has a spatially close companion, that companion (bound or line of sight) can create a false- positive transit signal if it is, for example, an eclipsing binary (EB). The flux from a close companion star constitutes "third-light" and may lead to an underestimated planetary radius if not accounted for in the transit model (Ciardi et al., 2015) and cause non-detections of small planets in the same exoplanetary system (Lester et al., 2021). Additionally, the discovery of close, bound companion stars, which exist in nearly one-half of FGK type stars (Matson et al., 2018), provides crucial information toward our understanding of exoplanetary formation, dynamics and evolution (Howell et al., 2021). Thus, to search for close-in bound companions unresolved in TESS observations, we obtained high-resolution imaging speckle observations of HIP 33609.

HIP 33609 was observed on 2022 March 03 UT using the Zorro speckle instrument on the Gemini South 8-m telescope (Scott et al., 2021; Howell & Furlan, 2022). Zorro provides simultaneous speckle imaging in two bands (562 nm and 832 nm) with output data products including a reconstructed image with robust contrast limits on companion detections. Three sets of 1000 ×

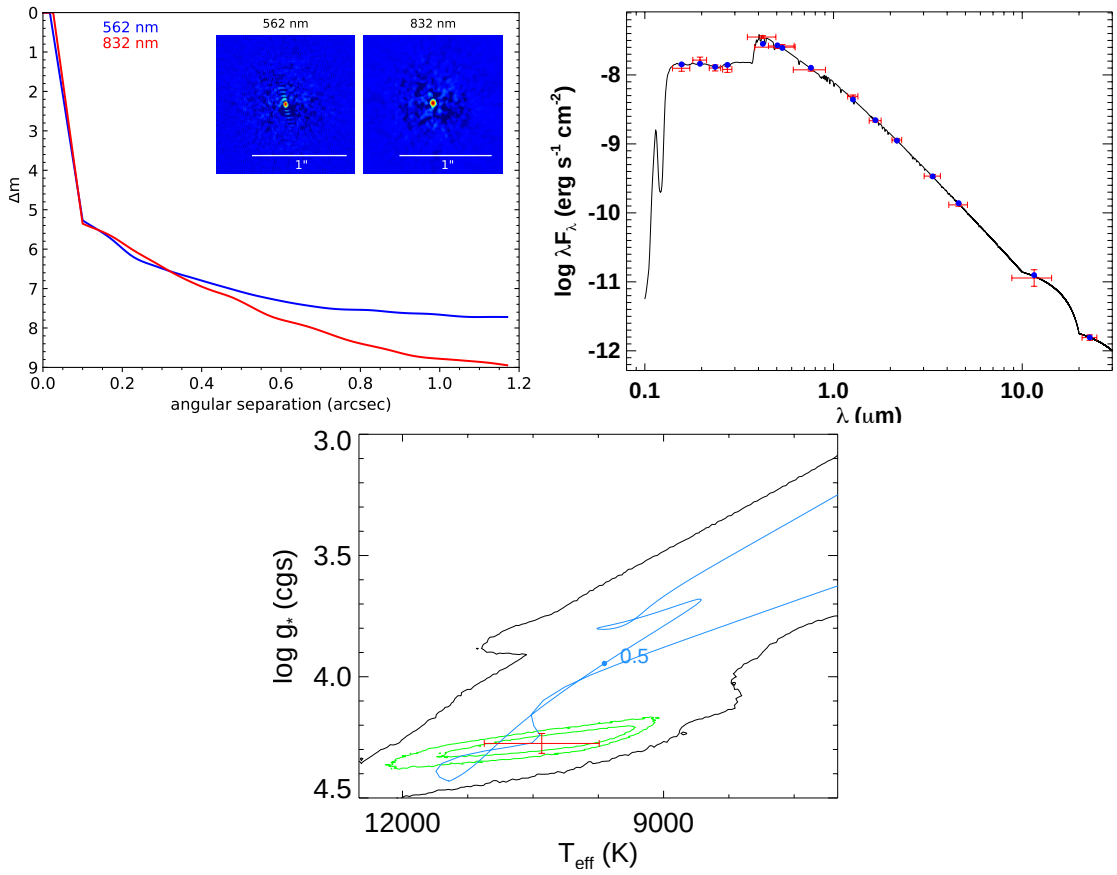

Figure 2.4 (Upper Left) The 5σ speckle imaging contrast curves in both filters as a function of the angular separation from the diffraction limit (20 mas) out to 1.2 arcsec, the end of speckle coherence. The inset shows the reconstructed 562 nm and 832 nm images with a 1 arcsec scale bar. HIP 33609 was found to have no close companions to within the angular and contrast levels achieved. (Upper Right) Spectral energy distribution of HIP 33609Ṙed symbols represent the observed photometric measurements, where the horizontal bars represent the effective width of the passband. Blue symbols are the model fluxes from the best-fit Kurucz atmosphere model (black). (Bottom) The best fitting MIST evolutionary track shown in blue with the 3σ contours on the best fit MIST track in black. The red point indicates the median value and 1σ error bars from our global analysis, while the green contours show the 3σ errors. The blue point indicates the location of 0.5 Gyr on the evolutionary track.

0.06 s exposures were collected on HIP 33609 and subjected to Fourier analysis in our standard reduction pipeline (see Howell et al. 2011). Figure 2.4 shows our final contrast curves and the two reconstructed speckle images. We find that HIP 33609 is a single star with no companion brighter than 5-9 magnitudes below that of the target star from the diffraction limit (20 mas) out to 1.2″. At the distance of HIP 33609 (d=154 pc) these angular limits correspond to spatial limits of 3 to 185 AU.

We also observed HIP 33609 on 18 May 2019 UT from the 4.1-m Southern Astrophysical Research (SOAR) telescope with speckle interferometry in the *I*-band (Tokovinin, 2018). We took these observations in-line with the general observing strategy for *TESS* targets described in Ziegler et al. (2020) with an estimated contrast of Δmag = 7.7 at 1". We found no nearby companions out to 3".

2.4 Membership and Age Determination of HIP 33609

2.4.1 MELANGE-6

We searched for evidence that HIP 33609 is a member of a young stellar association using the `FriendFinder` [3] (Tofflemire et al., 2021). `FriendFinder` used *Gaia* DR3 positions and parallaxes to identify all sources that fell within our selected three-dimensional search radius around HIP 33609İt then calculated the predicted tangential velocity (v_{tan}) for every nearby source assuming they have an identical *UVW* as the source. `FriendFinder` then compared that value to the true v_{tan}, derived from the *Gaia* proper motions. For this grouping, we selected targets with separation <25 pc and a difference in predicted and measured v_{tan} of < 5 km s^{-1}. A larger physical search radius yielded more objects consistent with membership, but the narrow selection was more than sufficient for aging the star and demonstrating the existence of an association.

Our selection yielded 283 stars, including HIP 33609. The population color-magnitude diagram (CMD) followed a tight Pleiades-like sequence (Figure 2.5). Further, a high fraction of the candidate co-movers had *Gaia* radial velocities consistent with HIP 33609İmportantly, `FriendFinder` did not use radial velocities or CMD information for selection, so consistency here made it clear this

[3] `https://github.com/adamkraus/comove`

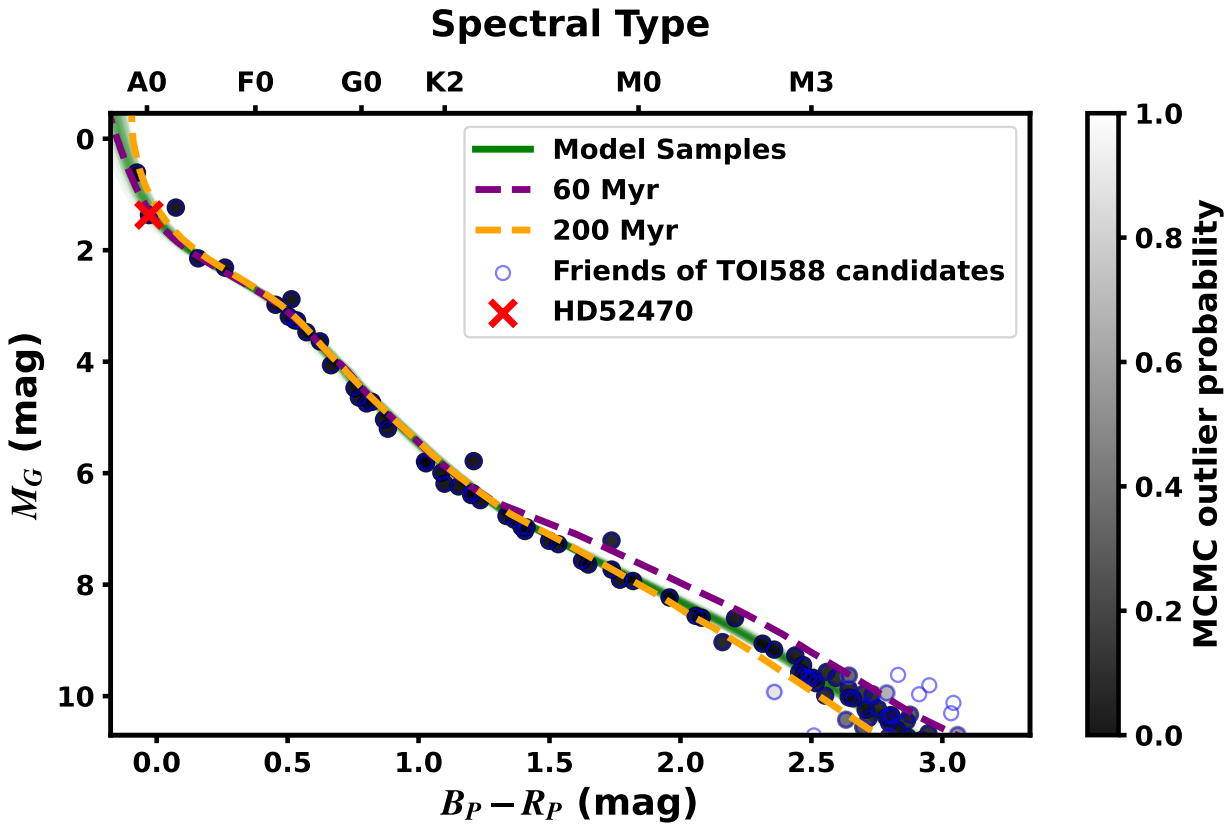

Figure 2.5 Color-magnitude diagram (CMD) of stars spatially and kinematically near HIP 33609. The green lines show random draws from our MCMC fit posterior. Points are shaded by the probability that they are part of the outlier model. HIP 33609 is denoted with a red X. The orange and purple lines designate age extremes for reference.

is a true co-moving and co-eval population. We denoted this population MELANGE-6, following the convention from Tofflemire et al. (2021).

2.4.2 Measuring MELANGE-6's age

To determine the age of MELANGE-6 (and hence the age of HIP 33609) we first compared the *Gaia* magnitudes to model isochrones following Mann et al. (2022). To briefly summarize, we used a mixture model as outlined in Hogg et al. (2010). The mixture contained two models, one for the single-star co-eval population, and an outlier population to account for non-members and binaries, inclusion of which tends to bias the isochronal age to older or younger ages, respectively. The fit was done in an MCMC framework using `emcee` (Foreman-Mackey et al., 2013). The six free parameters were age (τ), reddening ($E(B-V)$ [mags]), the amplitude of the outlier population

(P_B), the offset from the main population to the outlier population (Y_B [mags]), the variance in the outlier population (V_B) and a parameter to account for underestimated uncertainties or differential reddening (f [mags]).

We tested fits using the PARSECv1.2 (Bressan et al., 2012) and the Dartmouth Stellar Evolution Program (DSEP; Dotter et al., 2008) with magnetic enhancement (Feiden & Chaboyer, 2012). We initially restricted our analysis to Solar metallicity, but tested [M/H]=-0.1 and +0.1 with the PARSEC models. The DSEP-magnetic models were only available at Solar metallicity and did not extend to the highest-mass stars in the group. We ran the fit with 20 walkers for 10,000 steps following a burn-in of 2,000 steps, which was >50 times the autocorrelation time.

As we show in Figure 2.5, ages $\gtrsim$ 200 Myr or $<$ 80 Myr failed to reproduce the pre-main-sequence M dwarfs. The isochrone fit yielded an age of 106^{+11}_{-8} Myr, with negligible reddening ($E(B-V) < 0.05$) and a small outlier population ($P_B = 0.15 \pm 0.05$). The errors on the age are likely underestimated due to our assumptions and limitations of the models. For example, a slightly metal-rich grid ([M/H]=+0.1) gave a similar fit and yielded an older age 118^{+12}_{-8} Myr. Additional adjustments, such as down-weighting the coolest stars, where models struggle to reproduce observations, changed the age at the 10 Myr level.

As an additional constraint on age, we also measured rotation periods for candidate members of MELANGE-6 from their *TESS* light curves. The rotation sequence provides an age constraint that is (largely) independent of the isochronal measurement, instead relying on the relation between age, color, and rotation period (Gyrochonology; Barnes, 2003).

We followed the method outlined in Barber et al. (2022). To briefly summarize, we generated *TESS* light curves from the FFI cutouts, first creating raw flux light curves from the FFI cutouts centered on each candidate. Then, we generated a Causal Pixel Model (CPM) of the telescope systematics using the `unpopular` package (Hattori et al., 2021) using the "Similar Brightness" to generate the model for each star. We subtracted the resulting CPM systematic model from the initial light curves. In total, we extracted usable light curves for 117 targets; the majority of the remaining were too faint or had significant contaminating flux from nearby stars.

We searched every single-sector light curve for each star for rotation periods from 0.1 – 30 days using the Lomb-Scargle algorithm (Lomb, 1976). Each identified period was inspected by eye and assigned a quality score following Rampalli et al. (2021) with an additional quality flag of -99 for stars with no data or stars beyond *TESS* rotation period detection limits (*TESS* mag > 15 or contamination ratio > 1.6). We retained periods with a score of Q0 or Q1 (105 stars).

We show the rotation sequence in Figure 2.6. The slowly-rotating sequence of FGK dwarfs in MELANGE-6 sits above the Pleiades (Rebull et al., 2016), indicating an age > 112 Myr (Dahm, 2015). The sequence also closely matches that of Theia 456 (Kounkel & Covey, 2019) which was recently determined to be 150-200 Myr (Andrews et al., 2022).

The gyrochronological age is somewhat older than our isochronal value. However, the systematics in the isochronal age were sufficient that the measurements are consistent. We adopted a generous age of 150±25 Myr which encompasses both estimates.

2.5 Analysis

2.5.1 EXOFASTv2 Global Fits

We globally fit all available data using the public exoplanet fitting suite `EXOFASTv2` (Eastman et al., 2013, 2019) in order to determine the host star and companion parameters for the HIP 33609 system (Tables 2.3 and 2.4). We fit the Spectral Energy Distribution (SED) and used the MESA Isochrones and Stellar Tracks (MIST) stellar evolution models (Paxton et al., 2011, 2013, 2015; Choi et al., 2016; Dotter, 2016) in order to constrain the parameters of the host star. We account for smearing from the 30-minute cadence in our FFI light curves from sectors 6 and 8. Our ground-based photometric follow-up from both LCOGT and ASTEP were additively detrended against the parameters described in §2.3.2 (Collins et al., 2017).

We initially exclude all ground-based transits from the fit, incorporating only the *TESS* transits, CHIRON radial velocities, and the SED. We turn off the Claret (Claret, 2017) tables for these fits since they are less reliable for hot stars (> 10,000 K) and allow the fit to constrain the quadratic limb darkening coefficients (LDCs) directly from the *TESS* transits. The *TESS* 30-minute and 2-minute light curves have out-of-transit standard deviations of 110 ppm and 310 ppm respectively,

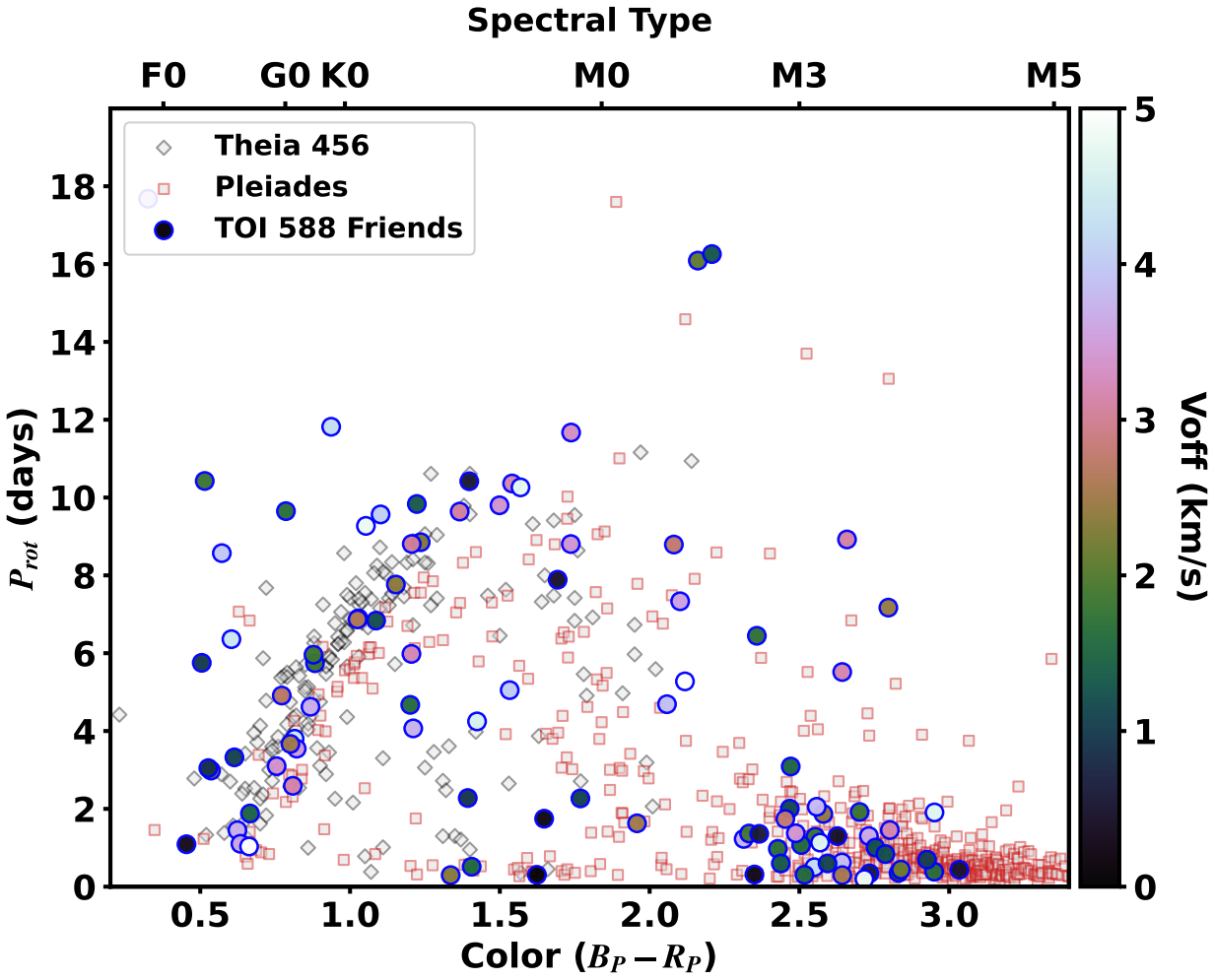

Figure 2.6 Rotation periods of candidate members of MELANGE-6 as a function of $B_P - R_P$ color. The rotation periods show a clear sequence as expected for a co-eval association, and the outliers tend to be further from HIP 33609 kinematically (see color-coding). We show the sequences for Theia 456 (150-200 Myr Andrews et al., 2022) and Pleiades (112 Myr Rebull et al., 2016) for comparison.

Table 2.3 Median values and 68% confidence interval for global model of HIP 33609

Stellar Parameters:		
M_*	Mass ($M_\odot$)	$2.383^{+0.10}_{-0.095}$
R_*	Radius ($R_\odot$)	$1.863^{+0.087}_{-0.082}$
F_{Bol} ...	Bolometric Flux (cgs)	$0.0000000492^{+0.0000000014}_{-0.0000000097}$
ρ_*	Density (cgs)	$0.519^{+0.076}_{-0.065}$
log$g$ ...	Surface gravity (cgs)	$4.274^{+0.042}_{-0.040}$
$T_{\rm eff}$	Effective Temperature (K)	10400^{+800}_{-660}
[Fe/H]	Metallicity (dex)	$-0.01^{+0.19}_{-0.20}$
$[{\rm Fe/H}]_0$	Initial Metallicity	$0.02^{+0.18}_{-0.20}$
Age ...	Age (Gyr)	0.153 ± 0.024
EEP ..	Equal Evolutionary Phase	$314.3^{+7.3}_{-7.4}$
A_V	V-band extinction (mag)	$0.134^{+0.075}_{-0.084}$
σ_{SED} ..	SED photometry error scaling	$1.28^{+0.38}_{-0.26}$
ϖ	Parallax (mas)	6.483 ± 0.049
d	Distance (pc)	154.3 ± 1.2
Planetary Parameters:		b
P	Period (days)	39.471814 ± 0.000014
R_P	Radius (R_J)	$1.580^{+0.074}_{-0.070}$
M_P	Mass (M_J)	$68.0^{+7.4}_{-7.1}$
T_C	Time of conjunction ($\rm BJD_{TDB}$)	$2459231.75856 \pm 0.00021$
T_0	Optimal conjunction Time ($\rm BJD_{TDB}$)	$2458915.98404 \pm 0.00017$
a	Semi-major axis (AU)	$0.3058^{+0.0042}_{-0.0041}$
i	Inclination (Degrees)	89.13 ± 0.15
e	Eccentricity	$0.560^{+0.029}_{-0.031}$
ω_*	Argument of Periastron (Degrees) ..	$165.9^{+5.5}_{-5.6}$
T_{eq}	Equilibrium temperature (K)	1237^{+73}_{-61}
$\tau_{\rm circ}$	Tidal circularization timescale (Gyr)	9800^{+6300}_{-4000}
K	RV semi-amplitude (m/s)	2700 ± 290
R_P/R_* .	Radius of planet in stellar radii	$0.08715^{+0.00034}_{-0.00036}$
a/R_* ...	Semi-major axis in stellar radii	$35.3^{+1.6}_{-1.5}$
τ	Ingress/egress transit duration (days)	$0.02401^{+0.00088}_{-0.00089}$
T_{14}	Total transit duration (days)	0.26960 ± 0.00080
b	Transit Impact parameter	$0.328^{+0.042}_{-0.053}$
$T_{S,14}$ ...	Total eclipse duration (days)	$0.341^{+0.031}_{-0.028}$
ρ_P	Density (cgs)	$21.3^{+4.0}_{-3.4}$
$logg_P$.	Surface gravity	$4.829^{+0.059}_{-0.062}$
$\langle F \rangle$	Incident Flux (10^9 erg s^{-1} cm^{-2}) ...	$0.398^{+0.11}_{-0.075}$
T_S	Time of eclipse ($\rm BJD_{TDB}$)	$2459238.47^{+0.75}_{-0.68}$
$e \cos \omega_*$	.....	$-0.541^{+0.037}_{-0.034}$
$e \sin \omega_*$	.....	$0.136^{+0.050}_{-0.051}$
d/R_* ..	Separation at mid transit	$21.3^{+2.3}_{-2.0}$

which was precise enough to independently constrain the LDCs in the *TESS* bandpass. We then add in each ground-based transit iteratively, ensuring that each successive fit is still consistent with the *TESS* only fit to 1σ. Since the ground-based light curves have too low S/N to constrain limb darkening in their respective bandpasses, we apply Gaussian priors on the LDCs according to the methods suggested by Patel & Espinoza (2022). The results presented in Tables 2.3, and 2.4 are the final iterations of this process including all ground-based light curves discussed in §2.3.2.

We adopted the age, as discussed in §2.4, of 150±25 Myr as a Gaussian prior in our global fits, and placed a Gaussian prior on the parallax from *Gaia* DR3 (Gaia Collaboration et al., 2022) while correcting for the parallax bias according to Lindegren et al. (2021). We also placed an upper limit on the line of sight extinction as described in Schlegel et al. (1998) and Schlafly & Finkbeiner (2011). Because HIP 33609 is a rapidly rotating B-star, stellar parameters derived from spectroscopic observations are not reliable. Therefore, we do not obtain precise measurements for the stellar metallicity from our spectral analysis and thus set a Gaussian prior of 0.0 ± 0.5 dex. We also set a Gaussian prior of 0 ± 10% of the contamination ratio reported in the *TESS* Input Catalogue (TIC, Stassun et al., 2018) in order to fit for a dilution term in the *TESS* band. While the SPOC PDC-SAP light curves are corrected for known nearby companions, fitting for a dilution term accounts for unknown nearby blended stars in the *TESS* aperture and serves as an independent check on the reported contamination correction. We adopted the convergence criteria of Eastman et al. (2019) which recommend a Gelman-Rubin statistic < 1.01 and over 1000 independent draws.

2.5.2 Gravity Darkening Fit

Given that HIP 33609 is a rapidly rotating B-star, we expect that gravity darkening would have a significant effect on the light curve (Barnes, 2009). Hence, we performed two additional fits in order to investigate the effects of gravity darkening on HIP 33609's light curve. We perform a symmetric fit based on the standard Mandel & Agol (2002) transit model as well as an additional, similar fit following the techniques described in Hooton et al. (2022) in order to account for deviations induced by oblateness and brightness variations that arise from gravity darkening (see Figure 2.7). For this analysis, we fit only the transits from *TESS* because of the much lower signal to noise ratios

Table 2.4 Median values and 68% confidence interval for global model of HIP 33609

Wavelength Parameters:		R	z′	TESS
u_1	Linear LDC	$0.043^{+0.061}_{-0.032}$	$0.043^{+0.061}_{-0.032}$	0.359 ± 0.050
u_2	Quadratic LDC	$0.032^{+0.078}_{-0.046}$	$0.044^{+0.084}_{-0.054}$	$-0.050^{+0.089}_{-0.086}$
A_D	Dilution	–	–	0.0001 ± 0.0016
Telescope Parameters:			CHIRON	
$\gamma_{\rm rel}$	RV Offset (m/s)		31130 ± 150	
σ_J	RV Jitter (m/s)		$0.00^{+400}_{-0.00}$	
σ_J^2	RV Jitter Variance		$-30000^{+190000}_{-130000}$	
Transit Parameters:		TESS (30-min)	TESS (2-min)	
σ^2	Added Variance	$4.5^{+2.2}_{-1.77} \times 10^{-9}$	$1.6^{+5.5}_{-5.1} \times 10^{-9}$	
F_0	Baseline flux	1.000011 ± 0.000014	1.000045 ± 0.000014	

of the ground-based light curves, as well as the fact that systematics in ground-based observations can imitate the effects of gravity darkening.

In both fits, we adopted Gaussian priors based on the `EXOFASTv2` outputs where possible. We reparameterized the LDCs u_1, u_2 taken directly from the Claret (2017) tables according to Kipping (2013) and adopted Gaussian priors with standard deviations of 0.5 and 0.1 respectively. We used wide uniform priors on the period, time of conjunction, and planetary radius in addition to a uniform prior ranging from -1 to 1 on $\sqrt{e}\cos\omega$ and $\sqrt{e}\sin\omega$. We also used a wide uniform prior on the impact parameter b for both fits. However, in the case of the gravity darkening fit, we allowed b to also sample negative values as we can no longer assume a symmetric stellar disk. Finally, we fixed the gravity darkening exponent β according to Claret (2016).

We found that both of these fits are in good agreement with our global `EXOFASTv2` fit as all parameters commonly fit among the 3 methods agreed within 2 sigma. We found no significant asymmetries induced by gravity darkening, and therefore we adopt the results from our global `EXOFASTv2` fit. While our gravity darkening fit is unable to strongly constrain the alignment, the fit favors a potential large misalignment. We encourage additional characterization through Doppler tomography or Rossiter-McLaughlin techniques in order to further constrain the orbital architecture of the HIP 33609 system.

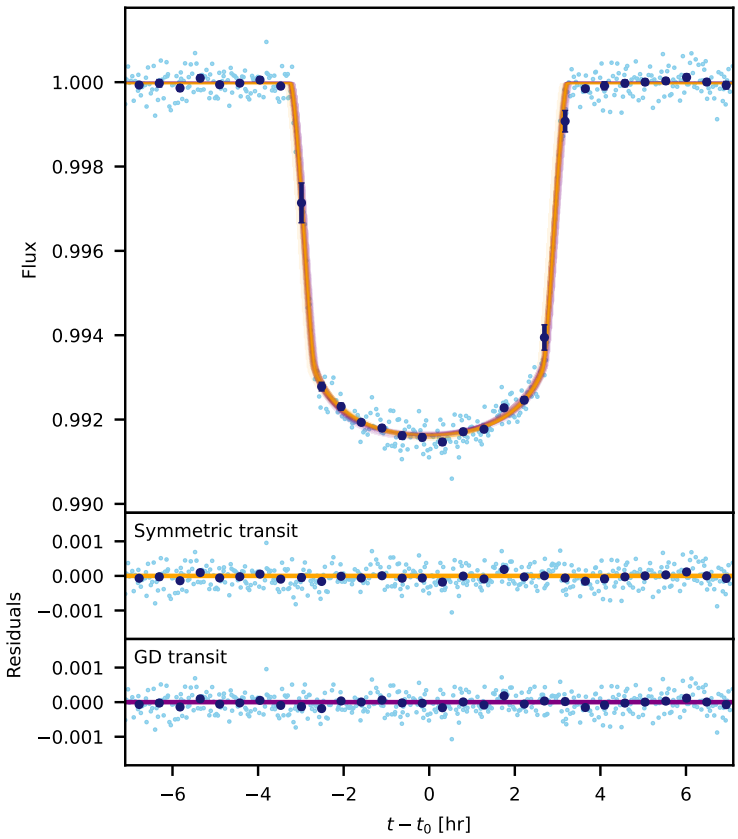

Figure 2.7 (Top) The TESS transits for HIP 33609 bphase-folded and binned to 30-minutes. 32 independent draws from the posteriors of the symmetric Mandel & Agol (2002) fit are plotted in orange, and 32 independent draws from the gravity darkening fit (Hooton et al., 2022) are plotted in purple (see §2.5.2). While the median models are very similar betwen the two fits, we note the slight asymmetries seen in the gravity darkening posteriors hint at a potential misalignment.

2.5.3 CEPAM Evolutionary Models

Using CEPAM (Guillot & Morel, 1995), we calculate evolutionary tracks of HIP 33609 b. Our models are based on the same approach as in Bouchy et al. (2011), using the analytical atmospheric boundary conditions from Guillot (2010). Our fiducial model has a solar metallicity interior ($Z^*_{\rm interior} = Z_\odot$) and thermal and visible mean opacities set to $\kappa^*_{\rm th} = 0.04\,{\rm g\,cm^{-2}}$ and $\kappa^*_{\rm v} = 0.024\,{\rm g\,cm^{-2}}$, respectively. As shown in Fig. 2.8, this model reproduces the observed radius for the age of HIP 33609 b. Because of the brown dwarf's large mass and intrinsic luminosity ($L_{\rm int} = 4 \times 10^{30}$ erg/s), we find that the interior is entirely convective and therefore its evolution is not affected by changes of the interior opacities. The energy supplied by tidal dissipation,

$L_{\rm tides} \approx 10^{25}$ erg/s for a tidal quality factor ($Q' = 10^6$) (e.g., Bodenheimer et al., 2001), is also too low to affect the evolution, as is that due to internal dissipation $L_{\rm dissipation} \approx 10^{27}$ erg/s (see Thorngren & Fortney, 2018).

The radius of HIP 33609 b is thus mainly affected by three factors: the initial formation entropy (here we assume a hot start initial entropy of $S = 13.4$ k_B/baryon), the deep interior mean molecular weight and the atmospheric opacity (see Guillot, 2005). Figure 2.8 shows that the latter is by far the dominant effect: when multiplying the atmospheric opacities by 2 over their fiducial values, we obtain a theoretical radius that is 25% larger (at the measured age) than our fiducial model and clearly incompatible with the observations. On the other hand, when multiplying the interior metallicity by a factor 5 (equivalent to adding 4.2 $M_{\rm Jup}$ of heavy elements in its interior) the radius change remains limited. Although a wider ensemble of dedicated evolution models should be calculated, this already shows that observations of HIP 33609 b with the James Webb Space Telescope (JWST) would be extremely important, by independently yielding its atmospheric metallicity (that we predict should be solar) and intrinsic luminosity (our evolution models predict $T_{\rm eff} = 2630$ K

2.6 Discussion

HIP 33609 b joins a population of 37 transiting BDs published to date (Grieves et al., 2021; Carmichael et al., 2022; Psaridi et al., 2022; Sebastian et al., 2022), and is one of the most extreme sub-stellar companions yet discovered. HIP 33609 not only has a precise age measurement of 150±25 Myr, but is also the brightest and hottest host of a transiting BD discovered to date. The unique combination of host star and BD parameters (see Figure 2.9) make the HIP 33609 system a benchmark for testing theories of substellar evolution, BD orbital dynamics, and the effects of insolation on BD atmospheres.

The HIP 33609 system also extends our knowledge of transiting companions around hot stars. All previously discovered transiting companions around B- and A-type stars have orbital periods less than 10 days (Addison et al., 2021; Anderson et al., 2018; Dorval et al., 2020; Gaudi et al., 2017; Giacalone et al., 2022; Hellier et al., 2019; Johnson et al., 2018; Lund et al., 2017; Morton

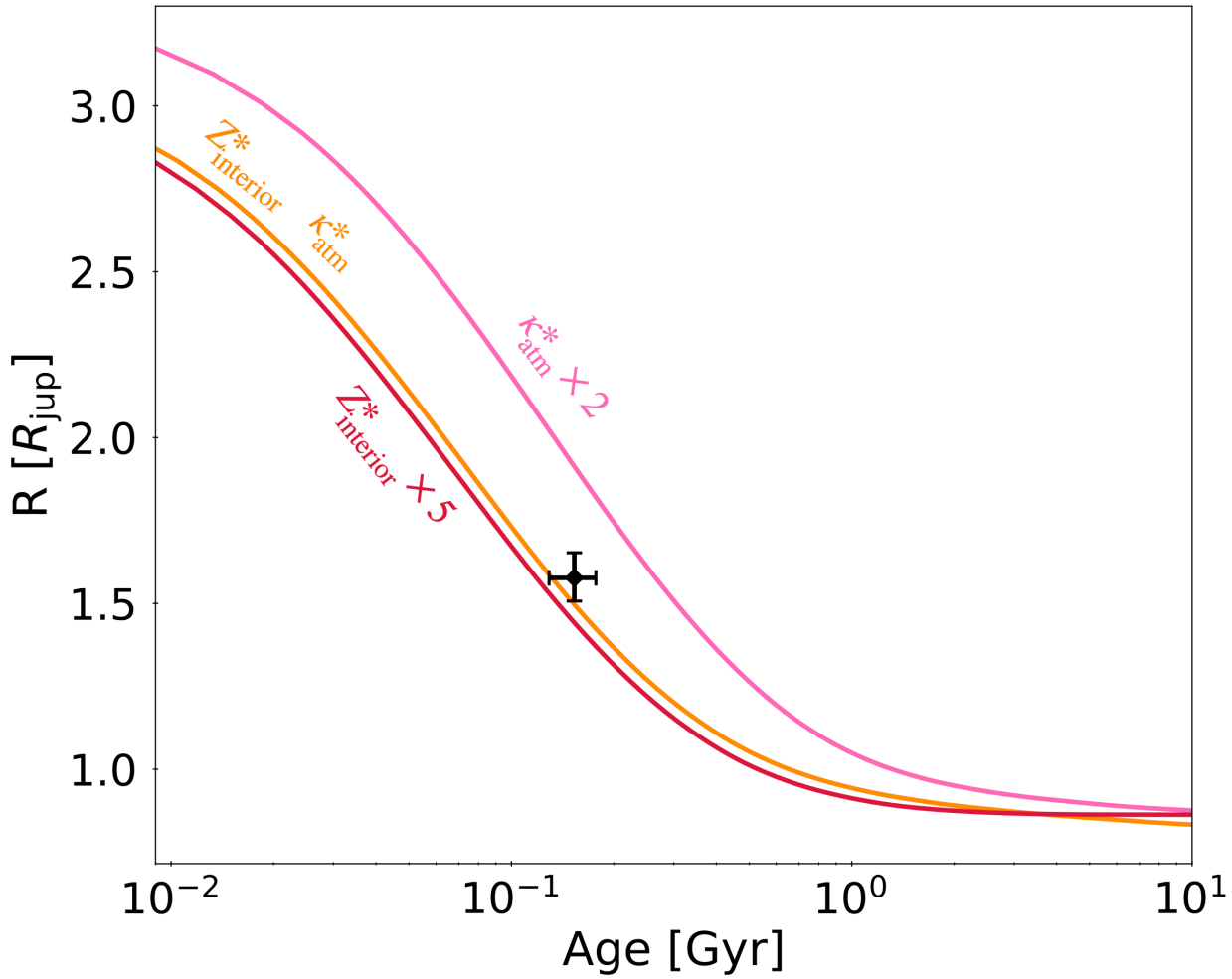

Figure 2.8 The radius evolution of HIP 33609 b. The black point signifies the measured age and radius with 1σ error bars. The orange line is our fiducial evolutionary model (see §2.5.3). The pink line multiplies the atmospheric opacities of the fiducial model by 2, and the red line multiplies the interior metallicity by 5.

et al., 2016; Shporer et al., 2014; Stevens et al., 2020; Talens et al., 2017; Zhou et al., 2019a), whereas HIP 33609 provides the first companion on a long period orbit (~39 days).

2.6.1 Placing HIP 33609 in Context

HIP 33609 b orbits a bright (V = 7.3) B-star with a precisely measured age, and joins a growing population of 12 BDs with host stars above the Kraft break (~6250 K, Kraft, 1967), an exciting regime for studying BD evolution in the context of star-like versus planet-like formation. For example, if BDs do indeed follow formation and evolutionary pathways similar to the giant planets, then we can draw comparisons to recent studies focused on hot Jupiters that have observed a

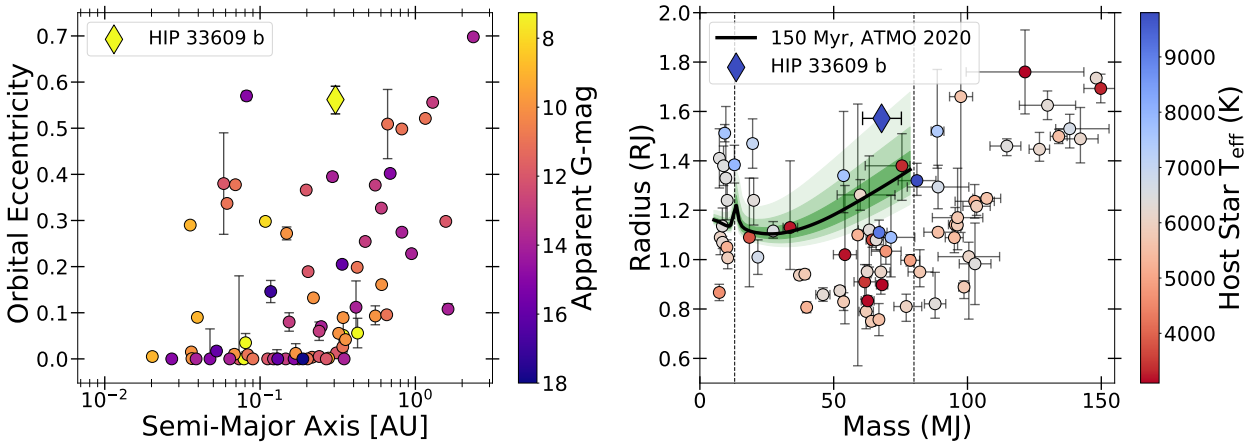

Figure 2.9 (Left) The population of stellar companions ranging from 7-150 M_J in eccentricity and semi-major axis, colored by the apparent magnitude. (Right) The same population in radius and mass, colored by the effective temperature of the host star. Vertical lines at 13 M_J and 80 M_J denote the traditional boundaries of the BD regime. The solid black line shows the ATMO 2020 substellar evolutionary model (Phillips et al., 2020) for HIP 33609 b's measured age (150±25 Myr) with the green shaded regions depicting the 1, 2, and 3σ uncertainties. **Note:** systems where the primary body is a BD or white dwarf are not included. **References:** (Bakos et al., 2010; Buchhave et al., 2011; Tingley et al., 2011; Parviainen et al., 2014; Bonomo et al., 2015; Esteves et al., 2015; Stassun et al., 2017; Bento et al., 2018; Cooke et al., 2020; Cortés-Zuleta et al., 2020; Grieves et al., 2021; Carmichael et al., 2022; Gill et al., 2022; NASA Exoplanet Archive, 2022; Psaridi et al., 2022; Sebastian et al., 2022)

.

discontinuity in stellar obliquity at the Kraft break (Winn et al., 2010a; Schlaufman, 2010). **?** suggest that this discontinuity may only exist for the low eccentricity population, a trend which would provide strong evidence for high eccentricity migration as the dominant migration mechanism for hot Jupiters. This hypothesis is also supported by the current population of *TESS* discovered giant planets (Rodriguez et al., 2023; Yee et al., 2022). If BDs and giant planets undergo similar migratory processes, then they could exhibit the same discontinuity in stellar obliquity. HIP 33609 b's high eccentricity ($e = 0.560^{+0.029}_{-0.031}$) makes it the second most eccentric BD behind KOI-415 (e = 0.698) (Moutou et al., 2013). However, HIP 33609 is significantly more accessible to follow-up because it is more than 500 times brighter than KOI-415 (V = 14.2).

Furthermore, HIP 33609 b's radius is among the largest for transiting BDs at $R_b = 1.580^{+0.074}_{-0.070}$ R_J. Substellar evolutionary models predict that BDs form highly inflated and then contract, rapidly at first, then slowing over the course of ~10 Gyr (Baraffe et al., 2003; Saumon & Marley, 2008;

Burrows et al., 2001; Phillips et al., 2020). HIP 33609 b's large radius is consistent within 3σ for substellar models at the estimated age from our analysis using both CEPAM (Figure 2.8) and the ATMO 2020 models (Figure 2.9).

2.6.2 Future Characterization Prospects

As the brightest and hottest host star for a transiting BD, the HIP 33609 system is well-situated for future characterization via ground-based observations. Although the long transit duration (~6.5 hours) will make spin-orbit alignment measurements challenging, HIP 33609 b would be a valuable addition to the population of BDs with well-constrained stellar obliquities.

We predict a Rossiter-Mclaughlin semi-amplitude to first order of 270 m/s for HIP 33609 b using the methods in Triaud (2018). While this is indeed well below our typical radial velocity uncertainty of ~1000 m/s with CHIRON, we expect orbital obliquity measurements to be more accessible to Doppler Tomographic techniques (Zhou et al., 2016; Collier Cameron et al., 2010) given that we can resolve the rotation of the host star. A finding that HIP 33609 b is highly misaligned, as tentatively indicated by our gravity darkening fit, would provide strong evidence for a dynamically active history. We also encourage future measurements of more BD obliquities in general, in order to provide insight into BD evolutionary pathways similar to that obtained from the obliquity studies of hot Jupiters discussed in §2.6.1.

HIP 33609 b is also a prime candidate for studying the effects of insolation on BD and giant planet atmospheres. As a long period, massive companion, it can thereby extend the extensive studies of the irradiated atmospheres of BDs and giant planets. The BD KELT-1 b (Siverd et al., 2012; Beatty et al., 2014; von Essen et al., 2021), and giant planets KELT-9 b (Gaudi et al., 2017; Yan & Henning, 2018; Hoeijmakers et al., 2018) and TOI-1431 b (Stangret et al., 2021) are all ultrahot (T_{eq} > 2000 K) companions with well-studied atmospheres that receive approximately 10 times more incident flux than HIP 33609 b.

2.7 Conclusion

In this paper, we present the discovery of a benchmark transiting BD in the HIP 33609system. We use a combination of spectroscopic and photometric observations from both ground- and space-

based facilities in order to characterize the host star and transiting BD. HIP 33609is a bright (V = 7.3), rapidly rotating B-star with an effective temperature of $T_{\rm eff} = 10,400^{+800}_{-660}$ K. HIP 33609 bis an inflated BD with a radius of $R_b = 1.580^{+0.074}_{-0.070}\ R_J$ and a mass of $M_b = 68.0^{+7.4}_{-7.1}\ M_J$ on a long period (P = 39.47 days), eccentric orbit ($e = 0.560^{+0.029}_{-0.031}$). We also present the discovery of MELANGE-6, a new, young stellar association, of which HIP 33609is shown to be a member. We determine the age of the association (and hence HIP 33609) to be 150±25 Myr. Thus, the HIP 33609system is an ideal candidate for testing substellar evolutionary models, as well as for a comparative analysis relative to the extensive population of highly irradiated, short period BDs and giant planets. We encourage the pursuit of stellar obliquity measurements for HIP 33609 band the transiting BD population as a whole in order to provide more insight into the formation and evolutionary history of transiting BDs.

CHAPTER 3

THE OATMEAL SURVEY. III. AN ALIGNED TRANSITING WARM BROWN DWARF AND EVIDENCE FOR QUIESCENT BROWN DWARF MIGRATION

This chapter's work was published in Vowell et al. (2026).

3.1 Abstract

We present the first measurement of the sky-projected orbital obliquity of a benchmark transiting brown dwarf host, HIP 33609, as a part of the Orbital Architectures of Transiting Massive Exoplanets And Low-mass stars (OATMEAL) survey. HIP 33609 b is an eccentric, 68 M_J brown dwarf orbiting a 10 300 K, A-type star with an orbital period of 39 days. Its host star is a known member of the 150 Myr old MELANGE-6 moving group, making it an excellent laboratory for testing sub-stellar evolutionary models. Using in-transit spectra collected by the Planet Finder Spectrograph (PFS) on the Magellan II Clay 6.5 m telescope, we measured a sky-projected orbital obliquity of $|\lambda| = 12.7 \pm 1.3°$. The mass of the brown dwarf is most consistent with a stellar-like fragmentation formation history followed by a period of migration. Given the eccentricity ($e = 0.557$) but low orbital obliquity of the brown dwarf, we claim that coplanar high eccentricity tidal migration seems to be the most plausible pathway, however, it remains difficult to conclusively rule out other migration mechanisms. The low orbital obliquity for HIP 33609 is consistent with previous measurements of high mass-ratio companions, and bears a striking resemblance to the obliquity distribution of transiting warm Jupiters. We suggest brown dwarfs may follow a dynamically quiescent migration pathway, consistent with them forming in isolated conditions.

3.2 Introduction

Brown dwarfs (BDs) have traditionally been distinguished from giant planets and stars by the presence (and type) of fusion that occurs in their cores. Planets are generally not massive enough to ignite nuclear fusion, whereas stars undergo hydrogen fusion. BDs, which lie between these two regimes in mass, are only massive enough to fuse deuterium in their cores, a heavy isotope of hydrogen composed of one proton and one neutron. Nominally, this translates to a boundary of 13 M_J to ignite deuterium fusion (Spiegel et al., 2011) and 80 M_J to ignite hydrogen fusion (Baraffe

et al., 2003). While this fusion-based definition is useful for understanding the underlying physics operating in their interiors, these objects can also be understood based on how they form and evolve. From the perspective of formation, there are generally two pathways: objects that form via core accretion (planet-like; Pollack et al., 1996), and objects that form via gravitational instability (star-like; Adams et al., 1989; Bate, 2012; Kratter & Lodato, 2016). Objects in the canonical BD regime can theoretically form through either formation channel, but it is not yet clear under what conditions each mechanism dominates.

Although differentiating between these mechanisms remains challenging for any individual BD, a large enough population of objects may show trends that favor one mechanism over the other. Several recent studies have attempted to explore this with different BD populations. Ma & Ge (2014) used the radial velocity (RV) and transit detections at the time to show that brown dwarf architectures support a 42.5 M_J transition between planet-like and star-like formation pathways. Schlaufman (2018) used an updated sample to explore host star metallicities, finding evidence for a much lower ~4 M_J transition point. Bowler et al. (2020, 2023) showed that directly imaged giant planets on widely separated orbits have very different architectures than their BD counterparts. Specifically, they found that the relative alignment of the companion's orbital plane to its host star's rotation axis (commonly referred to as stellar obliquity) is often much larger for BD companions than giant planets. The authors claim that this trend is supportive of two distinct formation channels since hydrodynamical simulations show that binaries formed via fragmentation can often form with high misalignments (Bate et al., 2010; Offner et al., 2016).

In the era of NASA's Transiting Exoplanet Survey Satellite (*TESS*; Ricker et al., 2015) mission, the population of transiting BD systems continued to grow in the wake of recent discoveries (e.g. Grieves et al., 2021; Carmichael et al., 2022; Henderson et al., 2024a; Vowell et al., 2025). With more than 50 transiting BDs now discovered, the population has just grown large enough to begin searching for trends without being biased by a small sample size. One of the most anticipated parameters to explore in search of trends that can be tied to formation is stellar obliquity because of its usefulness in distinguishing the evolutionary pathways of close-in giant planets (Rice et al.,

2022a) as well as widely-separated massive companions (Bowler et al., 2023). However, only 10 transiting BDs have had their stellar obliquity directly measured so far (Triaud et al., 2009; Siverd et al., 2012; Triaud et al., 2013; Zhou et al., 2019b; Giacalone et al., 2024; Ferreira dos Santos et al., 2024; Brady et al., 2025; Doyle et al., 2025; Rusznak et al., 2025; Carmichael et al., 2025). 4 of these systems have eccentric orbits and all 10 of them lie on orbital periods $P < 10$ days. Overall, the transiting BDs exhibit a strong preference for alignment among single-star hosts (Rusznak et al., 2025).

The stellar obliquity of transiting companions is typically measured through the Rossiter-McLaughlin (RM) effect (Rossiter, 1924; McLaughlin, 1924), an observed RV shift that occurs during a companion's transit. This observed RV shift is directly tied to the specific transit chord that is traced on the stellar surface by the transiting companion. As the companion transits, the local rotational velocity where the stellar surface is blocked will not contribute to the broadened line profile. The resulting distortion of line shape causes the apparent RV shift. This effect becomes less observable in rapidly rotating stars due to excessive broadening of the star's spectral lines; however, in some cases, the stellar obliquity can still be retrieved with techniques that measure the distortion of the spectral lines themselves rather than the induced RV shift (e.g. Doppler Tomography; Collier Cameron et al. 2010, Reloaded Rossiter-McLaughlin; Cegla et al. 2016). Here, we present a new stellar obliquity measurement for a transiting brown dwarf, HIP 33609 b, using the Doppler Tomography[1] technique.

HIP 33609 b is a benchmark young (150 Myr) transiting brown dwarf in the comoving group MELANGE-6 (Vowell et al., 2023). It orbits a bright, $V = 7.3$ mag host star making it easily accessible for follow-up characterization. It also lies on a 39-day, eccentric orbit. This architecture is consistent with a dynamically active past which is theorized to also produce potentially large misalignments (Kozai, 1962; Lidov, 1962; Rasio & Ford, 1996; Chatterjee et al., 2008; Wu & Lithwick, 2011b). These factors make HIP 33609 an ideal candidate to probe for misalignment since it is also tidally detached and therefore would not have had any potential misalignment

[1]Doppler Tomography is also sometimes referred to as the Doppler Shadow technique.

dampened by tidal interactions. This paper is structured as follows: in §3.3 we present the archival and in-transit spectroscopic observations of HIP 33609 b used in our analysis. We describe our analysis of these data to measure the stellar obliquity in §3.4. In §3.5 we discuss the most probable formation and evolutionary pathways for HIP 33609 b given it's newly measured stellar obliquity, and we place this system in context with the population of previously measured giant planet and BD stellar obliquities. Finally, we present our conclusions in §3.6.

3.3 Observations

Since the original discovery (see Vowell et al., 2023), *TESS* has reobserved HIP 33609 during Sectors 61, 87, and 88. Due to the long orbital period ($\sim$ 39 days), transits were only observed in Sectors 61 and 88. Unfortunately, the Sector 88 transit occurred during the spacecraft's momentum dump causing a period of unstable pointing which resulted in poor data quality. We therefore were only able to add the Sector 61 data to the data from Vowell et al. (2023) for our global analysis. The archival photometric and spectroscopic data reported in the original discovery, and the new transit from Sector 61 were collected and reduced according to Vowell et al. (2023).

We also observed a transit of HIP 33609 b with the Planet Finder Spectrograph (PFS) on the Magellan II Clay 6.5 m telescope (Crane et al., 2006, 2008, 2010) on the night of 2023-02-05 UTC to measure the sky-projected stellar obliquity of the system. Due to the long transit duration of HIP 33609 b ($\sim$ 6.5 hours), we were only able to observe the first half of the transit before the target fell too low in the sky to continue observing. The observations were taken using the $0.3^{"} \times 2.5^{"}$ slit with a resolving power of $R = 127,000$. We did not use the iodine cell. A total of 43 exposures were taken with an exposure time of 300 s. We reduced these spectra according to (Butler et al., 1996).

In order to measure the projected stellar obliquity, we utilized Doppler Tomography (Collier Cameron et al., 2010). This technique leverages the fact that a transiting companion will block out different parts of the host star's surface, which possess their own local rotational velocity. By tracking the companion's shadow projected on the host star's rotationally broadened line-profile, we were able to reconstruct the precise transit chord as a function of the local rotational velocity. To

do this, we first derived the line broadening profile with a least-squares deconvolution between the data and a synthetic spectrum based on the ATLAS9 model atmospheres (Castelli & Kurucz, 2003) which best matched the parameters of the host star. We calculated the local rotational velocity of the portion of the stellar surface being blocked out by subtracting the median combined line profile from the derived line profile. For a more in depth description of this process see Zhou et al. (2019b). We then fit this Doppler shadow to a model in order to constrain the projected orbital obliquity of the system, see §3.4.

3.4 Analysis and Results

We used `EXOFASTv2` (Eastman et al., 2019) to update the global fit performed in Vowell et al. (2023). Generally, we followed the same techniques described in Vowell et al. (2023) except that we chose not to include the ground-based photometry collected by the *TESS* Follow-up Observing Program (TFOP; Collins et al., 2018). Generally, these data are most useful during the confirmation process where they can rule out various false positive scenarios. They also often increase the precision of the ephemeris by extending the observational baseline, since the follow-up light curves are often collected after the most recent *TESS* observations. In this case however, the substellar nature of the transit signal has already been confirmed, and *TESS* has since revisited this field providing more data after the ground-based, follow-up data were collected. Hence, these follow-up data provide little value to the fit while simultaneously adding computational complexity, and we therefore choose not to include them in this analysis.

To briefly summarize the fitting process, we used archival photometry from Gaia Data Release 3 (DR3 Gaia Collaboration et al., 2023), 2MASS (Cutri et al., 2003; Skrutskie et al., 2006), and WISE (Wright et al., 2010; Cutri et al., 2012), in combination with the *TESS* light curves and radial velocities described in (Vowell et al., 2023). Using these data, we fit the host star using a combination of a Spectral Energy Distribution (SED) model and MESA Isochrones and Stellar Tracks (MIST). We also simultaneously fit the substellar companion by fitting the light curve and radial velocities to a Keplerian model. We placed the same Gaussian priors as Vowell et al. (2023) on the Gaia parallax, [Fe/H], and dilution in the *TESS* band. We also used the same uniform prior

Table 3.1 Median Values and 68% Confidence Intervals for Fitted Stellar and Companion Parameters.

Parameter	Description	Value
Priors		
π	Gaia parallax (mas)	$\mathcal{G}[6.4871, 0.0492]$
[Fe/H]	Metallicity (dex)	$\mathcal{G}[0.0, 0.5]$
A_V	V-band extinction (mag)	$\mathcal{U}[0, 0.0358]$
D_T	Dilution in *TESS*	$\mathcal{G}[0, 0.00162]$
Stellar Parameters		
M_*	Mass ($M_\odot$)	$2.375^{+0.098}_{-0.093}$
R_*	Radius ($R_\odot$)	$1.865^{+0.080}_{-0.075}$
L_*	Luminosity ($L_\odot$)	$35.6^{+10.0}_{-6.6}$
F_{Bol}	Bolometric Flux (cgs)	$4.78^{+1.4}_{-0.89} \times 10^{-8}$
ρ_*	Density (cgs)	$0.515^{+0.070}_{-0.061}$
$\log g$	Surface gravity (cgs)	$4.272^{+0.039}_{-0.037}$
$T_{\rm eff}$	Effective temperature (K)	10320^{+800}_{-620}
[Fe/H]	Metallicity (dex)	$0.01^{+0.18}_{-0.20}$
$[{\rm Fe/H}]_0$	Initial Metallicity	$0.03^{+0.17}_{-0.19}$
Age	Age (Gyr)	$0.153^{+0.024}_{-0.025}$
EEP	Equal Evolutionary Phase	$313.9^{+7.2}_{-7.3}$
A_V	V-band extinction (mag)	$0.125^{+0.078}_{-0.080}$
d	Distance (pc)	154.3 ± 1.2
Companion Parameters		
P	Period (days)	39.4718115 ± 0.0000072
R_P	Radius ($R_{\rm J}$)	$1.581^{+0.068}_{-0.064}$
M_P	Mass ($M_{\rm J}$)	$67.9^{+7.3}_{-7.2}$
T_C	Time of conjunction ($\rm BJD_{TDB}$)	$2459231.75945 \pm 0.00013$
T_0	Optimal Conjunction Time ($\rm BJD_{TDB}$)	$2459271.23166 \pm 0.00010$
a	Semi-major axis (AU)	$0.3054^{+0.0041}_{-0.0040}$
i	Inclination (degrees)	89.03 ± 0.12
e	Eccentricity	$0.557^{+0.029}_{-0.030}$
ω_*	Argument of periastron (degrees)	$167.4^{+5.1}_{-5.3}$
$T_{\rm eq}$	Equilibrium temperature (K)	1230^{+75}_{-57}
K	RV semi-amplitude (m/s)	2700 ± 290
R_P/R_*	Planet radius in stellar radii	$0.08709^{+0.00031}_{-0.00032}$
a/R_*	Semi-major axis in stellar radii	$35.2^{+1.5}_{-1.4}$
δ	$(R_P/R_*)^2$	0.007584 ± 0.000055
$\delta_{\rm TESS}$	Transit depth in TESS	0.00874 ± 0.00023
τ	Ingress/Egress duration (days)	$0.02481^{+0.00070}_{-0.00071}$
T_{14}	Total transit duration (days)	0.27057 ± 0.00061
b	Transit impact parameter	$0.369^{+0.029}_{-0.034}$

on the V-band extinction. We initialized the fit by placing starting points for each parameter at the median value reported in (Vowell et al., 2023). The posteriors resulting from this fit (see Table 3.1) agree with the posteriors in Vowell et al. (2023) to 1σ. We also improve the precision on the orbital period by nearly a factor of two due to the additional transit observed in Sector 61.

We then perform two separate fits to the Doppler shadow. For the first fit, we incorporated the posteriors from our `EXOFASTv2` global fit as priors on the Doppler shadow fit. Specifically, we applied Gaussian priors using the posteriors for mid-transit time (T_C), orbital period (P), R_P/R_*, impact parameter b, eccentricity (e) and argument of periastron (ω_*). For the second fit, we model each of these parameters together, incorporating the *TESS* lightcurves, CHIRON RVs and PFS spectra. Both fits incorporated the projected rotational velocity of the host star ($v \sin i_\star$) from Vowell et al. (2023) as a prior. We ran both fits according to the procedures outlined in Dong et al. (2022). To briefly summarize, we fit the Doppler shadow to a model created by calculating the planet's position on the stellar disk, as well as the local rotational velocity on stellar surface being blocked by the shadow. Then, we convolved this with a Gaussian velocity profile representing the resolution of the spectrograph and macroturbulence of the star. This normalized planetary velocity was then compared to the observed Doppler shadow to calculate the likelihood.

We modeled the Doppler shadow using the `PyMC` package with the No-U-Turn Sampler (NUTS) for posterior inference. We ran four independent Markov chains, each with 5000 tuning steps followed by 3000 draws. All model parameters achieved $\hat{R} < 1.01$, indicating good convergence of the posterior distributions. The posteriors from both these fits as well as the parameters they shared with the global `EXOFASTv2` fit were all consistent with each other within 1σ. We adopted the results from the second fit, which simultaneously models all parameters, as it incorporates the full data set. The resulting stellar obliquity from that fit was $|\lambda| = 12.7 \pm 1.3°$.

3.5 Discussion

HIP 33609 b is now the 11th transiting BD with a measured sky-projected stellar obliquity (see Figure 3.2), and within this population, it has both the longest orbital period ($\sim$ 39 days) and the hottest host star ($T_{\rm eff}$ = 10 300 K). These factors, combined with the young age (150 ± 25

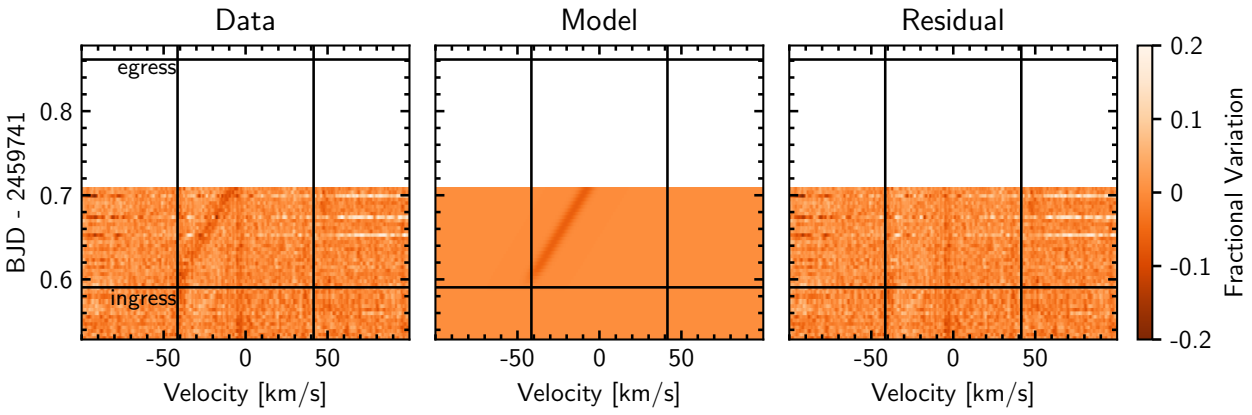

Figure 3.1 Doppler shadow analysis of HIP 33609 b. We note that only the first half of the transit was observed as discussed in §3.3. The left, middle, and right panels show the reduced data, best-fit model, and residuals (data minus model), respectively. The horizontal lines indicate the times of ingress and egress, while the vertical lines mark the projected stellar rotational velocity limits, $\pm v \sin i$. The color scale represents the fractional variation in flux.

Myr) constrained via cluster membership means that HIP 33609 b has likely not undergone any significant tidal realignment. Hot stars ($T_{\rm eff} > 6250$) have been shown to be less efficient at realigning transiting hot Jupiters, even on Gyr timescales (Rice et al., 2022a), and HIP 33609 b is several factors further from its host star ($a/R_* = 35.2^{+1.5}_{-1.4}$) than most hot Jupiters. The timescale for tidal realignment is a strong function a/R_*, see Equation 3 in Giacalone et al. (2024) adapted from Zahn (1975, 1977); Albrecht et al. (2012), so HIP 33609 b's architecture and age can rule out any significant tidal realignment. Given that lack of tidal influence, we examine the formation and evolution of the BD companion below. We also place this system in context with previously measured giant planet and BD stellar obliquities, noting the similarities between the BD and warm Jupiter stellar obliquity distributions.

3.5.1 HIP 33609 b Evolutionary History

While it remains challenging to discern between planet-like formation (core accretion) and stellar-like formation (disk fragmentation) for any individual transiting BD, the measurement of HIP 33609 b's sky-projected orbital obliquity, provides yet another piece of the puzzle for understanding its evolutionary history. By combining this measurement with the other known properties of the HIP 33609 system, we can hone in a probable evolutionary pathway. First, with a mass of 68 M_J, the core accretion formation mechanism is unlikely (Mordasini et al., 2009). This is mainly due to

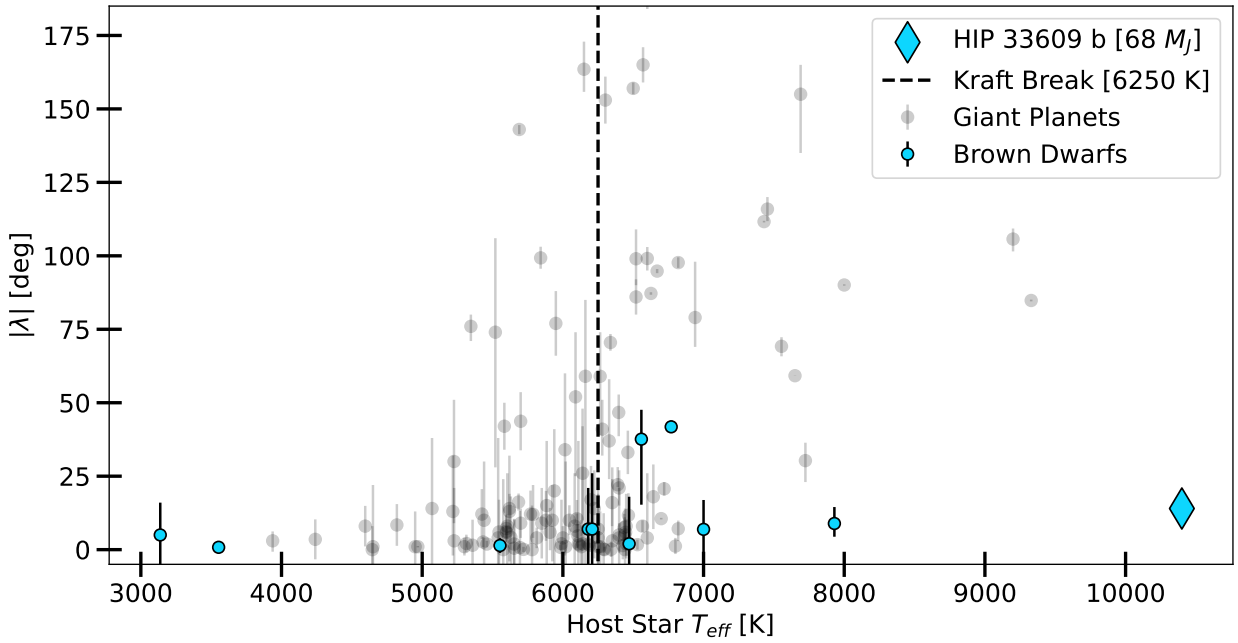

Figure 3.2 The sky-projected stellar obliquity vs. host star $T_{\rm eff}$ for transiting companions ranging $0.7 < M_b < 80\ M_{\rm J}$. The vertical dashed line at 6250 K marks the Kraft break (Kraft, 1967). Giant planets planets (gray) transition from low to high stellar obliquity at the Kraft break, whereas BDs (blue) exhibit low stellar obliquity regardless of their host star's effective temperature. HIP 33609 b stands out as the hottest stellar obliquity measurement to date and is denoted by the blue diamond. All data for this figure were retrieved using TEPCat (Southworth, 2011).

the limited lifetime of the circumstellar disk around FGK type stars which truncates the runaway gas accretion phase, inhibiting planet growth past $\sim 20\ M_J$ (Mordasini et al., 2012). In the case of HIP 33609, the disk lifetime is expected to be even shorter than typical transiting BD hosts due to its more massive host star which would further inhibit growth via core accretion (Richert et al., 2018). This fact alone makes disk fragmentation the more likely culprit behind the formation of HIP 33609 b.

However, both disk fragmentation and core accretion struggle to directly reproduce the current architecture of the HIP 33609 system at birth. In the case of core accretion, the formation of massive planets becomes inefficient when the semi-major axis a < 1 AU (Dawson & Johnson, 2018). Similarly, stellar companions on comparable orbits are also rare at birth (Moe & Di Stefano, 2017). Therefore, both scenarios require migration to explain the current architecture. The eccentricity of the BD (e = 0.56) offers some clues into its migration history. For example, high eccentricity

tidal migration triggered by a nearby massive companion could explain the eccentric orbit. These include Kozai-Lidov oscillations (Kozai, 1962; Lidov, 1962), planet-planet scattering (Rasio & Ford, 1996; Chatterjee et al., 2008), and secular interactions (Petrovich, 2015; Wu & Lithwick, 2011b) which are often invoked to explain the origins of short-period giant planets (Dawson & Johnson, 2018). Recent studies have shown that interactions between the protoplanetary disk and a massive planet or BD can also produce eccentric orbits (Li & Lai, 2023; Romanova et al., 2023). In this scenario, an eccentric HIP 33609 b would be massive enough to torque the protoplanetary disk, which could also induce migration.

Stellar mass companions with orbital periods P < 100 days are also thought to migrate through the same dynamical and secular interactions as the hot Jupiters (Moe & Di Stefano, 2017). In other words, the mechanism of HIP 33609 b's migration should be agnostic of its formation mechanism. Distinguishing between the various migration pathways described above requires additional information. For example, the interactions that require the presence of some other companion capable of driving up the eccentricity can favored when an outer companion is detected. However, we did not detect any nearby companions in the high resolution imaging, nor any additional transits in the *TESS* photometry. The Gaia Re-normalized Unit Weight Error (RUWE) is low (RUWE = 0.97), signifying that the Gaia astrometric solution is well-described by a single component. The radial velocities also show no sign of a longer term trend over the 3 observational epochs spanning ~2 years that may indicate outer bodies. While we are able to rule out additional short-period, large transiting companions, and widely-separated, bright companions, there is still ample parameter space where a companion of at least M-dwarf mass could reside and remain undetected by the available data. Such a companion would certainly be capable of inducing the migration of HIP 33609 b. Thus high eccentricity migration is still plausible given the ample parameter space to hide a massive companion.

Knowledge of the relative alignment of the companion's orbit can also help illuminate migration history since, each of the dynamical interactions discussed above predict unique stellar obliquity distributions. Therefore, we can attempt to rule out mechanisms that are inconsistent with HIP

33609 b's measured orbital obliquity. Kozai-Lidov predicts a bimodal distribution with peaks at 60° and 120° (Fabrycky & Tremaine, 2007) whereas scattering results in a more uniform distribution of stellar obliquities (Chatterjee et al., 2008). Secular chaos tends to induce moderate, prograde stellar obliquities (Wu & Lithwick, 2011b), and coplanar high eccentricity migration tends to keeps stellar obliquity low (Petrovich, 2015). The companion-disk interactions described in Li & Lai (2023); Romanova et al. (2023) are restricted to the plane of the disk. We measured a sky-projected orbital obliquity of $|\lambda| = 12.7 \pm 1.3°$, and note that it is unlikely that HIP 33609 b could have undergone significant tidal realignment. Given the system's young age (150 Myr), relatively wide separation ($a/R_* = 35.2$), and host star effective temperature ($T_{\rm eff} = 10,300$) it would not have had enough time to realign under equilibrium-tide theory (Winn et al., 2010b) or via resonance locking (Zanazzi et al., 2024). Thus, HIP 33609 b's stellar obliquity appears most consistent with coplanar high eccentricity migration, however, it's difficult to completely rule out other migration pathways. Detecting another massive companion in the system would provide strong evidence in favor of a dynamically hot migration mechanism, and indeed the multiplicity frequency for HIP 33609-like stars with late A/early B spectral types is roughly 85% (Moe & Di Stefano, 2017). While *TESS* will not reobserve this system in year 8, it may be reobserved in a potential 3rd extended mission allowing for the possibility to detect a transit from an outer long-period companion. Similarly, continuous RV monitoring of the system may uncover a long period trend indicative of another massive body as well. The upcoming Gaia Data Release 4 (expected December 2026) may also find evidence of a massive outer companion via detection an astrometric acceleration by virtue of its longer 66 month baseline.

3.5.2 Evidence for Quiescent Transiting BD Migration

HIP 33609 b is now the 11th transiting BD with a measured stellar obliquity. It also orbits the hottest host star for which this measurement has been made. This measurement continues the trend presented Giacalone et al. (2024); Doyle et al. (2025); Rusznak et al. (2025), which noted that BD companions tend to have significantly lower stellar obliquities than their less massive counterparts (e.g. hot Jupiters), regardless of their host's effective temperature. This is initially perplexing,

since transiting BDs are expected to have migrated to their present-day locations under the same mechanisms as hot Jupiters. This is because migration is generally agnostic to the mass of the system, with the same phenomena applying for giant planets up to stellar binaries (Moe & Di Stefano, 2017; Dawson & Johnson, 2018). The hot Jupiter orbital obliquity distribution, which transitions from low stellar obliquity to high at the Kraft break ($\sim 6250\ K$ Kraft, 1967). This has be explained by the fact that hot stars cannot efficiently realign their companions due to their lack of a convective envelope. Under equilibrium-tide theory, realignment results from the interaction between the orbit of the companion and the convective zone of the star (Winn et al., 2010b; Rice et al., 2022a). The combined distributions of hot Jupiter stellar obliquities and eccentricities have been cited as evidence of high eccentricity migration being the dominant migration mechanism (Rice et al., 2022a). If the transiting BDs migrate predominately by the same mechanisms, then we might expect them to have similar architectures, which vitally includes their orbital obliquities. However, transiting BDs seem to be significantly more aligned with 9 of the 11 total obliquity measurements being consistent with 0 to 3σ. This is suggestive that their migration pathways may be distinct, see Figure 3.3.

One possible explanation is presented in Rusznak et al. (2025) where they claim that low mass-ratio companions ($M_P/M_* < 2\times10^{-3}$) may form in compact multiplanet systems where dynamical instabilities capable of driving misalignment are common. Higher mass-ratio companions, on the other hand, may form in more isolated environments that lack massive nearby companions capable of perturbing the growing BD onto an inclined orbit. Therefore, the companion remains in the disk where it can continue to accrete and grow undisturbed. Indeed, the distribution of giant planet and brown dwarf stellar obliquities is consistent with this framework, including our new measurement for HIP 33609 b. However, this mechanism only explains the primordial alignment of these systems, not their subsequent migration, which, as noted above in §3.5.1, is required to observe them in their current configurations. Hence, it remains an open question to explain the orbital architectures of transiting BDs since they still need to migrate close to their host stars, but without exciting significant orbital obliquities. Superficially, this appears similar to recent trends

emerging in the warm Jupiter population.

Rice et al. (2022b) and Wang et al. (2024) showed that the warm Jupiters around single stars are more aligned than the hot Jupiter population regardless of their host star's effective temperature. Since the warm Jupiters orbit farther and are tidally detached, they should not undergo significant tidal realignment. Both studies also note evidence for primordial alignment among giant planets, suggesting that hot Jupiters migrate through some dynamically violent process that drives high stellar obliquity, whereas warm Jupiters may migrate more quiescently and, therefore, never become misaligned. This framework is also consistent with studies showing that warm Jupiters tend to have nearby companions significantly more frequently than hot Jupiters (Huang et al., 2016). Even more evidence that warm Jupiters seem to migrate quiescently, since any dynamically hot migration mechanism would have ejected nearby companions (Wu et al., 2023).

It is intriguing then that the BD obliquity distribution seems to more closely resemble the warm Jupiters (see Figure 3.4) given their relatively low stellar obliquities. While it is true that 6 warm Jupiters or BDs show large misalignments, they are almost entirely confined to systems with a detected outer stellar companion, which can explain their architectures. We restrict our discussion on the obliquity distribution resemblance between warm Jupiters and BDs to single-star systems to maintain consistency with the claims of Rice et al. (2022b) and Wang et al. (2024). Both studies noted that stellar companions have been shown to strongly influence stellar obliquity, often leading to large misalignments.

One potential interpretation of the similarity between warm Jupiter and transiting BD stellar obliquities would be that they undergo similar migration mechanisms. This would suggest that the transiting BDs migrate quiescently to their current, short-period orbits in order to retain their primordially low stellar obliquities. This interpretation is consistent with the hypothesis of Rusznak et al. (2025) wherein high mass-ratio companions form isolated due to the fact that isolated formation suggests no massive nearby bodies around to trigger a dynamical instability in the first place. If this is true and transiting BDs do indeed migrate quiescently (like warm Jupiters), then it should follow that they too would not disrupt the orbits of smaller planets with similar orbital separations to the

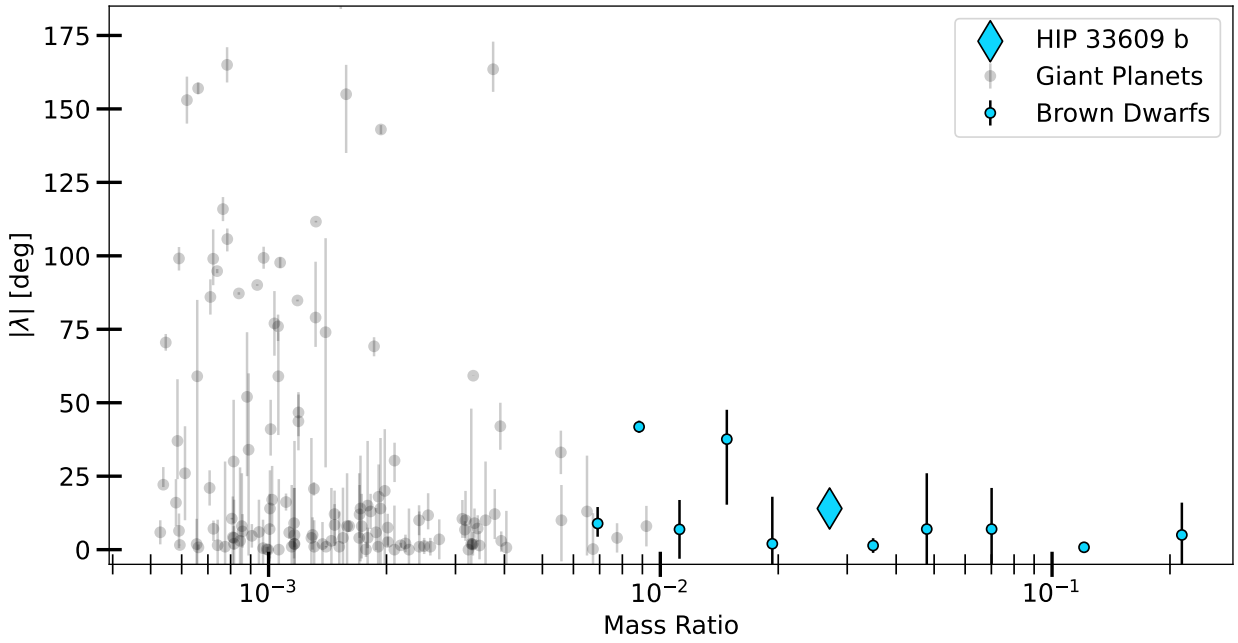

Figure 3.3 The sky-projected stellar obliquity vs. the mass ratio of the system for transiting companions ranging $0.7 < M_b < 80\ M_J$. Giant planets are shown as gray circles whereas BDs are blue circles. Our new measurement for HIP 33609 b is highlighted as the blue diamond. HIP 33609 b's stellar obliquity is consistent with the Rusznak et al. (2025) framework wherein high mass-ratio companions form isolated with low stellar obliquities.

BD (Huang et al., 2016). Therefore, one way to provide more evidence for quiescent BD migration would be to systematically search the current transiting BD population for these hypothetical small planets orbiting near the transiting BD to understand their occurrence rate.

3.6 Conclusion

We report the sky-projected orbital obliquity of $|\lambda| = 12.7 \pm 1.3°$ for the transiting BD HIP 33609 b. This marks the 11th transiting BD system for which this measurement has been made. It is also the hottest transiting BD host and longest BD orbital period for which a stellar obliquity measurement has been successful. Equipped with this measurement, and therefore a more complete understanding of the HIP 33609 system, we argued that a stellar-like fragmentation mechanism is the most likely formation channel followed by subsequent high eccentricity tidal migration. Ruling out any specific migration mechanism remains difficult, however, our stellar obliquity measurement appears most consistent with a coplanar high eccentricity migration mechanism. We found that our measurement continues the ongoing trend of low obliquity among high mass-ratio companions,

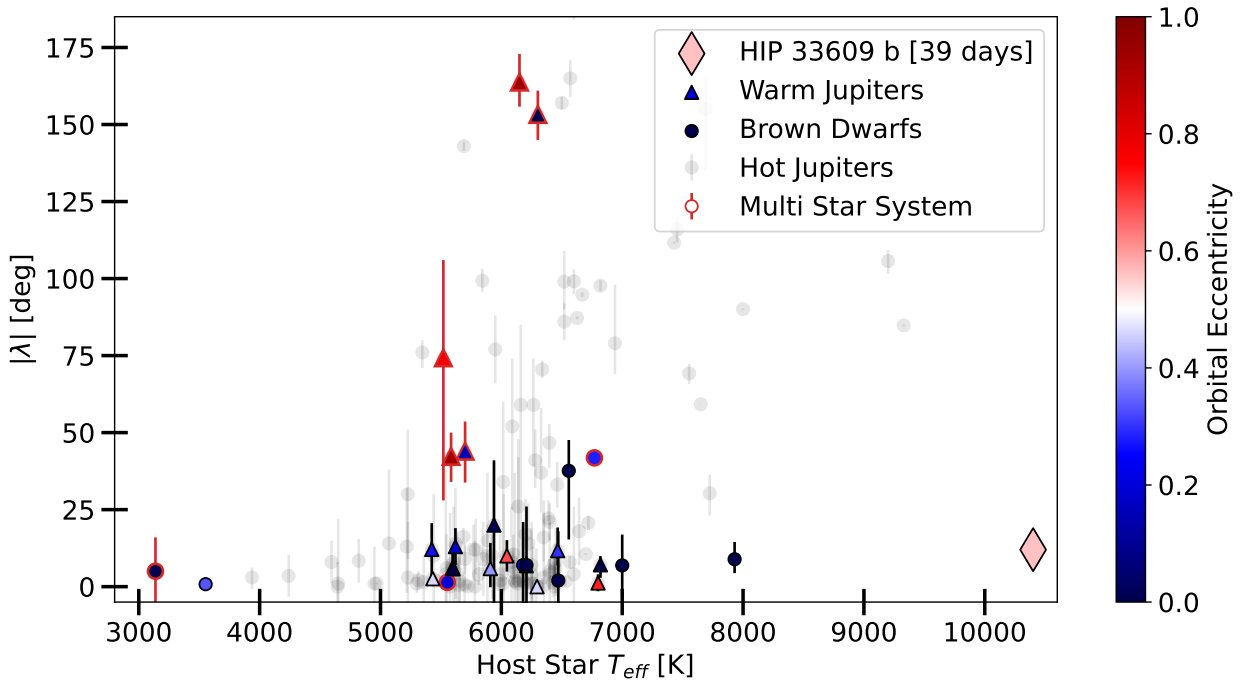

Figure 3.4 The sky-projected stellar obliquity vs. host star $T_{\rm eff}$ for transiting companions ranging $0.7 < M_b < 80\ M_{\rm J}$. Warm Jupiters are plotted in color as triangles and BDs as circles. Hot Jupiters are the gray background points. Warm Jupiters and BDs are colored based on their eccentricities. Systems with a detected outer stellar companion are highlighted with a red outline. Warm Jupiters and BDs orbiting single stars exhibit low stellar obliquities regardless of their host star's effective temperature and orbital eccentricity suggesting a potentially shared, quiescent migration pathway (see §3.5.2).

and note the similarity this distribution to the stellar obliquity measurements of warm Jupiters. We claimed that this similarity may be indicative of a shared migration history between the two populations which would imply that transiting BDs migrate relatively quiescently to their current day orbits. This idea is consistent with the results presented in Rusznak et al. (2025), which claimed that transiting BDs form isolated in the circumstellar disk. Finally, we propose future work to constrain the occurrence rate of nearby small planets to transiting BDs in order to further explore these systems' resemblance to the warm Jupiters.

CHAPTER 4

11 NEW TRANSITING BROWN DWARFS AND VERY LOW MASS STARS FROM *TESS*

The work presented in this chapter was published in Vowell et al. (2025)

4.1 Abstract

We present the discovery of 11 new transiting brown dwarfs and low-mass M-dwarfs from NASA's *TESS* mission: TOI-2844, TOI-3122, TOI-3577, TOI-3755, TOI-4462, TOI-4635, TOI-4737, TOI-4759, TOI-5240, TOI-5467, and TOI-5882. They consist of 5 brown dwarf companions and 6 very low-mass stellar companions ranging in mass from 25 M_J to 128 M_J. We used a combination of photometric time-series, spectroscopic, and high-resolution imaging follow-up as a part of the *TESS* Follow-up Observing Program (TFOP) to characterize each system. With over 50 transiting brown dwarfs confirmed, we now have a large enough sample to directly test different formation and evolutionary scenarios. We provide a renewed perspective on the transiting brown dwarf desert and its role in differentiating between planetary and stellar formation mechanisms. Our analysis of the eccentricity distribution for the transiting brown dwarf sample does not support previous claims of a transition between planetary and stellar formation at ~42 M_J. We also contribute a first look into the metallicity distribution of transiting companions in the range 7 – 150 M_J, showing that this does not support a ~42 M_J transition too. Finally, we also detect a significant lithium absorption feature in one of the brown dwarf hosts (TOI-5882). However, we determine that the host star is likely old based on rotation, kinematic, and photometric measurements. We therefore claim that TOI-5882 may be a candidate for planetary engulfment.

4.2 Introduction

Since the launch of NASA's Transiting Exoplanet Survey Satellite (*TESS*) in 2018 (Ricker et al., 2015), the number of brown dwarfs (BDs) known to transit their host stars has increased rapidly from just 16 systems to > 50. These BDs, which are defined as objects within the mass range of 13 - 80 M_J, fuse only deuterium in their cores. This differentiates them from planets, which undergo no fusion, and stars, which ignite hydrogen fusion. However, the deuterium and hydrogen burning limits have been shown to be less clear than this definition would imply. Spiegel et al.

(2011) showed that the lower limit varies from 11 - 16 M_J, while Baraffe et al. (2003) showed that hydrogen fusion can ignite between 75 - 80 M_J. The spread in both of these estimates can be explained by variation in the chemical composition and formation conditions of the BD. While these definitions provide insight into the physical processes taking place in BD interiors, they offer little insight into how they form.

Reframing our perspective on BDs into one motivated by formation and evolution has long been advocated for by some members of the BD community (Chabrier et al., 2014; Burrows, 2014; Carmichael et al., 2021), where objects would be distinguished based on whether they form through a planet-like or a star-like formation mechanism. BDs forming like planets would undergo a core accretion pathway (Pollack et al., 1996), commonly referred to as a "bottom-up" approach. The star-like BDs on the other hand would form via direct gravitational collapse, or "top-down", which can happen either within the circumstellar disk or at the core scale (Adams et al., 1989; Bate, 2012; Kratter & Lodato, 2016). Differentiating between these two formation pathways remains challenging, since it is unclear under what conditions each mechanism dominates, and whether there are any observable parameters that could distinguish them. Fortunately, in the era of *TESS*, we have begun to accumulate transiting BDs en masse, allowing us to pursue the question of BD formation from a different perspective. This budding population of transiting BDs is particularly enticing for studying BD formation because it provides a complementary, and in many cases, more complete understanding of the BD compared to the previously studied objects, which have primarily been discovered via direct imaging or radial velocity (RV) techniques. The transiting population serves as a complementary dataset to these other populations because transits provide a model independent measurement of BD radii, a property which often can only be otherwise inferred with evolutionary models based on the observed spectrum and luminosity. This measurement is vital because BDs tend to contract with age, while also decreasing in size as mass increases (Baraffe et al., 2003; Saumon & Marley, 2008; Burrows et al., 2001; Phillips et al., 2020). Thus there exists a degeneracy between mass, radius, and age for BDs making it difficult to test the substellar models with observed systems unless all three variables can be measured. These transiting systems provide

direct, independent measurements on two of these degenerate parameters, and in cases where the host star's age can be precisely determined, all three (e.g. Gillen et al., 2017; Nowak et al., 2017; David et al., 2019; Vowell et al., 2023).

This rapidly growing population of transiting BDs also allows us to revisit the longstanding idea of the so-called "brown dwarf desert". Prior work has shown a dearth of brown dwarfs orbiting main sequence host stars with semi-major axes < 5 au. (Marcy et al., 1997; Latham et al., 1998). Ma & Ge (2014) refined our understanding of the brown dwarf desert by investigating the population of all published brown dwarfs discovered with the RV method at the time. Here they found that the "driest land" of the desert lies between $35 < m \sin i < 55\ M_J$ and with period $P < 100$ days). The authors attribute this feature to being a result of different formation mechanisms dominating in different mass regimes. Namely, that stellar binary formation is responsible for the systems with BD companions $> 42 M_J$ while formation in the protoplanetary disk explains the systems with BDs $< 42 M_J$. However, the sample in this study with period $P < 100$ days was quite small at only 25 brown dwarfs. Furthermore, by virtue of being a RV study, it was restricted to only probing $m \sin i$ rather than the BD mass directly, unable to break the $\sin i$ degeneracy in most cases, a complication that the transiting population does not have.

As this population of transiting brown dwarfs expanded in the era of space-based transit surveys, several new discoveries noted an "oasis" forming in the desert (Carmichael et al., 2020; Šubjak et al., 2020; Henderson et al., 2024b) with new transiting systems beginning to populate the driest region of the desert noted by Ma & Ge (2014). With the new discoveries presented in this work, the transiting BD population now exceeds 50 systems, more than double the size of the population Ma & Ge (2014) had access to, opening the door for a reevaluation of brown dwarf desert from a new perspective. Hence, in this paper we present the discovery of 11 new transiting companions from NASA's *TESS* mission. 6 of these systems are BDs, with 3 lying within the Ma & Ge (2014) defined "driest" region of the BD desert. We confirmed the remaining 6 non-BD companions as very low-mass stars $< 150\ M_J$. In §4.3 of this manuscript, we present all the observations collected for each system in this work. §4.4 details our analysis of each system using `EXOFASTv2` (Eastman

et al., 2013, 2019). In §4.5 we provide a discussion on how these new systems fit into the population as a whole with a renewed perspective on the BD desert. We also discuss a detection of lithium in the host star of the BD companions presented here (TOI-5882). Finally, we present our conclusions in §4.6.

4.3 Observations

In the following subsections we present all observations collected and analyzed for each target in this sample. To briefly summarize, each target has a suite of observations that serve to characterize the host star and/or companion and rule out false-positive scenarios. Generally, these observations include archival multiband observations from various ground-based missions, time-series photometry from both space and ground-based telescopes, spectroscopy, and high resolution imaging. See Table 4.1 for the relevant results of the archival data associated with each system.

Table 4.1. Literature and Measured Properties

		TOI-2844	TOI-3122	TOI-3577	TOI-3755	Source
Other identifiers:						
	TESS Input Catalog	TIC 387342052	TIC 61117473	TIC 396133015	TIC 281196902	
	TYCHO-2	TYC 771-367-1	TYC 6773-1-1	TYC 3608-647-1	—	
	2MASS	J07204878+1301073	J15074899-2809237	J21482300+4820042	J04385936+6640161	
	Gaia DR3	3166196736096450816	6212565847439064192	1977894600881987328	483359575160953728	
Astrometric Parameters:						
α_{J2000}‡	Right Ascension (h:m:s)	07:20:48.78	15:07:48.99	21:48:23.01	04:38:59.37	1
δ_{J2000}‡	Declination (d:m:s)	13:01:07.4	-28:09:23.8	48:20:04.4	66:40:16.2	1
μ_α	Gaia DR3 proper motion in RA (mas yr^{-1})	-2.992 ± 0.016	-13.329 ± 0.015	5.052 ± 0.011	-11.614 ± 0.007	1
μ_δ	Gaia DR3 proper motion in Dec (mas yr^{-1})	-4.906 ± 0.016	-0.501 ± 0.013	-33.472 ± 0.011	11.407 ± 0.009	1
π	Gaia DR3 Parallax (mas)	1.4262 ± 0.0137	1.9337 ± 0.0147	2.3184 ± 0.011	3.0749 ± 0.0104	1
$v \sin i_\star$	Projected rotational velocity (km s^{-1})	60.8 ± 2.6	23.2 ± 5.1	10.3 ± 0.5	5.1 ± 0.5	2
Photometric Parameters:						
G	Gaia G mag.	11.87 ± 0.02	12.52 ± 0.02	11.75 ± 0.02	12.62 ± 0.02	1
$G_{\rm BP}$	Gaia $G_{\rm BP}$ mag.	12.08 ± 0.02	12.835 ± 0.02	12.07 ± 0.02	13.06 ± 0.02	1
$G_{\rm RP}$	Gaia $G_{\rm RP}$ mag.	11.52 ± 0.02	12.05 ± 0.02	11.26 ± 0.02	12.01 ± 0.02	1
T	TESS mag.	11.583 ± 0.007	12.123 ± 0.008	11.321 ± 0.006	12.079 ± 0.006	3
J	2MASS J mag.	11.168 ± 0.022	11.515 ± 0.026	10.638 ± 0.023	11.316 ± 0.024	4
H	2MASS H mag.	10.967 ± 0.027	11.277 ± 0.025	10.381 ± 0.03	10.966 ± 0.028	4
K	2MASS K mag.	10.927 ± 0.021	11.207 ± 0.024	10.318 ± 0.020	10.876 ± 0.022	4
$W1$	WISE $W1$ mag.	10.90 ± 0.03	11.05 ± 0.03	10.24 ± 0.03	10.82 ± 0.03	5
$W2$	WISE $W2$ mag.	10.93 ± 0.03	11.07 ± 0.03	10.27 ± 0.03	10.87 ± 0.03	5
$W3$	WISE $W3$ mag.	10.987 ± 0.143	11.147 ± 0.155	10.298 ± 0.046	10.651 ± 0.093	5

Table 4.1. *(Continued)*

		TOI-4462	TOI-4635	TOI-4737	TOI-4759	Source
Other identifiers:						
	TESS Input Catalog	TIC 76420654	TIC 337129672	TIC 142532090	TIC 49705089	
	TYCHO-2	TYC 2635-1030-1	—	—	—	
	2MASS	J18184078+3615175	J02143112+0804481	J06533851-1326106	J06234422-2401288	
	Gaia DR3	4605954852723545088	2521579495665163008	2949605211853441664	2936390357694302336	
Astrometric Parameters:						
α_{J2000}‡	Right Ascension (h:m:s)	18:18:40.78	02:14:31.26	06:53:38.51	06:23:44.23	1
δ_{J2000}‡	Declination (d:m:s)	36:15:17.5	08:04:45.3	-13:26:10.7	-24:01:28.9	1
μ_α	Gaia DR3 proper motion in RA (mas yr^{-1})	6.959 ± 0.038	122.150 ± 0.026	11.332 ± 0.013	0.634 ± 0.009	1
μ_δ	Gaia DR3 proper motion in Dec (mas yr^{-1})	−3.105 ± 0.045	−203.829 ± 0.019	−20.658 ± 0.014	7.847 ± 0.012	1
π	Gaia DR3 Parallax (mas)	2.5184 ± 0.0365	13.3018 ± 0.0238	1.7169 ± 0.0132	1.3243 ± 0.0107	1
$v \sin i_\star$	Projected rotational velocity (km s^{-1})	18.6 ± 0.4	3.5 ± 1.1	5.1 ± 0.6	13.4 ± 0.6	2
Photometric Parameters:						
G	Gaia G mag.	10.88 ± 0.02	11.32 ± 0.02	12.43 ± 0.02	12.73 ± 0.02	1
$G_{\rm BP}$	Gaia $G_{\rm BP}$ mag.	11.17 ± 0.02	11.99 ± 0.02	12.78 ± 0.02	13.10 ± 0.02	1
$G_{\rm RP}$	Gaia $G_{\rm RP}$ mag.	10.39 ± 0.02	10.53 ± 0.02	11.93 ± 0.02	12.20 ± 0.02	1
T	TESS mag.	10.445 ± 0.006	10.445 ± 0.006	11.992 ± 0.006	12.263 ± 0.007	3
J	2MASS J mag.	9.882 ± 0.020	9.565 ± 0.025	11.355 ± 0.024	11.596 ± 0.022	4
H	2MASS H mag.	9.585 ± 0.020	8.987 ± 0.028	11.057 ± 0.025	11.325 ± 0.025	4
K	2MASS K mag.	9.513 ± 0.020	8.854 ± 0.025	10.988 ± 0.025	11.21 ± 0.026	4
$W1$	WISE $W1$ mag.	9.46 ± 0.03	8.70 ± 0.03	10.93 ± 0.03	11.12 ± 0.03	5
$W2$	WISE $W2$ mag.	9.49 ± 0.03	8.74 ± 0.03	10.97 ± 0.03	11.15 ± 0.03	5
$W3$	WISE $W3$ mag.	9.410 ± 0.033	8.696 ± 0.030	10.960 ± 0.107	11.166 ± 0.107	5

Table 4.1. *(Continued)*

		TOI-5240	TOI-5467	TOI-5882	Source
Other identifiers:					
	TESS Input Catalog	TIC 40055053	TIC 83275782	TIC 232941965	
	TYCHO-2	TYC 2663-268-1	—	TYC 2695-1754-1	
	2MASS	J19322010+3456254	J06173449+2826431	J20473329+3444151	
	Gaia DR3	2046792606517797632	3433414139371114368	1869489729418662528	
Astrometric Parameters:					
α_{J2000}‡	Right Ascension (h:m:s)	19:32:20.11	06:17:34.49	20:47:33.29	1
δ_{J2000}‡	Declination (d:m:s)	34:56:25.4	28:26:43.1	34:44:15.2	1
μ_α	Gaia DR3 proper motion in RA (mas yr^{-1})	-0.414 ± 0.011	0.599 ± 0.016	-14.084 ± 0.014	1
μ_δ	Gaia DR3 proper motion in Dec (mas yr^{-1})	0.502 ± 0.012	-13.726 ± 0.012	-17.246 ± 0.017	1
π	Gaia DR3 Parallax (mas)	0.9894 ± 0.0114	1.7558 ± 0.0138	2.3859 ± 0.0144	1
$v \sin i_\star$	Projected rotational velocity (km s^{-1})	32.8 ± 1.3	31.2 ± 0.4	7.3 ± 0.5	2
Photometric Parameters:					
G	Gaia G mag.	11.92 ± 0.02	12.25 ± 0.02	11.11 ± 0.02	1
$G_{\rm BP}$	Gaia $G_{\rm BP}$ mag.	12.09 ± 0.02	12.56 ± 0.02	11.47 ± 0.02	1
$G_{\rm RP}$	Gaia $G_{\rm RP}$ mag.	11.63 ± 0.02	11.78 ± 0.02	10.58 ± 0.02	1
T	TESS mag.	11.692 ± 0.009	11.842 ± 0.006	10.634 ± 0.006	3
J	2MASS J mag.	11.307 ± 0.021	11.255 ± 0.021	9.988 ± 0.020	4
H	2MASS H mag.	11.176 ± 0.022	11.011 ± 0.023	9.736 ± 0.020	4
K	2MASS K mag.	11.154 ± 0.020	10.947 ± 0.020	9.615 ± 0.020	4
$W1$	WISE $W1$ mag.	11.14 ± 0.03	10.90 ± 0.03	9.57 ± 0.03	5
$W2$	WISE $W2$ mag.	11.16 ± 0.03	10.91 ± 0.03	9.60 ± 0.03	5
$W3$	WISE $W3$ mag.	10.928 ± 0.096	10.952 ± 0.144	9.662 ± 0.055	5

Notes — The uncertainties of the photometric measurements have a systematic floor applied that is usually larger than the reported catalog errors. ‡ Right Ascension and Declination are in epoch J2000. The coordinates come from Vizier where the Gaia RA and Dec have been precessed and corrected to J2000 from epoch J2016.
Sources: (1) Gaia Collaboration et al. (2023); (2) §4.3.3; (3) Stassun et al. (2019); (4) Cutri et al. (2003); Skrutskie et al. (2006); (5) Wright et al. (2010); Cutri et al. (2012)

4.3.1 *TESS* Photometry

Each system presented here initially showed signs of an orbiting companion via transits detected by *TESS*. *TESS* has a mosaic of four CCD cameras each with a 24°x24° field of view, and a pixel size of 21". In combination, this makes the *TESS* field of view 24°x96° for each sector, which is observed for approximately 27 days before moving to a new sector of sky. *TESS* observes at a 2-second, and in the *TESS* prime mission, the data were processed into 2-minute stacks for select stars, with the rest of the field being processed at 30-minute cadence. This prime mission observed >80% of the entire sky with the largest gaps in coverage occurring near the ecliptic plane. As *TESS* transitioned to its first, and now second, extended missions it continues to observe even more of the ecliptic plane. In this second extended mission, most preselected targets are now processed at 120-seconds while a smaller number are processed at 20-second cadence. Full-frame images are processed at 200-seconds.

The systems presented here were observed by *TESS* between Sectors 6 – 76 with cadences ranging from 30-minutes in the prime mission to as low as 2-minutes in the extended mission. The *TESS* data were originally downloaded and reduced using both the *TESS* Science Processing Operations Center (SPOC) Pipeline (Jenkins et al., 2016) and the MIT Quick-Look Pipeline (QLP; Huang et al., 2020a,b; Kunimoto et al., 2021). The initial detection of a transit-like signal was discovered and vetted by the faint-star QLP search (Kunimoto et al., 2022) for 10 out the 12 systems presented in this paper. The remaining two, TOI-4462 and TOI-4635, were initially detected by the QLP and SPOC pipelines respectively, and then vetted by the *TESS* Science Office. The diagnostic tests described in Twicken et al. (2018) were used to evaluate whether the transit-like signal is indeed Keplerian. Upon passing, each system was designated as a *TESS* Object of Interest (TOI; Guerrero et al., 2021). While both the QLP and SPOC pipelines correct for contamination by known nearby stars, we choose to use the SPOC light curves with the shortest cadence in our analysis wherever possible for consistency. See Table 4.2 for full details on the sectors, cadence, and pipeline used for each source. It should be noted that all QLP light curves are processed from the full frame images. The TESS-SPOC (Caldwell et al., 2020) light curves are produced by the SPOC on a best-effort

basis under the leadership of Doug Caldwell, the PI, and delivered as high-level science products to the Mikulski Archive for Space Telescopes (MAST) rather than as part of the official mission data products produced by the SPOC.

We downloaded the individual light curves from the MAST using the *lightkurve*[1] package (Lightkurve Collaboration et al., 2018). We then removed any long-term variability (both stellar and instumental) by fitting a spline to the flux and dividing the light curve by the best fitting spline model. We used the *Keplerspline*[2] package for this process as described in (Vanderburg & Johnson, 2014). We remove most of the out-of-transit data, electing to keep just one transit duration of baseline on either side of the transit.

4.3.2 Ground-Based Time-Series Photometry

In order to confirm that the signal observed by *TESS* is on-target not originating from a nearby eclipsing binary that is blended with the target star, we gathered ground-based, time-series photometry of each system as the companion transited its host star. Since *TESS* has a relatively large pixel scale (21″ per pixel), the shallow eclipses we measured, which are consistent with roughly 1 R_J, can be easily mimicked when a different, nearby eclipsing binary happens to fall on the same photometric aperture as the target star. The much deeper eclipses of the nearby eclipsing binary become diluted by the target star to mimic a much shallower event. Seeing-limited ground-based telescopes can have a much higher angular resolution than *TESS* typically 1-2″ and therefore can confirm that the signal is on-target, thereby ruling out nearby eclipsing binaries at all but the closest separations. It also has the benefit of observing in multiple wavelengths to confirm that the transit-like signal is achromatic. This is helpful because the eclipse depth of an eclipsing binary is nearly always wavelength dependent since the occulting body cannot be treated as a non-luminous sphere. We also note here, that while 6 of the companions presented here are low-mass M-dwarfs, and hence are eclipsing binaries themselves, they are so low in mass that we can still treat them as black spheres since they contribute negligibly to the overall flux of the system (Stevens et al., 2018). This process not only rules out the nearby eclipsing binary false positive, but also serves to

[1] `https://github.com/lightkurve/lightkurve`
[2] `https://github.com/avanderburg/keplerspline`

Table 4.2. Summary of Observations from TESS

Target	TESS Sector	Cadence (s)	Pipeline
TOI-2844	7	1800	TESS-SPOC
—	33	600	TESS-SPOC
—	44	600	TESS-SPOC
—	45	600	TESS-SPOC
—	46	600	TESS-SPOC
—	71	120	SPOC
—	72	120	SPOC
TOI-3122	11	1800	QLP
—	38	600	QLP
—	65	120	SPOC
TOI-3577	8	1800	QLP
—	56	120	SPOC
—	76	120	SPOC
TOI-3755	19	1800	TESS-SPOC
—	59	120	SPOC
—	73	120	SPOC
TOI-4462	26	1800	TESS-SPOC
—	40	600	TESS-SPOC
—	53	600	TESS-SPOC
—	54	600	TESS-SPOC
—	74	120	SPOC
TOI-4635	42	120	SPOC
—	43	120	SPOC
—	70	120	SPOC
—	71	120	SPOC
TOI-4737	6	1800	TESS-SPOC
—	7	1800	QLP
—	33	600	TESS-SPOC
TOI-4759	6	1800	QLP
—	33	600	QLP
TOI-5240	14	1800	QLP
—	40	600	QLP
—	41	600	TESS-SPOC
—	54	600	QLP
—	55	600	QLP
—	74	120	SPOC
—	75	120	SPOC
TOI-5467	43	600	TESS-SPOC
—	44	600	TESS-SPOC
—	45	600	TESS-SPOC
—	71	120	TESS-SPOC
—	72	120	TESS-SPOC
TOI-5882	15	1800	TESS-SPOC
—	41	600	TESS-SPOC
—	55	600	TESS-SPOC
—	75	120	SPOC

refine the ephemerides of systems in which these data are able to extend the photometric baseline.

The observations for these systems were collected through the *TESS* Follow-up Observing Program (TFOP; Collins et al., 2018) from various observatories as shown in Table 4.3. The Las Cumbres Observatory Global Telescope (LCOGT; Brown et al. 2013) was responsible for 14 light curves from the following sites: McDonald Observatory (McD), Teide Observatory (TEID), South African Astronomical Observatory (SAAO), and Cerro Tololo Inter-American Observatory (CTIO). The remaining light curves were contributed by the following facilities: Calar Alto Observatory, Brierfield Observatory, the Telescopio Carlos Sánchez (TCS) at Teide Observatory, Grand-Pra (GdP) Observatory, Thacher Observatory (Swift et al., 2022), KeplerCam at the Fred Lawrence Whipple Observatory (FLWO), and the Acton Sky Portal.

All data sets, except for the observations of TOI-3577 from MuSCAT2, were reduced and their light curves extracted using `AstroImageJ` (AIJ; Collins et al., 2017). To do this, we use AIJ's multi-aperture photometry tool using at least five similarly bright comparison stars. We use AIJ's built-in transit fitting tool to assess the quality of the data and determine detrending parameters. Generally, we only detrend against the parameters that strongly correlate with the apparent brightness of the companion stars as they change over the course of the night. We choose to adopt detrending only when the Bayesian Information Criterion of AIJ's transit-only fit significantly favors the detrended model. The detrending parameters used for each light curve can be found in Table 4.3. See §D in the appendix of Collins et al. (2017) for a detailed description of each detrending parameter. Finally, we normalized the data to the out-of-transit baseline and incorporated each light curve (with detrending) into our global fitting process (see §4.4).

Our follow-up observations of TOI-3577 were taken by MuSCAT2 on the TCS from Teide Observatory in Tenerife, Spain (Narita et al., 2019). MuSCAT2 is a multi-band imager with four cameras, each with a field of view of $7.4' \times 7.4'$. This set-up allows for simultaneous observation in multiple bands, which in our case, were the g', r', i', and z_s bands. These data were reduced by the dedicated MuSCAT2 pipeline (Parviainen et al., 2019), and incorporated into our global fit.

Table 4.3 Follow-up observations

TIC ID	TOI	Telescope	Camera	Date (UT)	Telescope Size (m)	Filter	Pixel Scale (arcsec)	Exposure Time (s)	Detrend params
387342052	2844	LCO-McD	QHY600	2023/4/5	0.35	i’	0.7	135	Airmass
		Zeiss Calar Alto	iKon-XL 230	2023/11/21	1.23	R	0.314	90	None
		LCO-TEID	Sinistro	2023/11/29	1.0	i’	0.389	19	None
61117473	3122	Brierfield	Moravian 16803	2023/5/15	0.36	R	0.735	180	Airmass
396133015	3577	TCS	MuSCAT2	2023/7/16	1.52	g’	0.44	10	None
		TCS	MuSCAT2	2023/7/16	1.52	r’	0.44	5	None
		TCS	MuSCAT2	2023/7/16	1.52	i’	0.44	5	None
		TCS	MuSCAT2	2023/7/16	1.52	z_s	0.44	10	None
281196902	3755	GdP	FLI4710	2022/3/3	0.4	i’	0.73	90	None
		Thacher CDK-700	Teledyne PIXIS	2023/3/18	0.7	r’	0.608	40	None
76420654	4462	FLWO	KeplerCam	2024/3/19	1.2	i’	0.672	6	Airmass
		LCO-TEID	Sinistro	2024/4/3	1.0	i’	0.389	38	tot_C_cnts
337129672	4635	LCO-SAAO	Sinistro	2023/11/22	1.0	z’	0.389	37	None
		LCO-CTIO-fa04	Sinistro	2023/12/5	1.0	z’	0.389	37	None
		LCO-CTIO-fa15	Sinistro	2023/12/5	1.0	z’	0.389	37	Airmass
142532090	4737	LCO-TEID	Sinistro	2023/11/26	1.0	i’	0.389	33	None
		LCO-CTIO	Sinistro	2023/12/6	1.0	i’	0.389	33	None
		LCO-SAAO	Sinistro	2023/12/24	1.0	i’	0.389	33	Airmass
49705089	4759	LCO-SAAO-fa06	Sinistro	2024/2/5	1.0	i’	0.389	44	Airmass
		LCO-SAAO-fa14	Sinistro	2024/2/5	1.0	i’	0.389	44	None
40055053	5240	LCO-TEID	Sinistro	2023/8/2	1.0	i’	0.389	26	None
83275782	5467	FLWO	KeplerCam	2023/3/4	1.2	i’	0.672	15	Airmass
		Acton Sky Portal	SBIG A4710	2023/3/20	0.36	r’	1.0	20	Airmass
		LCO-McD	Sinistro	2023/10/13	1.0	i’	0.389	29	tot_C_cnts
232941965	5882	LCO-McD	Sinistro	2023/6/16	1.0	z’	0.389	45	None

4.3.3 Spectroscopy

We collected spectroscopic observations for each system to measure the mass and eccentricity of their companions while also further ruling out the false-positive scenario of nearby eclipsing binaries. While several of the systems presented here have companions above the hydrogen-burning boundary, and thus are eclipsing binaries themselves, none of them have companions that are bright enough to be detected photometrically or spectroscopically. Hence, they are all single-lined spectroscopic binaries. Any potential nearby eclipsing binaries (both bound and unbound) that cannot be ruled out by ground-based photometry can be ruled out by spectroscopy within the angular diameter of the fiber. These are ruled out by the fact that the companions presented here are significantly more massive than their giant planet counterparts. The Doppler motion of the host stars' spectral lines is too large to be mimicked by a nearby eclipsing binary without resolving a secondary set of spectral features.

We obtained spectroscopic measurements for each system in this sample via the Tillinghast Reflector Échelle Spectrograph (TRES) on the 1.5-meter Tillinghast Reflector telescope at the Fred Lawrence Whipple Observatory on Mt. Hopkins, Arizona. The TRES instrument is a fiber-fed, échelle spectrograph with a resolving power of 44,000. We reduced the spectra according to Buchhave et al. (2010) and analyzed each observation with the Stellar Parameter Classification (SPC) tool (Buchhave et al., 2012) in order to measure the metallicity, effective temperature, surface gravity, and projected rotational velocity of the star. We incorporated the average metallicity for each system into our analysis as a Gaussian prior in our global fits (see §4.4). We did not incorporate the effective temperature or surface gravity measurements from SPC as priors because these quantities are better constrained by the fit itself. This is due to the fact that `EXOFASTv2` simultaneously models the spectral energy distribution, companion's transit, and stellar evolutionary models (Eastman et al., 2023)

Finally, we derived the radial velocities according to the methods described in Quinn et al. (2012), except that we do not cross-correlate against a template spectrum. Instead, we create a high S/N, median-combined observed spectrum that we cross-correlate with each individual spectrum.

See Table 4.4 for a sample radial velocity point for each system (the full table of radial velocities is available in machine-readable form in the online journal).

4.3.3.1 SOPHIE Spectroscopy

We complement the TRES data with SOPHIE observations of TOI-5882. SOPHIE is a stabilized échelle spectrograph dedicated to high-precision radial-velocity measurements at the 1.93-m telescope of the Observatoire de Haute-Provence, France (Perruchot et al., 2008; Bouchy et al., 2009, 2013). We used its high-resolution mode (resolving power $R = 75\,000$) and the fast readout of its CCD.

Removing a few observations with low accuracy, we have a dataset of 21 SOPHIE measurements of TOI-5882 secured from December 2022 to July 2024. Exposure times ranged between 5 and 37 minutes, allowing signal to-noise ratios between 14 and 40 to be reached per pixel at 550 nm.

The radial velocities were extracted with the SOPHIE pipeline, as presented by Bouchy et al. (2009) and refined by Heidari et al. (2024, 2025). That procedure includes corrections for bad pixels, cosmic rays, and charge transfer inefficiency of the CCD, as well as sky background and instrumental drifts. It derives cross correlation functions (CCF) from a numerical mask, then fit the CCFs by Gaussians to derive the radial velocities (Baranne et al., 1996; Pepe et al., 2002). One sample measurement is reported in Table 4.4.

4.3.4 High Resolution Imaging

While ground-based transits rule out nearby eclipsing binaries at most scales, if another source is close enough to the target star, it may be blended both in *TESS* and from the ground. Therefore, to verify that there is no contamination at these very small separations, and in order to detect any potentially bright companions, we utilized high-resolution imaging. We employed both Adaptive Optics (AO) and speckle imaging instruments to obtain our high resolution images for these systems.

We used the ShARCS and PHARO instruments for AO imaging. The ShARCS instrument is on the Shane 3.0-meter telescope located at Lick Observatory (Kupke et al., 2012; Gavel et al., 2014; McGurk et al., 2014). The PHARO instrument is on the Palomar Hale 5-meter telescope at Palomar Observatory (Hayward et al., 2001). For our speckle observations we used the following telescopes

Table 4.4. One Representative RV measurement for each system.

Target	BJD_{TDB}	RV (m s^{-1})	σ_{RV} (m s^{-1})	Spectrograph
TOI-2844	2459528.8676	-6696	1791	TRES
TOI-3122	2459651.9406	14841	145	TRES
TOI-3577	2459395.9184	52	70	TRES
TOI-3755	2459477.9662	-8617	31	TRES
TOI-4462	2459468.6623	944	76	TRES
TOI-4635	2459556.7367	6170	19	TRES
TOI-4737	2459583.9325	2529	65	TRES
TOI-4759	2459623.7415	-64	53	TRES
TOI-5240	2459681.9612	20204	375	TRES
TOI-5467	2459697.6358	-237	352	TRES
TOI-5882	2459899.6240	108	55	TRES
TOI-5882	2459930.2705	-22361.2	12.4	SOPHIE

Notes — The full table of RVs for each system is available in machine-readable form in the online journal.

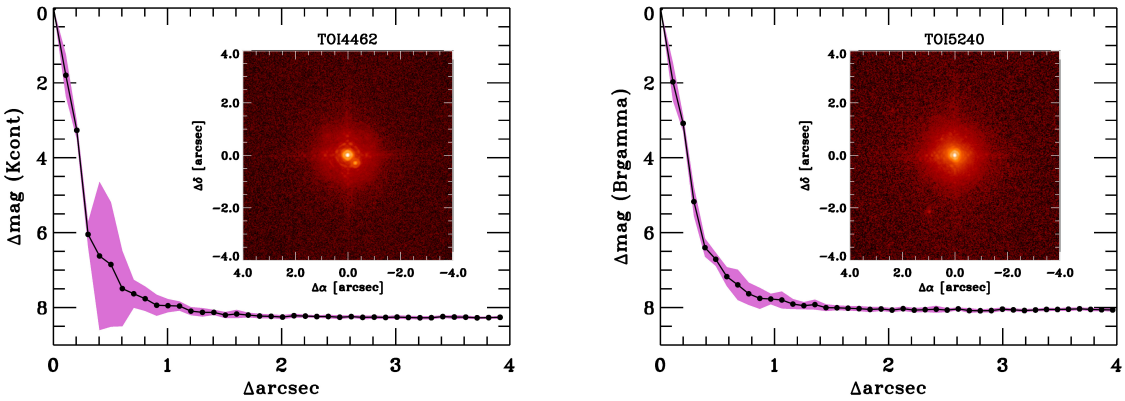

Figure 4.1 The adaptive optics image and contrast curves for TOI-4462 and TOI-5240 taken by PHARO on the 5.0 m Palomar telescope. (Left) TOI-4462 in the K_{cont} filter with a bright companion clearly seen at a separation of 0.4″. (Right) TOI-5240 in the Brγ filter with a faint companion at a separation of 2.4″.

and instruments: HRCam on the Southern Astrophysical Research (SOAR) 4.1-meter telescope at CTIO (Tokovinin, 2018; Ziegler et al., 2020), the NN-EXPLORE Exoplanet Stellar Speckle Imager (NESSI; Scott et al., 2018) on the WIYN 3.5-meter telescope at Kitt Peak Observatory, the Speckle Polarimeter on the 2.5-meter telescope at the Caucasian Mountain Observatory of the Sternberg Astronomical Institute (SAI) at Lomonosov Moscow State University, and the Zorro instrument on the Gemini-South 8-meter telescope. The Speckle Polarimeter used an Andor iXon 897 Electron Multiplying CCD for the observation of TOI-3755 (Safonov et al., 2017). All other observations from this instrument used a Hamamatsu ORCA-quest CMOS detector (Strakhov et al., 2023). See Table 4.5 for a summary of each observation including the dates each system was observed, filters used, contrast achieved, and whether a nearby companion was detected.

Our high resolution imaging runs resulted in the detection of only two nearby companions, one in the TOI-4462 system and another in the TOI-5240 system (see Figure 4.1). The companion to TOI-5240 was detected only by PHARO and is 2.4″away at a position angle of 156 degrees. It is 6.67 magnitudes dimmer in the Brγ filter, contributing only 0.1% of the total flux of the unresolved system. Even if this companion is a perfectly edge-on, equal mass eclipsing binary, the eclipse depths would be an order of magnitude smaller than the observed transit depths. Since it contributes a negligible amount of light to the overall flux of the system, we chose to neglect this companion in our analysis (eg. Mugrauer & Michel, 2020, 2021).

The companion to TOI-4462 A was resolved by both SAI and PHARO at 0.4″separation and a position angle of 225 degrees. It is approximately 2.6 magnitudes dimmer in the H_{cont} and K_{cont} filters, too bright to neglect in our analysis (see §4.4). However, we remain confident that the Keplerian signals detected in both our photometry and spectroscopy can only be attributed to the brighter, primary star. The transits observed by *TESS* KeplerCam, and LCO-TEID show no evidence of chromaticity, and the spectral line profiles show no evidence of a secondary set of spectral lines that would produce an apparent RV shift. Since TRES observed TOI-4462 with a 2.3″fiber (larger than the companion's separation), the host star spectra were blended with light from the companion. However, this faint companion would only affect the measured RVs at the

10s of m/s level (Buchhave et al., 2011), significantly smaller than 10000 m/s semi-amplitude we measure for the TOI-4462 system. Hence we are confident that the signal we detect is due to an unresolved transiting companion around the brighter primary star TOI-4462 A.

Table 4.5. Summary of High-Resolution Imaging Observations

Target	Telescope	Instrument	Image Type	Filter	Contrast	Observation Date (UT)	Detection?†
TOI-2844	SOAR (4.1 m)	HRCam	Speckle	I_c	Δ 5.8 mag at 1″	2022 Apr 15	No
—	WIYN (3.5 m)	NESSI	Speckle	832 nm	—	2022 Apr 18	No
TOI-3122	SOAR (4.1 m)	HRCam	Speckle	I_c	Δ 5.0 mag at 1″	2022 Apr 25	No
TOI-3577	Palomar (5.0 m)	PHARO	AO	Brγ	Δ 5.8 mag at 0.5″	2023 Jun 7	No
TOI-3755	SAI (2.5 m)	Speckle Polarimeter	Speckle	I_c	Δ 5.7 mag at 1″	2021 Oct 29	No
TOI-4462	SAI (2.5 m)	Speckle Polarimeter	Speckle	I_c	Δ 6.3 mag at 1″	2023 Jan 22	Yes
—	SAI (2.5 m)	Speckle Polarimeter	Speckle	I_c	Δ 5.3 mag at 1″	2024 Feb 24	Yes
—	Palomar (5.0 m)	PHARO	AO	H_{cont}	Δ 7.2 mag at 0.5″	2024 Apr 21	Yes
—	Palomar (5.0 m)	PHARO	AO	K_{cont}	Δ 6.9 mag at 0.5″	2024 Apr 21	Yes
TOI-4635	Shane (3.0 m)	ShARCS	AO	J	—	2021 Nov 21	No
—	Shane (3.0 m)	ShARCS	AO	Ks	—	2021 Nov 21	No
—	SOAR (4.1 m)	HRCam	Speckle	I_c	Δ 6.7 mag at 1″	2024 Jan 8	No
TOI-4737	Gemini (8.0 m)	Zorro	Speckle	562 nm	Δ 4.3 mag at 0.5″	2022 Mar 19	No
—	Gemini (8.0 m)	Zorro	Speckle	832 nm	Δ 6.0 mag at 0.5″	2022 Mar 19	No
—	SOAR (4.1 m)	HRCam	Speckle	I_c	Δ 5.6 mag at 1″	2022 Apr 15	No
TOI-4759	SOAR (4.1 m)	HRCam	Speckle	I_c	Δ 6.2 mag at 1″	2022 Apr 15	No
TOI-5240	Palomar (5.0 m)	PHARO	AO	Brγ	Δ 6.7 mag at 0.5″	2023 Jun 6	Yes
—	SAI (2.5 m)	Speckle Polarimeter	Speckle	I_c	Δ 6.3 mag at 1″	2023 Sep 1	No
TOI-5467	SAI (2.5 m)	Speckle Polarimeter	Speckle	I_c	Δ 6.2 mag at 1″	2022 Dec 12	No
TOI-5882	Palomar (5.0 m)	PHARO	AO	Brγ	Δ 6.8 mag at 0.5″	2023 Jun 6	No
—	SAI (2.5 m)	Speckle Polarimeter	Speckle	I_c	Δ 7.4 mag at 1″	2023 Aug 28	No

Notes — All images and contrast curves are available on ExoFOP.
† Detection refers to a positive detection of a star within the field of view of the AO or speckle instrument, subject to the maximum contrast possible with the instrument in question.

4.4 Analysis

We analyzed each system using `EXOFASTv2` [3] (Eastman et al., 2019), a publicly available exoplanet fitting suite. `EXOFASTv2` is a Differential Evolution Markov Chain Monte Carlo (MCMC) code which globally fits both the star and the companion simultaneously, ensuring a self-consistent set of parameters for the entire system. In each fit, we generate a Spectral Energy Distribution (SED) model for the host star using MESA Isochrones and Stellar Tracks (MIST; Paxton et al., 2011, 2013) in order to fit the host star, while the companion is fit with a standard Keplerian model. Our SED model is fit to broadband archival photometry which we collected from Gaia Data Release 3 (DR3; Gaia Collaboration et al., 2023), 2MASS (Cutri et al., 2003; Skrutskie et al., 2006), and WISE (Wright et al., 2010; Cutri et al., 2012). The Keplerian model for the companion is fit to the *TESS* and ground based transits as well as the RV data from TRES and SOPHIE. For a more detailed explanation of the modeling process, see Eastman et al. (2019).

The fit was generally set up in the same way for each system, except for TOI-4462, which required special consideration due to the presence of a bright nearby companion which we discuss in §4.4.1. For the other 11 systems, we first compiled the archival photometry for each target in the Gaia G, Bp, Rp, 2MASS J, H, Ks, and WISE $W1$, $W2$, and $W3$ bands to construct the SED. We then placed a set of priors on each system based on previous observations, the first of which was a Gaussian prior on the parallax from Gaia DR3 with the Lindegren et al. (2021) correction applied. The parallax uncertainty was added in quadrature with 0.01 to account for any remaining systematic residuals. We also placed a Gaussian prior on the host star metallicity centered on the average value of the TRES-derived metallicity with a prior width of twice the standard deviation. Additionally, we place an upper limit on the V-band extinction along the line-of-site using the dust maps from Schlegel et al. (1998) and Schlafly & Finkbeiner (2011).

In addition to the priors described above, we also fit for a dilution term in each system to account for unresolved contaminants.To do this, we placed a prior of 0% ± 10% of the contamination ratio reported by the *TESS* Input Catalog (TIC; Stassun et al., 2018, 2019). While the QLP and SPOC

[3] `https://github.com/jdeast/EXOFASTv2`

light curves are both already corrected for known contaminants, we still chose to fit for a dilution term as a conservative assumption that the correction applied had a precision of at most 10%. We did this because the contamination ratio reported by the TIC is only an estimate that does not account for the actual point spread functions, as the CCD location and camera were unknown until after the launch of *TESS*. We also provided each fit with starting points on several parameters from the TIC. Specifically, we adopted the TIC-derived values for the host star's mass, radius, and effective temperature as well as the companion's orbital period, time of conjunction, and radius. We retrieved these values from the *TESS* mission catalog on ExoFOP[4] (NExScI, 2022). We performed a preliminary fit with `EXOFASTv2` on each system which included fitting a linear term to the radial velocities in order to account for a long-term drift due to unseen outer companions. In every case except for TOI-4737, this resulted in a slope consistent with zero within 1-sigma, and we subsequently fixed the slope to zero in all subsequent fits for these systems. For TOI-4737, we continued to fit for this long-term trend, and in the final iteration of these fits which we publish here, we found a slope of -1.63 ± 0.23 m s^{-1} day^{-1}. Each system's final fit was run to the adopted convergence criteria suggested by Eastman et al. (2019) of at least 1000 independent draws and a Gelman-Rubin statistic < 1.01. See Table 4.6 for the priors used, and the median values determined from our analysis.

Four of our fits resulted in bimodal posterior distributions. This typically arises when `EXOFASTv2` is unable to distinguish between a host star that is at the end of the main sequence versus the subgiant branch, resulting in high and low stellar mass solutions. Indeed, this was the case in all four bimodal systems presented here (TOI-3577, TOI-4462, TOI-4759, and TOI-5882). We characterized each solution independently by splitting the posterior distributions at the local minimum between the two solutions. We present both solutions for the sake of transparency, but in each case we adopt the higher probability solution as the preferred parameter set. See Table 4.7 for the priors used, and the median values determined for both solutions of these bimodal systems. Plots of the transit photometry, radial velocities, SEDs, and MIST evolutionary tracks for each system presented in

[4] `https://exofop.ipac.caltech.edu/tess/`

this work are presented in Figures 4.6-4.16.

Table 4.6. Median Values and 68% Confidence Intervals for Fitted Stellar and Planetary Parameters

		TOI-2844	TOI-3122	TOI-3755	TOI-4635
Priors:					
π	Gaia Parallax (mas)	$\mathcal{G}$[1.4759, 0.01696]	$\mathcal{G}$[1.962, 0.01778]	$\mathcal{G}$[3.0924, 0.01443]	$\mathcal{G}$[13.33, 0.02582]
[Fe/H]	Metallicity (dex)	$\mathcal{G}$[0.025, 0.198]	$\mathcal{G}$[0.3193, 0.1188]	$\mathcal{G}$[0.3156, 0.1007]	$\mathcal{G}$[-0.1783, 0.1608]
A_V	V-band extinction (mag)	$\mathcal{U}$[0, 0.2725]	$\mathcal{U}$[0, 0.4675]	$\mathcal{U}$[0, 0.9867]	$\mathcal{U}$[0, 0.3959]
D_T	Dilution in *TESS*	$\mathcal{G}$[0, 0.008335]	$\mathcal{G}$[0, 0.027729]	$\mathcal{G}$[0, 0.012054]	$\mathcal{G}$[0, 0.002608]
Primary Star Parameters:					
M_*	Mass ($M_\odot$)	$1.585^{+0.071}_{-0.072}$	$1.247^{+0.074}_{-0.091}$	$1.037^{+0.066}_{-0.071}$	$0.698^{+0.027}_{-0.025}$
R_*	Radius ($R_\odot$)	$1.784^{+0.085}_{-0.08}$	$1.336^{+0.062}_{-0.045}$	$1.044^{+0.042}_{-0.038}$	0.683 ± 0.011
L_*	Luminosity ($L_\odot$)	$6.51^{+0.57}_{-0.48}$	$2.27^{+0.24}_{-0.27}$	$0.99^{+0.12}_{-0.11}$	$0.182^{+0.011}_{-0.013}$
ρ_*	Density (cgs)	$0.394^{+0.065}_{-0.059}$	$0.742^{+0.09}_{-0.12}$	$1.29^{+0.18}_{-0.17}$	3.09 ± 0.12
$\log g$	Surface gravity (cgs)	$4.135^{+0.048}_{-0.051}$	$4.284^{+0.038}_{-0.059}$	$4.417^{+0.043}_{-0.049}$	4.613 ± 0.013
$T_{\rm eff}$	Effective temperature (K)	6910.0 ± 210	6120.0^{+180}_{-220}	5630.0 ± 170	4555.0^{+67}_{-74}
[Fe/H]	Metallicity (dex)	$0.06^{+0.12}_{-0.089}$	0.29 ± 0.11	$0.334^{+0.092}_{-0.098}$	$-0.091^{+0.039}_{-0.033}$
$[{\rm Fe/H}]_0$	Initial metallicity	$0.22^{+0.1}_{-0.088}$	$0.298^{+0.094}_{-0.093}$	$0.317^{+0.085}_{-0.093}$	$-0.077^{+0.055}_{-0.051}$
Age	Age (Gyr)	$1.08^{+0.52}_{-0.42}$	$2.5^{+2.6}_{-1.6}$	$4.9^{+4.9}_{-3.5}$	$7.5^{+4.2}_{-4.5}$
EEP	Equal evolutionary phase	$342.5^{+9.5}_{-14}$	351.0^{+59}_{-32}	362.0^{+44}_{-40}	332.0^{+11}_{-24}
A_V	V-band extinction (mag)	$0.132^{+0.084}_{-0.082}$	$0.3^{+0.12}_{-0.17}$	$0.5^{+0.15}_{-0.16}$	$0.26^{+0.1}_{-0.15}$
d	Distance (pc)	$677.0^{+7.9}_{-7.6}$	510.0 ± 4.6	323.5 ± 1.5	$75.01^{+0.15}_{-0.14}$

Table 4.6 (cont'd)

		TOI-2844	TOI-3122	TOI-3755	TOI-4635
Companion Parameters:					
P	Period (days)	3.5524204 ± 0.000003	6.1836025 ± 0.0000063	$5.543744^{+0.0000062}_{-0.0000061}$	12.2769349 ± 0.0000033
R_P	Radius (R_J)	$0.775^{+0.047}_{-0.043}$	$1.235^{+0.075}_{-0.057}$	$0.885^{+0.051}_{-0.046}$	1.02 ± 0.019
M_P	Mass (M_J)	$54.0^{+4.9}_{-5.1}$	$101.5^{+4.1}_{-4.8}$	$47.1^{+2}_{-2.1}$	$84.0^{+2.1}_{-2}$
T_C	Time of conjunction ($\mathrm{BJD_{TDB}}$)	$2459574.31396^{+0.00094}_{-0.00099}$	$2459356.52122^{+0.00067}_{-0.00065}$	$2459914.24483^{+0.00057}_{-0.00058}$	$2459448.74844 \pm 0.00018$
T_0	Optimal conjunction time ($\mathrm{BJD_{TDB}}$)	$2459940.21326^{+0.00088}_{-0.00093}$	$2459727.53737^{+0.00054}_{-0.00052}$	$2459775.65123^{+0.00054}_{-0.00057}$	2460013.48744 ± 0.0001
a	Semi-major axis (AU)	$0.0537^{+0.00079}_{-0.00082}$	$0.0728^{+0.0014}_{-0.0018}$	$0.0629^{+0.0013}_{-0.0015}$	$0.0958^{+0.0012}_{-0.0011}$
i	Inclination (Degrees)	$83.7^{+2}_{-1.3}$	$87.3^{+1.6}_{-1.5}$	$87.51^{+0.35}_{-0.36}$	$88.791^{+0.057}_{-0.056}$
e	Eccentricity	$0.424^{+0.046}_{-0.041}$	$0.4704^{+0.008}_{-0.0077}$	$0.0049^{+0.0031}_{-0.0026}$	0.4906 ± 0.0015
ω_*	Argument of periastron (Degrees)	159.0 ± 11	$75.55^{+0.98}_{-0.91}$	21.0^{+44}_{-57}	$-5.99^{+0.78}_{-0.74}$
T_{eq}	Equilibrium temperature (K)	1919.0^{+37}_{-33}	1267.0^{+27}_{-32}	1106.0 ± 28	$586.6^{+8.2}_{-9.5}$
τ_{circ}	Tidal circularization timescale (Gyr)	27.0^{+17}_{-12}	$33.0^{+10}_{-9.7}$	500.0^{+170}_{-130}	827.0^{+71}_{-65}
K	RV semi-amplitude (m/s)	5700.0^{+450}_{-470}	10450.0 ± 110	5127.0 ± 22	10032.0^{+41}_{-43}
R_P/R_*	Radius of planet in stellar radii	0.0447 ± 0.0013	$0.0952^{+0.0026}_{-0.0025}$	0.0872 ± 0.0025	$0.15339^{+0.00081}_{-0.00082}$
a/R_*	Semi-major axis in stellar radii	6.47 ± 0.34	$11.74^{+0.45}_{-0.68}$	$12.96^{+0.57}_{-0.61}$	30.17 ± 0.38
Depth	*TESS* flux decrement at mid-transit	0.00212 ± 0.00011	$0.01026^{+0.00056}_{-0.00055}$	0.0085 ± 0.00046	$0.02871^{+0.00036}_{-0.00035}$
τ	Ingress/egress transit duration (days)	$0.0073^{+0.0016}_{-0.0015}$	$0.01015^{+0.0015}_{-0.00082}$	$0.0144^{+0.0017}_{-0.0014}$	0.02135 ± 0.00058
T_{14}	Total transit duration (days)	$0.1258^{+0.0019}_{-0.0018}$	$0.1075^{+0.0019}_{-0.0016}$	$0.1267^{+0.0021}_{-0.0019}$	$0.12316^{+0.00051}_{-0.0005}$
b	Transit impact parameter	$0.52^{+0.11}_{-0.19}$	$0.3^{+0.14}_{-0.17}$	$0.564^{+0.052}_{-0.058}$	$0.509^{+0.017}_{-0.019}$
ρ_P	Density (cgs)	143.0^{+31}_{-27}	67.0^{+10}_{-12}	84.0^{+16}_{-14}	$98.3^{+4.9}_{-4.6}$
$\log g_P$	Surface gravity	$5.346^{+0.065}_{-0.069}$	$5.218^{+0.044}_{-0.062}$	$5.173^{+0.052}_{-0.055}$	5.302 ± 0.014
Θ	Safronov number	$4.71^{+0.49}_{-0.48}$	$9.58^{+0.47}_{-0.54}$	$6.45^{+0.36}_{-0.35}$	$22.57^{+0.47}_{-0.46}$
T_S	Time of eclipse ($\mathrm{BJD_{TDB}}$)	$2459575.217^{+0.086}_{-0.084}$	$2459353.947^{+0.033}_{-0.034}$	$2459911.4849^{+0.0084}_{-0.0091}$	$2459446.27^{+0.011}_{-0.01}$
$T_{S,14}$	Total eclipse duration (days)	$0.142^{+0.035}_{-0.011}$	$0.205^{+0.069}_{-0.2}$	$0.1269^{+0.0021}_{-0.002}$	0.1137 ± 0.0013
$e \cos \omega_*$		$-0.391^{+0.042}_{-0.04}$	$0.1173^{+0.0076}_{-0.0078}$	$0.0034^{+0.0024}_{-0.0026}$	0.4878 ± 0.0016
$e \sin \omega_*$		$0.148^{+0.088}_{-0.078}$	$0.4555^{+0.0082}_{-0.0078}$	$0.001^{+0.0039}_{-0.0032}$	$-0.0511^{+0.0066}_{-0.0063}$
M_P/M_*	Mass ratio	$0.0326^{+0.0028}_{-0.003}$	$0.0778^{+0.0023}_{-0.0018}$	$0.04337^{+0.0011}_{-0.00093}$	0.1148 ± 0.0016
d/R_*	Separation at mid-transit	$4.62^{+0.56}_{-0.58}$	$6.26^{+0.28}_{-0.36}$	$12.95^{+0.58}_{-0.6}$	24.14 ± 0.41

Notes — The priors listed at the top of the table are labeled as $\mathcal{G}$[mean, standard deviation] if they are Gaussian priors and $\mathcal{U}$[lower limit, upper limit] if they are uniform priors.

Table 4.6. (cont'd)

		TOI-4737	TOI-5240	TOI-5467
Priors:				
π	Gaia Parallax (mas)	$\mathcal{G}$[1.7399, 0.01656]	$\mathcal{G}$[1.0355, 0.01516]	$\mathcal{G}$[1.7819, 0.01704]
[Fe/H]	Metallicity (dex)	$\mathcal{G}$[0.3267, 0.1499]	$\mathcal{G}$[-0.1571, 0.2089]	$\mathcal{G}$[0.3257, 0.1645]
A_V	V-band extinction (mag)	$\mathcal{U}$[0, 1.8386]	$\mathcal{U}$[0, 0.4879]	$\mathcal{U}$[0, 1.6687]
D_T	Dilution in *TESS*	$\mathcal{G}$[0, 0.005883]	$\mathcal{G}$[0, 0.024878]	$\mathcal{G}$[0, 0.007941]
Primary Star Parameters:				
M_*	Mass ($M_\odot$)	$1.336^{+0.08}_{-0.09}$	$1.754^{+0.094}_{-0.092}$	$1.515^{+0.059}_{-0.058}$
R_*	Radius ($R_\odot$)	$1.618^{+0.068}_{-0.066}$	2.35 ± 0.11	$1.503^{+0.046}_{-0.045}$
L_*	Luminosity ($L_\odot$)	$3.39^{+0.34}_{-0.31}$	$14.9^{+2.4}_{-2.1}$	$4.4^{+0.41}_{-0.33}$
ρ_*	Density (cgs)	$0.443^{+0.073}_{-0.065}$	$0.189^{+0.032}_{-0.026}$	$0.63^{+0.054}_{-0.052}$
$\log g$	Surface gravity (cgs)	$4.145^{+0.05}_{-0.053}$	$3.938^{+0.049}_{-0.047}$	$4.266^{+0.024}_{-0.027}$
$T_{\rm eff}$	Effective temperature (K)	6160.0^{+210}_{-200}	7390.0^{+350}_{-330}	6820.0^{+170}_{-150}
[Fe/H]	Metallicity (dex)	$0.24^{+0.1}_{-0.11}$	-0.12 ± 0.19	$0.265^{+0.098}_{-0.11}$
$[{\rm Fe/H}]_0$	Initial metallicity	$0.297^{+0.093}_{-0.096}$	$-0.03^{+0.18}_{-0.19}$	$0.316^{+0.083}_{-0.093}$
Age	Age (Gyr)	$3.0^{+1.6}_{-1.3}$	$1.19^{+0.23}_{-0.2}$	$0.29^{+0.42}_{-0.2}$
EEP	Equal evolutionary phase	377.0^{+38}_{-32}	374.0^{+13}_{-14}	294.0^{+27}_{-37}
A_V	V-band extinction (mag)	0.4 ± 0.11	$0.23^{+0.15}_{-0.14}$	$0.567^{+0.092}_{-0.08}$
d	Distance (pc)	$574.5^{+5.5}_{-5.4}$	966.0 ± 14	$560.5^{+5.4}_{-5.2}$

Table 4.6 (cont'd)

		TOI-4737	TOI-5240	TOI-5467
Companion Parameters:				
P	Period (days)	$9.320278^{+0.000018}_{-0.000017}$	4.1793241 ± 0.0000058	$2.6570963^{+0.0000027}_{-0.0000028}$
R_P	Radius (R_J)	$0.701^{+0.079}_{-0.059}$	$1.655^{+0.097}_{-0.096}$	$1.096^{+0.046}_{-0.043}$
M_P	Mass (M_J)	$66.3^{+2.7}_{-3.1}$	$128.0^{+4.9}_{-4.8}$	$91.7^{+2.8}_{-2.7}$
T_C	Time of conjunction (BJD_{TDB})	$2459222.4062^{+0.0017}_{-0.0018}$	$2459444.90408^{+0.0009}_{-0.00091}$	$2459545.35471^{+0.00052}_{-0.00053}$
T_0	Optimal conjunction time (BJD_{TDB})	2459949.3884 ± 0.0011	$2459950.60229 \pm 0.00057$	$2459927.97657 \pm 0.00035$
a	Semi-major axis (AU)	$0.097^{+0.0019}_{-0.0022}$	0.0626 ± 0.0011	$0.04394^{+0.00056}_{-0.00055}$
i	Inclination (Degrees)	$87.82^{+0.51}_{-0.46}$	$85.7^{+1.4}_{-1.1}$	$83.21^{+0.35}_{-0.37}$
e	Eccentricity	$0.0063^{+0.007}_{-0.0042}$	$0.0113^{+0.014}_{-0.0078}$	$0.0137^{+0.013}_{-0.0083}$
ω_*	Argument of periastron (Degrees)	-120.0^{+40}_{-89}	-115.0^{+28}_{-83}	121.0^{+57}_{-28}
T_{eq}	Equilibrium temperature (K)	1214.0^{+26}_{-25}	2187.0^{+80}_{-81}	1924.0^{+39}_{-34}
$\tau_{\rm circ}$	Tidal circularization timescale (Gyr)	$25000.0^{+15000}_{-11000}$	$25.7^{+9.5}_{-6.6}$	$18.1^{+3.8}_{-3.3}$
K	RV semi-amplitude (m/s)	5118.0 ± 49	10580.0^{+160}_{-150}	9760.0^{+130}_{-140}
R_P/R_*	Radius of planet in stellar radii	$0.0443^{+0.0047}_{-0.003}$	0.0723 ± 0.0019	0.075 ± 0.0017
a/R_*	Semi-major axis in stellar radii	$12.86^{+0.67}_{-0.66}$	$5.72^{+0.31}_{-0.27}$	$6.29^{+0.17}_{-0.18}$
Depth	*TESS* flux decrement at mid-transit	$0.00216^{+0.00048}_{-0.00028}$	0.00563 ± 0.0003	0.00569 ± 0.00025
τ	Ingress/egress transit duration (days)	$0.012^{+0.0019}_{-0.0015}$	$0.0192^{+0.0023}_{-0.0022}$	$0.015^{+0.0011}_{-0.001}$
T_{14}	Total transit duration (days)	$0.214^{+0.0029}_{-0.0027}$	$0.232^{+0.0023}_{-0.0022}$	0.1053 ± 0.0012
b	Transit impact parameter	$0.491^{+0.074}_{-0.095}$	$0.436^{+0.084}_{-0.13}$	$0.735^{+0.018}_{-0.02}$
ρ_P	Density (cgs)	236.0^{+76}_{-67}	$35.0^{+7.2}_{-5.7}$	$86.5^{+11}_{-9.8}$
$\log g_P$	Surface gravity	$5.521^{+0.083}_{-0.098}$	$5.063^{+0.056}_{-0.053}$	$5.278^{+0.034}_{-0.035}$
Θ	Safronov number	$13.7^{+1.3}_{-1.4}$	$5.52^{+0.34}_{-0.31}$	$4.85^{+0.22}_{-0.21}$
T_S	Time of eclipse (BJD_{TDB})	$2459227.054^{+0.016}_{-0.022}$	$2459446.983^{+0.012}_{-0.014}$	$2459546.6736^{+0.0091}_{-0.011}$
$T_{S,14}$	Total eclipse duration (days)	$0.213^{+0.0035}_{-0.0036}$	$0.2294^{+0.0042}_{-0.006}$	0.1054 ± 0.0011
$e\cos\omega_*$		$-0.002^{+0.0027}_{-0.0037}$	$-0.0039^{+0.0043}_{-0.0053}$	$-0.0057^{+0.0054}_{-0.0067}$
$e\sin\omega_*$		$-0.0026^{+0.0046}_{-0.0089}$	$-0.0065^{+0.0084}_{-0.017}$	$0.009^{+0.015}_{-0.0093}$
M_P/M_*	Mass ratio	$0.0474^{+0.0013}_{-0.0011}$	$0.0696^{+0.0018}_{-0.0017}$	0.0578 ± 0.0012
d/R_*	Separation at mid-transit	$12.92^{+0.68}_{-0.67}$	$5.77^{+0.32}_{-0.29}$	$6.22^{+0.2}_{-0.21}$

Table 4.7. Median Values and 68% Confidence Intervals for Fitted Stellar and Planetary Parameters for Bimodal Systems

		TOI-3577		**TOI-4462**	
		Low-mass solution (63.8% probability)	High-mass solution (36.2% probability)	Low-mass solution (90.7% probability)	High-mass solution (9.3% probability)
Priors:					
π	Gaia Parallax (mas)	$\mathcal{G}$[2.36440, 0.01487]		$\mathcal{G}$[2.53984, 0.03785]	
[Fe/H]	Metallicity (dex)	$\mathcal{G}$[-0.0486, 0.0889]		$\mathcal{G}$[0.0873, 0.1781]	
A_V	V-band extinction (mag)	$\mathcal{U}$[0, 2.2165]		$\mathcal{U}$[0, 0.0949]	
D_T	Dilution in *TESS*	$\mathcal{G}$[0, 0.032559]		$\mathcal{G}$[0, 0.057591]	
Primary Star Parameters:					
M_*	Mass ($M_\odot$)	$1.111^{+0.057}_{-0.067}$	$1.31^{+0.073}_{-0.056}$	$1.252^{+0.053}_{-0.061}$	$1.452^{+0.049}_{-0.047}$
R_*	Radius ($R_\odot$)	$1.753^{+0.068}_{-0.067}$	$1.733^{+0.069}_{-0.064}$	$2.084^{+0.084}_{-0.059}$	$2.128^{+0.046}_{-0.036}$
L_*	Luminosity ($L_\odot$)	$3.38^{+0.5}_{-0.42}$	$4.06^{+0.59}_{-0.52}$	$4.98^{+0.28}_{-0.24}$	$5.07^{+0.24}_{-0.22}$
ρ_*	Density (cgs)	$0.29^{+0.037}_{-0.034}$	$0.355^{+0.047}_{-0.038}$	$0.195^{+0.017}_{-0.023}$	$0.2132^{+0.0075}_{-0.011}$
$\log g$	Surface gravity (cgs)	$3.995^{+0.038}_{-0.04}$	$4.078^{+0.04}_{-0.034}$	$3.898^{+0.026}_{-0.04}$	$3.945^{+0.011}_{-0.015}$
$T_{\rm eff}$	Effective temperature (K)	5920.0 ± 210	6210.0^{+240}_{-200}	5970.0 ± 110	5930.0^{+84}_{-82}
[Fe/H]	Metallicity (dex)	$-0.031^{+0.071}_{-0.069}$	$-0.026^{+0.081}_{-0.073}$	$0.05^{+0.15}_{-0.13}$	$0.19^{+0.13}_{-0.14}$
$[Fe/H]_0$	Initial metallicity	$0.021^{+0.066}_{-0.064}$	$0.074^{+0.076}_{-0.068}$	0.09 ± 0.12	$0.22^{+0.11}_{-0.12}$
Age	Age (Gyr)	$6.8^{+1.8}_{-1.3}$	$3.29^{+0.68}_{-0.89}$	$4.73^{+0.75}_{-0.58}$	$2.88^{+0.36}_{-0.33}$
EEP	Equal evolutionary phase	$453.5^{+4.5}_{-7.7}$	398.0^{+15}_{-28}	$454.5^{+3.9}_{-5.4}$	$407.3^{+6.4}_{-7.4}$
A_V	V-band extinction (mag)	$0.31^{+0.16}_{-0.17}$	0.53 ± 0.15	$0.054^{+0.029}_{-0.035}$	$0.063^{+0.023}_{-0.036}$
d	Distance (pc)	423.2 ± 2.7	423.4 ± 2.7	$392.6^{+5.8}_{-5.6}$	$395.2^{+5.7}_{-5.5}$

Table 4.7 (cont'd)

		TOI-3577		TOI-4462	
		Low-mass solution (63.8% probability)	High-mass solution (36.2% probability)	Low-mass solution (90.7% probability)	High-mass solution (9.3% probability)
Companion Parameters:					
P	Period (days)	5.266759 ± 0.000013	$5.266759^{+0.000014}_{-0.000013}$	$4.9132987^{+0.0000088}_{-0.0000089}$	$4.9132998^{+0.0000088}_{-0.0000089}$
R_P	Radius (R_J)	$0.999^{+0.053}_{-0.051}$	$0.967^{+0.053}_{-0.048}$	$1.141^{+0.081}_{-0.078}$	1.158 ± 0.075
M_P	Mass (M_J)	$53.8^{+1.9}_{-2.2}$	$60.0^{+2.2}_{-1.7}$	$101.7^{+2.8}_{-3.2}$	$111.9^{+2.5}_{-2.4}$
T_C	Time of conjunction (BJD_{TDB})	$2459847.67307^{+0.00091}_{-0.00092}$	$2459847.673^{+0.00093}_{-0.0009}$	$2459789.41867 \pm 0.00079$	$2459789.4187^{+0.00078}_{-0.00079}$
T_0	Optimal conjunction time (BJD_{TDB})	$2460105.74424^{+0.00064}_{-0.00063}$	$2460105.74423^{+0.0006}_{-0.00062}$	$2459882.77168 \pm 0.00077$	$2459882.77175^{+0.00076}_{-0.00077}$
a	Semi-major axis (AU)	$0.0623^{+0.001}_{-0.0013}$	$0.06576^{+0.0012}_{-0.00093}$	$0.06251^{+0.00085}_{-0.001}$	$0.06558^{+0.00072}_{-0.0007}$
i	Inclination (Degrees)	$83.56^{+0.36}_{-0.38}$	84.14 ± 0.34	$87.7^{+1.4}_{-1.3}$	$89.02^{+0.69}_{-0.97}$
e	Eccentricity	$0.006^{+0.0081}_{-0.0042}$	$0.0066^{+0.0087}_{-0.0047}$	$0.0203^{+0.0034}_{-0.0038}$	$0.0199^{+0.0034}_{-0.004}$
ω_*	Argument of periastron (Degrees)	-77.0^{+86}_{-47}	-78.0^{+80}_{-37}	$96.5^{+5.9}_{-5.8}$	$96.5^{+6.1}_{-6}$
T_{eq}	Equilibrium temperature (K)	1512.0^{+47}_{-43}	1540.0 ± 47	1663.0^{+27}_{-23}	1630.0^{+20}_{-19}
$\tau_{\rm circ}$	Tidal circularization timescale (Gyr)	258.0^{+80}_{-62}	378.0^{+110}_{-87}	214.0^{+90}_{-63}	241.0^{+95}_{-64}
K	RV semi-amplitude (m/s)	5656.0^{+40}_{-48}	5655.0^{+40}_{-46}	9954.0^{+31}_{-33}	9954.0^{+32}_{-34}
R_P/R_*	Radius of planet in stellar radii	0.0586 ± 0.0012	0.0574 ± 0.0011	$0.0561^{+0.0033}_{-0.0034}$	$0.0558^{+0.0034}_{-0.0035}$
a/R_*	Semi-major axis in stellar radii	7.63 ± 0.31	$8.16^{+0.34}_{-0.31}$	$6.45^{+0.18}_{-0.27}$	$6.635^{+0.077}_{-0.11}$
Depth	*TESS* flux decrement at mid-transit	0.00317 ± 0.0001	$0.003137^{+0.000099}_{-0.000098}$	$0.00359^{+0.00044}_{-0.00042}$	$0.00361^{+0.00045}_{-0.00044}$
τ	Ingress/egress transit duration (days)	$0.0262^{+0.0028}_{-0.0026}$	$0.0222^{+0.0023}_{-0.0021}$	$0.014^{+0.0015}_{-0.0012}$	$0.01323^{+0.00092}_{-0.00088}$
T_{14}	Total transit duration (days)	$0.1372^{+0.0027}_{-0.0025}$	$0.1339^{+0.0023}_{-0.0022}$	$0.2447^{+0.0024}_{-0.0023}$	$0.2433^{+0.0022}_{-0.0021}$
b	Transit impact parameter	$0.86^{+0.012}_{-0.014}$	$0.838^{+0.015}_{-0.016}$	$0.26^{+0.12}_{-0.15}$	$0.112^{+0.11}_{-0.078}$
ρ_P	Density (cgs)	$66.7^{+12}_{-9.9}$	82.0^{+14}_{-12}	84.0^{+20}_{-16}	89.0^{+20}_{-15}
$\log g_P$	Surface gravity	5.125 ± 0.048	$5.201^{+0.047}_{-0.045}$	$5.286^{+0.061}_{-0.06}$	$5.316^{+0.058}_{-0.054}$
Θ	Safronov number	$6.03^{+0.33}_{-0.3}$	6.21 ± 0.32	$8.89^{+0.65}_{-0.59}$	$8.72^{+0.61}_{-0.53}$
T_S	Time of eclipse (BJD_{TDB})	$2459845.0427^{+0.011}_{-0.0087}$	$2459845.0428^{+0.011}_{-0.0091}$	$2459791.8682^{+0.0062}_{-0.0065}$	$2459791.8684^{+0.0064}_{-0.0065}$
$T_{S,14}$	Total eclipse duration (days)	$0.1381^{+0.0036}_{-0.0031}$	$0.1347^{+0.003}_{-0.0027}$	$0.2539^{+0.0028}_{-0.0029}$	$0.2528^{+0.0029}_{-0.003}$
$e\cos\omega_*$		$0.0009^{+0.0034}_{-0.0026}$	$0.0009^{+0.0034}_{-0.0028}$	$-0.0023^{+0.002}_{-0.0021}$	-0.0022 ± 0.0021
$e\sin\omega_*$		$-0.0031^{+0.0044}_{-0.0097}$	$-0.0041^{+0.005}_{-0.01}$	$0.0201^{+0.0034}_{-0.0038}$	$0.0197^{+0.0034}_{-0.0041}$
M_P/M_*	Mass ratio	$0.04626^{+0.0011}_{-0.00087}$	$0.04365^{+0.00075}_{-0.00091}$	$0.0776^{+0.0014}_{-0.0012}$	0.07359 ± 0.0009
d/R_*	Separation at mid-transit	$7.67^{+0.33}_{-0.32}$	$8.21^{+0.36}_{-0.32}$	$6.32^{+0.18}_{-0.26}$	$6.503^{+0.09}_{-0.12}$

Table 4.7. *(Continued)*

		TOI-4759		**TOI-5882**	
		Low-mass solution (68.2% probability)	High-mass solution (31.8% probability)	Low-mass solution (71.1% probability)	High-mass solution (28.9% probability)
Priors:					
π	Gaia Parallax (mas)	$\mathcal{G}$[1.34392, 0.01465]		$\mathcal{G}$[2.42207, 0.01753]	
[Fe/H]	Metallicity (dex)	$\mathcal{G}$[0.2723, 0.4141]		$\mathcal{G}$[0.1400, 0.1900]	
A_V	V-band extinction (mag)	$\mathcal{U}$[0, 0.1507]		$\mathcal{U}$[0, 0.8438]	
D_T	Dilution in *TESS*	$\mathcal{G}$[0, 0.038128]		$\mathcal{G}$[0, 0.008565]	
Primary Star Parameters:					
M_*	Mass ($M_\odot$)	$1.186^{+0.061}_{-0.079}$	$1.384^{+0.049}_{-0.048}$	$1.334^{+0.055}_{-0.065}$	$1.549^{+0.055}_{-0.053}$
R_*	Radius ($R_\odot$)	$1.953^{+0.1}_{-0.094}$	$1.868^{+0.083}_{-0.077}$	$2.26^{+0.072}_{-0.052}$	$2.334^{+0.047}_{-0.041}$
L_*	Luminosity ($L_\odot$)	$3.5^{+0.2}_{-0.18}$	$3.49^{+0.15}_{-0.16}$	$5.67^{+0.84}_{-0.73}$	$6.65^{+0.84}_{-0.73}$
ρ_*	Density (cgs)	$0.223^{+0.037}_{-0.034}$	$0.299^{+0.038}_{-0.033}$	$0.1635^{+0.0094}_{-0.015}$	$0.1722^{+0.0065}_{-0.0078}$
$\log g$	Surface gravity (cgs)	$3.928^{+0.047}_{-0.052}$	$4.036^{+0.035}_{-0.033}$	$3.856^{+0.018}_{-0.03}$	$3.892^{+0.012}_{-0.013}$
$T_{\rm eff}$	Effective temperature (K)	5650.0 ± 150	5770.0 ± 130	5920.0 ± 210	6060.0 ± 180
[Fe/H]	Metallicity (dex)	$0.17^{+0.21}_{-0.22}$	$0.37^{+0.11}_{-0.15}$	$0.18^{+0.16}_{-0.15}$	0.25 ± 0.15
$[{\rm Fe/H}]_0$	Initial metallicity	$0.18^{+0.18}_{-0.2}$	$0.376^{+0.088}_{-0.13}$	$0.19^{+0.14}_{-0.13}$	$0.28^{+0.12}_{-0.13}$
Age	Age (Gyr)	$6.25^{+1.1}_{-0.86}$	$3.48^{+0.53}_{-0.54}$	$4.11^{+0.66}_{-0.52}$	$2.44^{+0.34}_{-0.33}$
EEP	Equal evolutionary phase	$457.5^{+5.7}_{-6.2}$	$405.3^{+8.6}_{-14}$	$455.4^{+4.4}_{-5.9}$	$405.5^{+7.2}_{-9.2}$
A_V	V-band extinction (mag)	$0.094^{+0.041}_{-0.057}$	$0.109^{+0.031}_{-0.054}$	$0.33^{+0.17}_{-0.18}$	$0.53^{+0.13}_{-0.14}$
d	Distance (pc)	$743.7^{+8.2}_{-8}$	$743.8^{+8.2}_{-7.9}$	$413.0^{+3}_{-2.9}$	$413.8^{+3}_{-2.9}$

Table 4.7 (cont'd)

		TOI-4759		TOI-5882	
		Low-mass solution (68.2% probability)	High-mass solution (31.8% probability)	Low-mass solution (71.1% probability)	High-mass solution (28.9% probability)
Companion Parameters:					
P	Period (days)	$9.657846^{+0.000036}_{-0.000039}$	$9.657845^{+0.000036}_{-0.000039}$	7.148972 ± 0.000014	7.148973 ± 0.000015
R_P	Radius (R_J)	$0.926^{+0.069}_{-0.063}$	$0.867^{+0.056}_{-0.052}$	$1.023^{+0.045}_{-0.038}$	$1.056^{+0.037}_{-0.034}$
M_P	Mass (M_J)	$99.0^{+3.4}_{-4.3}$	$109.4^{+2.6}_{-2.5}$	$22.01^{+0.61}_{-0.72}$	$24.29^{+0.58}_{-0.56}$
T_C	Time of conjunction (BJD_{TDB})	2459226.0099 ± 0.0035	$2459226.0089^{+0.0035}_{-0.0034}$	$2459818.9045^{+0.0013}_{-0.0012}$	$2459818.9044^{+0.0013}_{-0.0012}$
T_0	Optimal conjunction time (BJD_{TDB})	$2459370.8776^{+0.0035}_{-0.0034}$	2459370.8766 ± 0.0034	$2459768.8621^{+0.0013}_{-0.0012}$	$2459768.8621^{+0.0013}_{-0.0012}$
a	Semi-major axis (AU)	$0.0964^{+0.0016}_{-0.0021}$	$0.1013^{+0.0011}_{-0.0012}$	$0.0804^{+0.0011}_{-0.0013}$	$0.08445^{+0.00099}_{-0.00098}$
i	Inclination (Degrees)	$86.97^{+0.58}_{-0.53}$	$87.98^{+0.75}_{-0.53}$	$88.56^{+0.97}_{-1.1}$	$89.25^{+0.52}_{-0.76}$
e	Eccentricity	$0.2411^{+0.0024}_{-0.0026}$	$0.2413^{+0.0024}_{-0.0026}$	0.0339 ± 0.0041	$0.0332^{+0.004}_{-0.0042}$
ω_*	Argument of periastron (Degrees)	-19.2 ± 1.5	-19.1 ± 1.5	$104.7^{+4.9}_{-4.5}$	$105.0^{+5.1}_{-4.6}$
T_{eq}	Equilibrium temperature (K)	1226.0^{+24}_{-18}	1194.0 ± 14	1515.0^{+50}_{-46}	1537.0^{+45}_{-43}
$\tau_{\rm circ}$	Tidal circularization timescale (Gyr)	5400.0^{+2400}_{-1700}	9200.0^{+3300}_{-2400}	369.0^{+74}_{-70}	385.0^{+66}_{-57}
K	RV semi-amplitude (m/s)	8247.0 ± 44	8247.0^{+44}_{-45}	1895.9 ± 7	$1895.9^{+7.2}_{-6.9}$
R_P/R_*	Radius of planet in stellar radii	0.0487 ± 0.0019	0.0477 ± 0.0018	0.0465 ± 0.0013	$0.0465^{+0.0012}_{-0.0013}$
a/R_*	Semi-major axis in stellar radii	$10.59^{+0.55}_{-0.57}$	$11.66^{+0.48}_{-0.45}$	$7.66^{+0.14}_{-0.24}$	$7.786^{+0.097}_{-0.12}$
$Depth$	*TESS* flux decrement at mid-transit	0.00263 ± 0.00019	$0.00261^{+0.0002}_{-0.00019}$	0.00251 ± 0.00014	0.0025 ± 0.00014
τ	Ingress/egress transit duration (days)	$0.0183^{+0.0027}_{-0.0022}$	$0.0146^{+0.0017}_{-0.0015}$	$0.01376^{+0.0011}_{-0.00061}$	$0.01337^{+0.00052}_{-0.00044}$
T_{14}	Total transit duration (days)	$0.2698^{+0.0087}_{-0.0083}$	$0.267^{+0.0086}_{-0.0082}$	0.2969 ± 0.0029	0.2951 ± 0.0029
b	Transit impact parameter	$0.573^{+0.069}_{-0.089}$	$0.42^{+0.095}_{-0.15}$	$0.19^{+0.13}_{-0.12}$	$0.098^{+0.097}_{-0.068}$
ρ_P	Density (cgs)	154.0^{+37}_{-30}	208.0^{+42}_{-35}	$25.4^{+2.9}_{-3}$	$25.6^{+2.5}_{-2.4}$
$logg_P$	Surface gravity	$5.455^{+0.064}_{-0.065}$	5.557 ± 0.053	$4.716^{+0.032}_{-0.036}$	$4.732^{+0.027}_{-0.028}$
Θ	Safronov number	$17.4^{+1.3}_{-1.2}$	$18.5^{+1.2}_{-1.1}$	$2.59^{+0.1}_{-0.11}$	$2.505^{+0.084}_{-0.085}$
T_S	Time of eclipse (BJD_{TDB})	$2459222.573^{+0.014}_{-0.015}$	$2459222.573^{+0.014}_{-0.015}$	2459822.44 ± 0.012	2459822.44 ± 0.012
$T_{S,14}$	Total eclipse duration (days)	$0.2433^{+0.008}_{-0.0075}$	$0.2339^{+0.0068}_{-0.0065}$	0.3158 ± 0.004	$0.3141^{+0.004}_{-0.0039}$
$e\cos\omega_*$		$0.2277^{+0.0024}_{-0.0026}$	$0.2279^{+0.0025}_{-0.0027}$	-0.0086 ± 0.0026	$-0.0085^{+0.0025}_{-0.0027}$
$e\sin\omega_*$		$-0.0791^{+0.0061}_{-0.0062}$	-0.0791 ± 0.0062	$0.0327^{+0.0041}_{-0.0042}$	$0.032^{+0.0041}_{-0.0043}$
M_P/M_*	Mass ratio	$0.0797^{+0.002}_{-0.0015}$	0.0755 ± 0.001	$0.01574^{+0.00027}_{-0.00022}$	$0.01497^{+0.00018}_{-0.00019}$
d/R_*	Separation at mid-transit	$10.83^{+0.57}_{-0.58}$	$11.92^{+0.5}_{-0.46}$	$7.4^{+0.15}_{-0.23}$	$7.53^{+0.11}_{-0.13}$

4.4.1 Multi-star Fitting in EXOFASTv2

As discussed in §4.3.4, a stellar companion to TOI-4462 was detected 0.4″away, which was blended in all catalog photometry and a significant factor in the dilution of the transit light curves. Given that the probability of a chance alignment is low, and the high Gaia Re-normalized Unit Weight Error (RUWE) of 3.13, we assumed this companion is bound to the primary star. We undid the deblending that SPOC applies to the TESS lightcurves so that we could more accurately model it based on our multi-component SED model. We modeled both stars simultaneously, each with their own MIST evolutionary model, while assuming that the age, initial metallicity, distance, and extinction is the same for both stars. In addition, we modeled a spectral energy distribution for each star, constraining the sum of both stars with the catalog photometry of the unresolved TOI-4462 system, and the difference between the two stars with the AO photometry from PHARO, as shown in Figure 4.1 (Left). We therefore fit for dilution terms that were then constrained by the multi-component SED model, integrated at the transit-observed bands assuming a 5% floor in the theoretical dilution from the model atmospheres. That is, we applied an adaptive prior penalty of

$$\ln \mathscr{L} = 0.5 \left(\frac{D_{\rm Step} - D_{\rm SED}}{0.02 D_{\rm Step}} \right)^2 \tag{4.1}$$

where $D_{\rm Step}$ is the modeled dilution at the current MCMC step and $D_{\rm SED}$ is the SED-derived dilution. This naturally propagates the uncertainty in the stellar properties, accounting for systematics in the theoretical atmospheres, to the light curve de-blending and transit depth.

4.5 Discussion

The 5 BD-mass companions presented here increase the population of transiting brown dwarfs to over 50. While this number is expected to continue growing, it is worth analyzing the sizable population that has been put together thus far in the context of planet-like and star-like formation. We have also added 6 new transiting low-mass stars to the population > 80 M_J. Accurate mass and radius measurements are rare for these objects which will be vital for anchoring our understanding of stellar formation and evolution. We may find that early trends or features observed in the growing population from previous efforts have been reinforced, or lost significance (perhaps even

disappearing) in the wake of new discoveries. One such feature of particular interest is the so-called "brown dwarf desert" and its potential role in dividing the brown dwarfs into distinct planet-like and star-like groups. We discuss these trends below in §4.5.1 and §4.5.2. We also note that one of the BD-hosting stars presented here, TOI-5882, has a significant absorption feature at 6708 Å which we attribute to lithium. We discuss in §4.5.3 the implications of this, as well as how it affects our determination of the system's age.

4.5.1 The Transiting Brown Dwarf Desert

Perhaps the most discussed feature to emerge from the growing transiting BD population is that of the brown dwarf desert. The phrase was originally coined in the earliest days of exoplanet discovery (Marcy et al., 1997; Latham et al., 1998) in reference to the lack of BD-mass companions discovered by RV surveys at that time. It has since evolved over time with studies like Grether & Lineweaver (2006) which analyzed RV-detected companions with periods less than 5 years and found the "driest" part of the desert was between $13-56\ M_J$. Then Ma & Ge (2014) examined trends in the RV discovered population and refined the measurement to be between $35 < m\ \sin i < 55\ M_J$ and with $Period < 100$ days.

We now have a more substantial population of transiting BD systems which have precisely measured radii and masses. It's worth exploring how well the trends found in the the RV discovered sample hold up in the transiting BD regime. Of course, because of the transit probability decreases with period, transiting systems tend to have much shorter orbital periods than their counterparts discovered through direct imaging and RV campaigns. As a result we are largely investigating a different, more limited parameter space than the previous studies of Ma & Ge (2014) for example. We found that the most sparsely populated area of the transiting BD desert appears to be the entire low-mass BD regime ($<\sim 42 M_J$), and the work presented here contributes 1 new BD (TOI-5882) to this underpopulated region (see Figure 4.2). We also note that the apparent drop off in systems with companions above the substellar limit ($80\ M_J$) is likely unphysical and is more plausibly due to selection bias since most of these systems have been discovered via exoplanet discovery pipelines. In order to more accurately describe trends emerging near the hydrogen fusion boundary, a more

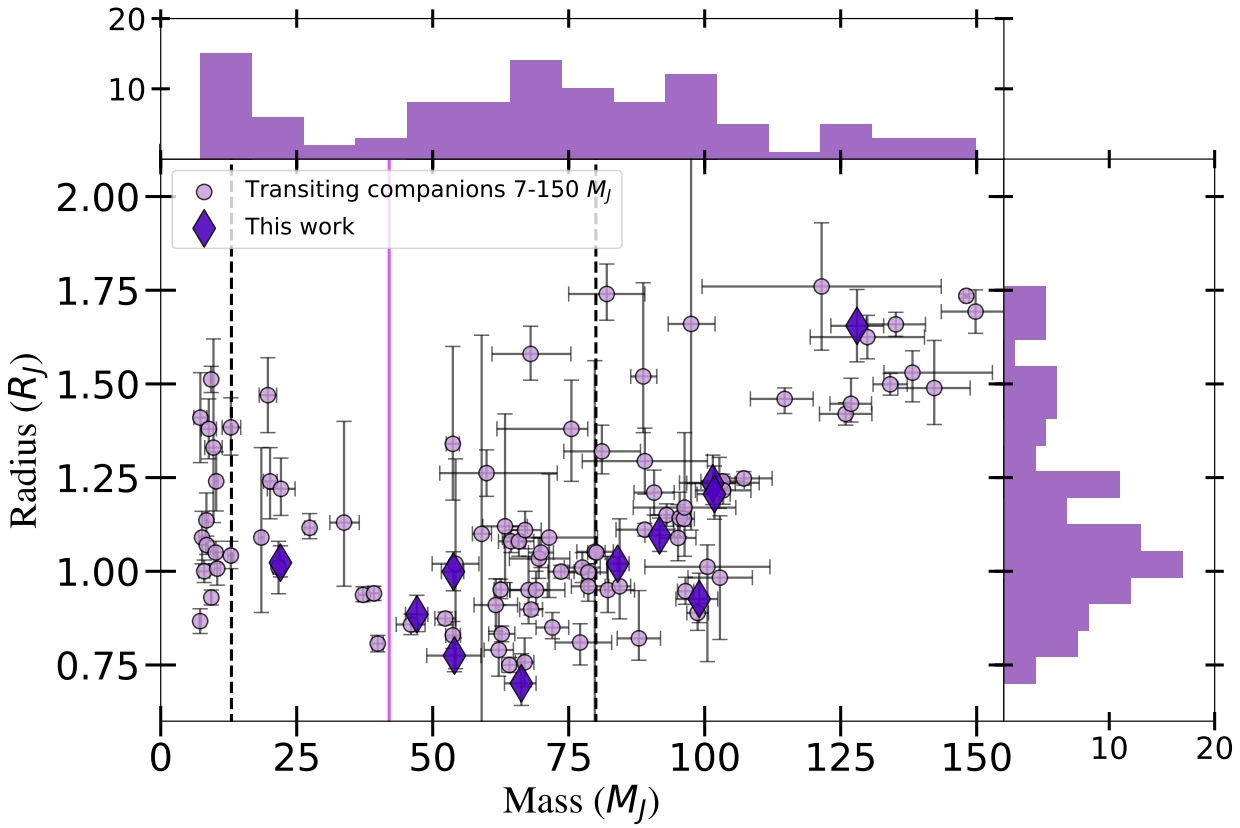

Figure 4.2 Radius versus mass for all transiting companions from 7 - 150 M_J. The black dashed lines depict the canonical 13 and 80 M_J BD boundaries. The solid purple line at 42 M_J shows the proposed Ma & Ge (2014) boundary between planet and star-like BDs. **Note:** systems where the primary object is a white dwarf or brown dwarf are not shown. **References:** Henderson et al. (2024a) and references therein as well as Bakos et al. (2010); Buchhave et al. (2011); Tingley et al. (2011); Parviainen et al. (2014); Bonomo et al. (2015); Esteves et al. (2015); Stassun et al. (2017); Bento et al. (2018); Cañas et al. (2018); Cooke et al. (2020); Cortés-Zuleta et al. (2020); El-Badry et al. (2023); Lambert et al. (2023); Schmidt et al. (2023); Dalba et al. (2024); Davis et al. (2024); Eberhardt et al. (2023); Henderson et al. (2024b); Swayne et al. (2024); Wang et al. (2024)

unbiased sample will need to be produced.

Another key trend that was first noted by the Ma & Ge (2014) RV study is in the eccentricity vs $m \sin i$ distribution. They found that eccentricity decreases as companion mass increases up until $m \sin i \sim 42\ M_J$, right in the middle of the driest part of the brown dwarf desert. On the other hand, companions more massive than 42 M_J cover a much larger range in eccentricity and little to no correlation with the companion mass. The authors attributed this trend as evidence of a ~42 M_J transition point between the planet and star formation mechanisms. As the transiting BD

population has developed, several studies have drawn comparisons to these results, some finding evidence for the same trends (Grieves et al., 2021; Henderson et al., 2024b), while others have noted low-mass BDs with higher than expected eccentricities (Page et al., 2024). However, such claims have historically been subject to the small sample size and selection effects that accompany the transiting BD population. Now that this population exceeds 50 systems, we can at least start to alleviate the risks of small number statistics. Figure 4.3 (Left) shows the eccentricity vs. companion mass distribution for the transiting brown dwarfs, and it is clear that there are more systems above 42 M_J with high eccentricity than there are below. About 30% of systems below 42 M_J have eccentricities > 0.1 compared to about 45% for their higher-mass counterparts. However, we argue that this trend alone is not necessarily supportive of a 42 M_J transition between the planet and stellar formation mechanisms. If the low-mass transiting BDs are indeed dominated by the planet formation mechanism, then they should be subject to the same evolutionary pathways as the hot Jupiters. The hot Jupiter eccentricity distribution has been shown to be most consistent with high eccentricity migration mechanisms and thus are ultimately sculpted by tidal recircularization (Rodriguez et al., 2023; Schulte et al., 2024). We know that this process depends more fundamentally on the mass ratio of the system rather than just the companion mass as evidenced by the tidal recircularization time scale (Equation 2 of Adams & Laughlin, 2006). So, if the trend in eccentricity vs companion mass were indeed indicative of a separation between planet-like and star-like formation processes, then we should expect to see the same trends emerge in eccentricity vs mass ratio. Namely, low mass ratio systems should exhibit a much smaller range of eccentricities than their high mass ratio counterparts. However, as shown in Figure 4.3 (Right), we see the opposite. The eccentricity dichotomy between low and high mass companions seems to disappear when plotted against mass ratio. We therefore argue that the eccentricity vs companion mass distribution of transiting companions does not support a 42 M_J transition point.

4.5.2 Transiting Brown Dwarf Metallicities

Eccentricity is likely not the only parameter that could offer insight into at which critical companion mass the dominant formation mechanism turns over from planet-like to star-like. For

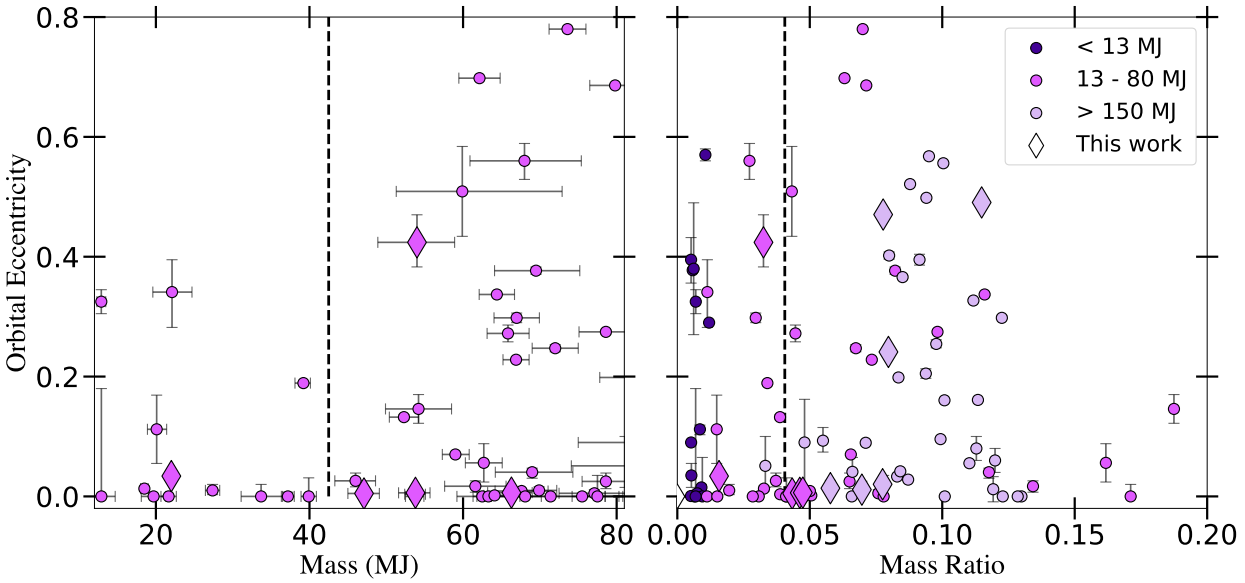

Figure 4.3 (Left) Eccentricity versus mass for transiting BDs with a dotted line at the proposed Ma & Ge (2014) boundary between planet and star-like BDs. (Right) All transiting companions ranging from 7 - 150 M_J in eccentricity versus mass ratio with a dashed line at the same 42 M_J location assuming a 1.0 $M_\odot$ host star. As discussed in §4.5.1, the eccentricity dichotomy between low and high mass BDs does not hold up when plotted against mass ratio, suggesting that this feature may not represent the boundary between planet-like and star-like BDs.

nearly three decades we have known of the giant planet-metallicity correlation, in which hot Jupiter hosting stars tend to be more metal rich than their counterparts with no discovered planets (Gonzalez, 1997; Santos et al., 2003; Fischer & Valenti, 2005). If the low-mass transiting BDs are predominantly forming in the same way as the hot Jupiters, then we should expect their host stars to exhibit the same metallicity enhancement when compared to the high-mass BD hosts. Schlaufman (2018) tested this hypothesis using the metallicities of transiting companions in the range $0.1 - 300$ M_J to show that transition between core accretion and fragmentation may be as low as $4 - 10$ M_J. However, at the time of this study, there were only 27 transiting companions known between $13 - 300$ M_J limiting the ability to probe potential higher-mass transition points. Now that we have access to significantly more systems in this mass regime, we can better probe the same ~42 M_J transition. In Figure 4.4 we show a preliminary look at testing this hypothesis. Qualitatively, it appears that the lower-mass companions ($7 - 42$ M_J) preferentially orbit more metal-rich host stars. However, a two-sample Kolmogovorov-Smirnov test yields a p-value of 0.35, too high to reject

the null hypothesis that the high mass and low mass samples are drawn from the same underlying distribution.

We note also a few important caveats for interpreting the metallicity distribution. First, we chose a 42 M_J cutoff for historical reasons in order to compare to the original hypothesis presented by Ma & Ge (2014) as well as the eccentricity distribution presented in §4.5.1. It may be that a more appropriate boundary separating the population will be found after a more comprehensive analysis which may be in better agreement with the lower-mass Schlaufman (2018) transition. With just 26 companions below 42 M_J in our $7 - 150$ M_J sample, we chose not to investigate possible lower-mass transitions. A more in-depth analysis including the population of giant planets will need to be done to more precisely probe a lower mass transition. An unbiased sample of the population of companions across the substellar limit will also be required to better understand the selection effects currently affecting this population. We note also that the metallicities presented here are the reported values from each system's discovery which have been measured using a variety of different techniques and therefore the underlying biases affecting each measurement are not explored here.

4.5.3 Lithium Detected in TOI-5882

During our analysis of TOI-5882's spectra, we found a significant absorption feature at 6708 Å which we attribute to the lithium doublet. We measured the equivalent width of this feature using the `specutils` (Earl et al., 2022) package in Python (see Figure 4.5). To perform this measurement, we first co-added all of the observed TRES spectra, after correcting each for the RV shift, to increase the signal-to-noise resolution (SNR) of the Li feature. The resulting co-added echelle order containing Li has an SNR of 56.8. Then, we defined a 1.4 Å region centered on the rest wavelength of the Li doublet at 6707.844 Å to measure the equivalent width. The resulting equivalent width is 71.2 ± 6.89 mÅ, where the uncertainty was estimated using Equation 6 in Cayrel (1988).

The presence of lithium in stars is typically interpreted as an indicator of youth. This is due to the temperatures and pressures in the core being sufficiently high to destroy Li, which results in Li visible on the stellar surface slowly depleting as transport occurs between the core and the surface

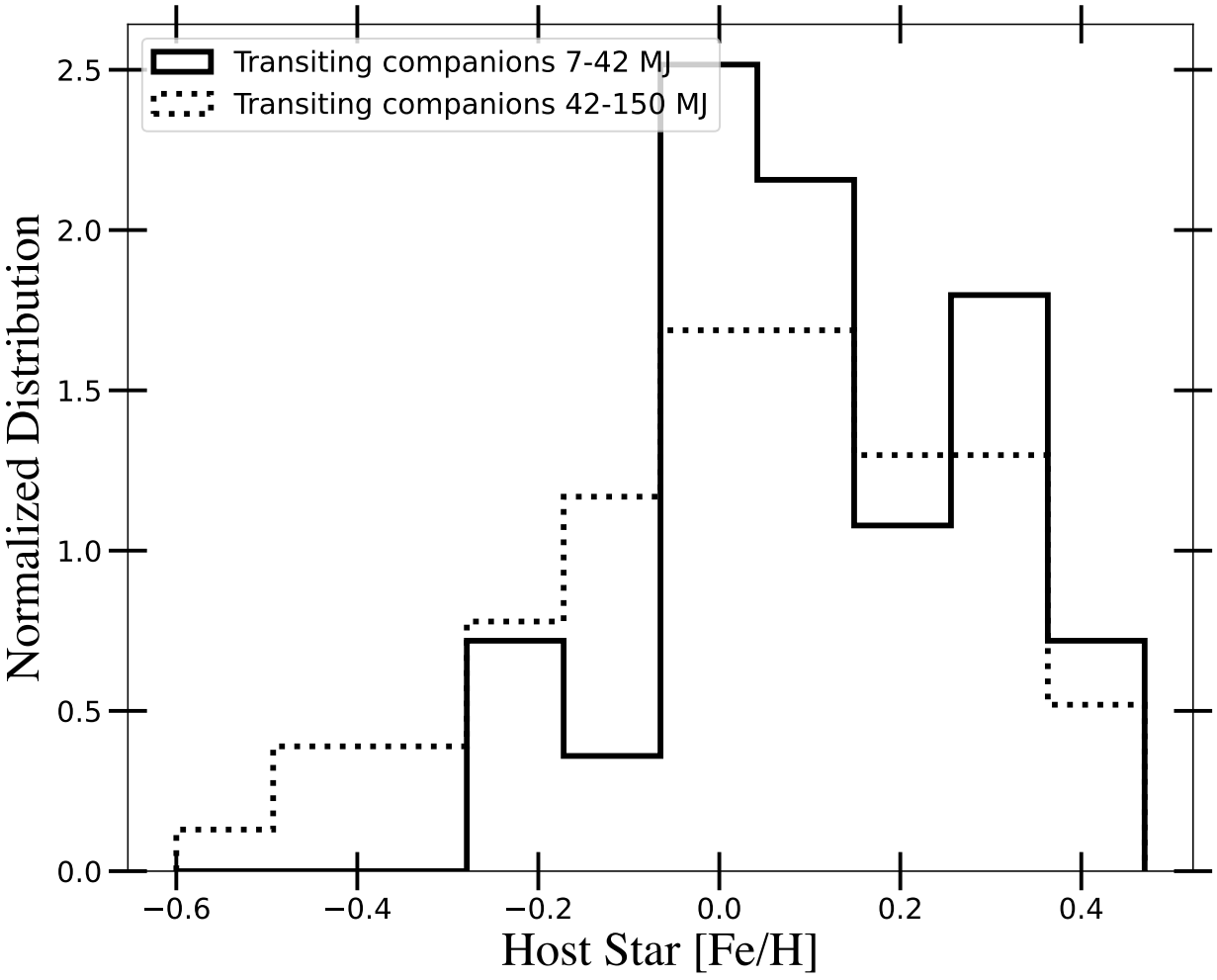

Figure 4.4 The solid-lined histogram depicts the metallicity distribution of transiting companions ranging from 7 - 42 M_J while the dotted-lined histogram depicts the metallicity distribution of transiting companions from 42 - 150 M_J. Both histograms are normalized such that their areas are equal to 1. There appears to be a slight trend towards higher metallicities for host stars with lower mass companions. **Note:** The metallicities shown here are the values cited by their original discovery papers, and hence represent a heterogeneous sample with a variety of different measurement techniques.

of the star (Soderblom et al., 2014). Despite this, we claim that TOI-5882 is likely not a young star, since we found no other signs of youth. To verify this, we performed a period search on each sector of TOI-5882's *TESS* light curves to characterize the rotation of the host star. Since young stars are typically born rapidly rotating and gradually spin down over time, an age can often be inferred from a star's rotation period if it is below the Kraft break (Bouma et al., 2023). We found a significant peak in the periodogram at 9.6 days, however, we are hesitant to adopt this as the true rotation period since periodicity beyond 1/3 of a *TESS* observing sector ($\sim$ 9 days) can be unreliable due to aliases induced by the *TESS* observing strategy and processing of light curves. Even if we were to believe that the 9.6 day periodicity is truly due to stellar rotation, it is still anomalous when compared to the observed rotation periods of young stars. T Tauri stars for example rarely exhibit rotation periods longer than 8 days (Serna et al., 2021), and gyrochronology shows that a 9.6 day period would be indicative of an age of approximately 1 Gyr given this star's effective temperature (Bouma et al., 2023). While a young age for TOI-5882 cannot be conclusively ruled out by its rotation, it is unlikely, especially combined with the lack of other youth indicators.

For example, we also searched for nearby comoving stars using `FriendFinder` [5] (Tofflemire et al., 2021) since their presence would indicate that TOI-5882 and its hypothetical nearby comovers have not yet dispersed from their birth location and hence would be young. `FriendFinder` identifies all nearby sources that fall within a selected search radius, and calculates the predicted tangential velocity $v_{\rm tan}$ for each source, assuming that they have Galactic velocity components (U,V,W) identical to TOI-5882. This predicted v_{tan} is then compared to the true $v_{\rm tan}$ which is derived from *Gaia* proper motions. Using a physical search radius of 30 pc around TOI-5882 and a difference between the predicted and measured $v_{\rm tan}$ of < 5 km s^{-1} we find no evidence that TOI-5882 is part of a comoving group. Furthermore, the nearest star-forming regions in Cygnus, where TOI-5882 is located, are much further away ($>$ 1 kpc; Reipurth & Schneider, 2008).

Finally, we looked for an infrared excess as well as Hα emission. Young stellar objects that retain a circumstellar disk show increased emission at infrared wavelengths (Cotten & Song, 2016).

[5] `https://github.com/adamkraus/comove`

We ruled out an infrared excess for TOI-5882 via our SED fitting in the global analysis where we see no significant infrared emission above the blackbody model in any of the WISE $W1$, $W2$, and $W3$ bandpasses. The presence of Hα lines in emission is also characteristic of active young stars (Briceño et al., 2019), and we found no evidence of such emission. While the lack of these additional youth indicators do not completely rule out the possibility of a young host star, we believe it is more likely that TOI-5882 is a late subgiant star, as indicated by our most probable `EXOFASTv2` solution. This older age could then imply that the presence of Li is due to the infall of planetary material onto the host star. For a deeper dive into the origin of Li in TOI-5882, including its potential as system that has undergone a planetary engulfment, we alert the reader to Kotten et al. (in prep).

4.6 Conclusions

In this paper, we present the discovery of 11 new transiting companions from the *TESS* mission. We collected photometric time-series, spectroscopic, and high resolution imaging follow-up as a part of the *TESS* Follow-up Observing Program (TFOP) to rule our false positives and further characterize each system. Using `EXOFASTv2` , we performed a global fit on each system using the space and ground-based transits, spectroscopic RVs, and archival photometry to characterize both the host stars, and their transiting companions. We found that 5 of these systems are brown dwarfs ($13 < M_2 < 80 M_J$) and 6 of them are very low mass stars from $80 < M_2 < 130\ M_J$. This contribution to the transiting brown dwarf population increases it to 54 systems, a milestone that represents the population outgrowing the burdens of small sample statistics.

Using this population that *TESS* has rapidly developed to a significant size, we offered some initial insight into the features that have started to appear. We revisit the idea of the "brown dwarf" desert for the short orbital periods probed by the transit method. We revisited the eccentricity-mass distribution that has been claimed as evidence of a 42 M_J transition between planet and star formation and showed that this trend does not seem to hold in eccentricity versus mass-ratio, calling into question whether eccentricity truly does offer insight into the formation mechanisms behind these rare objects. We also examined the metallicity distribution of transiting BD host stars

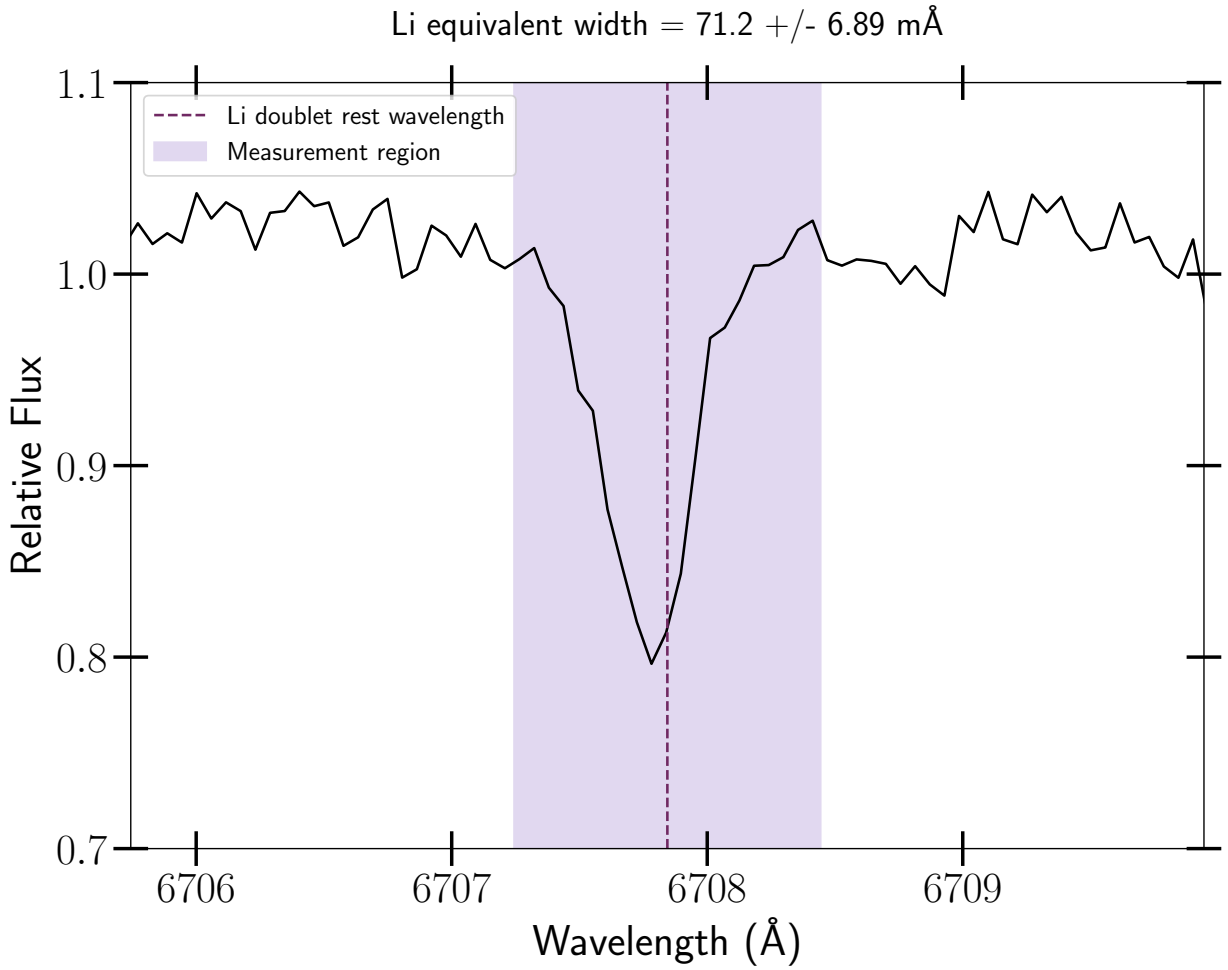

Figure 4.5 The co-added spectra of TOI-5882 zoomed in to the Li absorption line at 6708 Å. The measurement region used to determine the equivalent width is shaded in purple with the dashed line at the center indicating the rest wavelength of the Li doublet, 6707.844 Å.

for the first time, and find that a 42 M_J transition does not divide the population into two distinct populations with any statistical significance.

Finally, we noted the presence of Li in the spectrum of TOI-5882, the host star of our lowest mass BD. We measured the equivalent width of the Li line and search for other signs of youth. Seeing no evidence of youth from any of the other indicators that we examined, we adopt the age provided by our global `EXOFASTv2` fit and do not interpret the presence of Li as a sign of youth. Instead, we noted that the Li may actually be a signature of engulfed planetary material, and that more work will be required to explore this hypothesis.

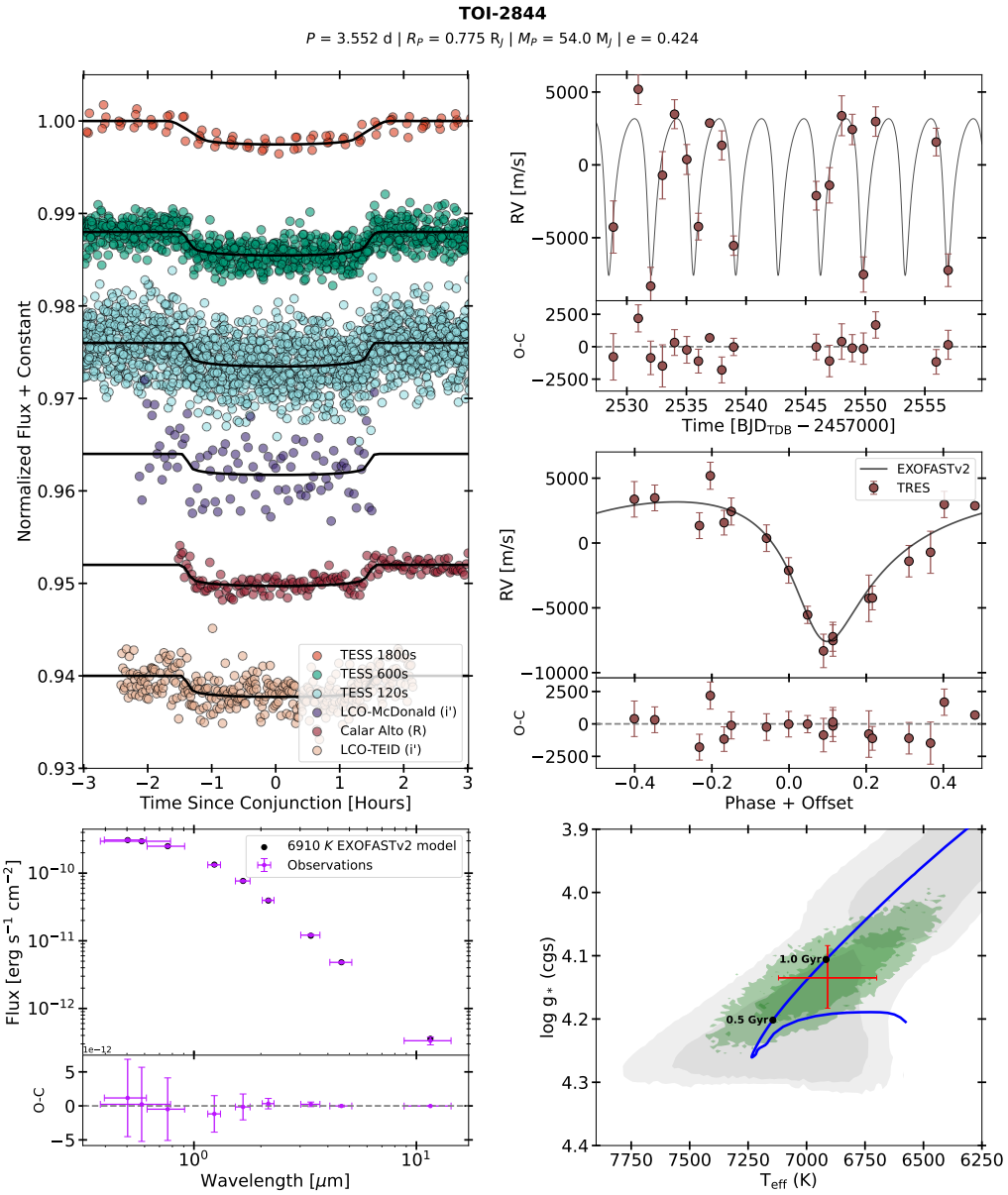

Figure 4.6 *TESS*, Follow-up and archival observations of TOI-2844 compared to the the `EXOFASTv2` results. **Upper left**: *TESS* and follow-up ground-based transits, phase-folded and shown in comparison to the best fit `EXOFASTv2` model. **Bottom left**: The spectral energy distribution of the target star compared to the best-fit `EXOFASTv2` model. **Upper right**: RV observations versus time, including any significant long-term trend. The residuals are shown in the subpanel below in the same units. **Middle right**: RV observations phase-folded using the best-fit ephemeris from the `EXOFASTv2` global fit. The residuals are shown in the subpanel below in the same units. **Bottom right**: The evolutionary track and current evolutionary stage of the primary star according to the best-fit MESA Isochrones and Stellar Tracks (MIST) model. The blue line indicates the best-fit MIST track, while the gray shaded contours show the 1σ and 2σ constraints on the star's current $T_{\rm eff}$ and $\log g$ from the MIST isochrone alone. The green contours represent the 1σ and 2σ constraints on the star's $T_{\rm eff}$ and $\log g$ from the `EXOFASTv2` global fit. The red cross indicates the median and 68% confidence interval reported in Table 4.6.

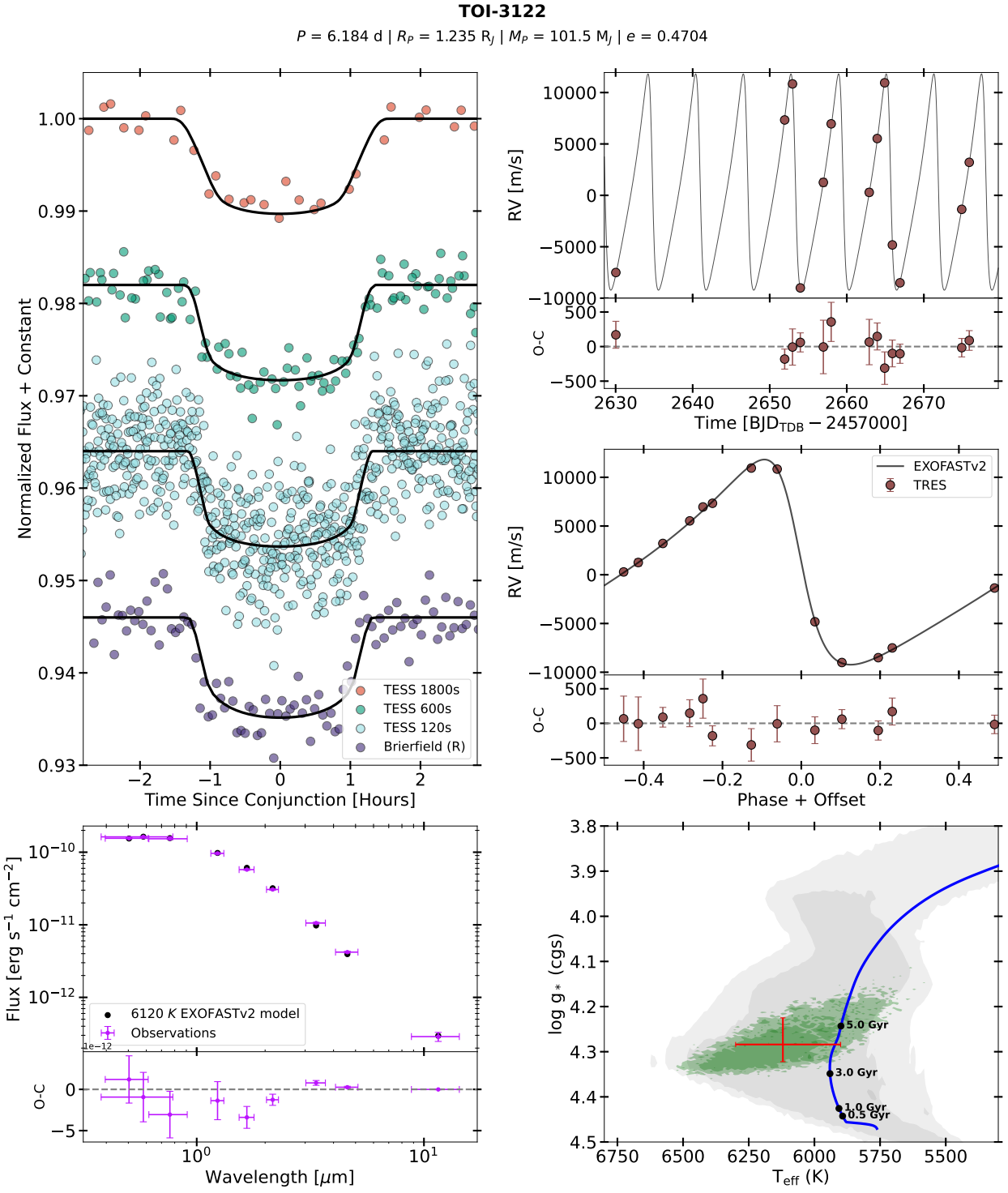

Figure 4.7 Same as Figure 4.6 except for TOI-3122.

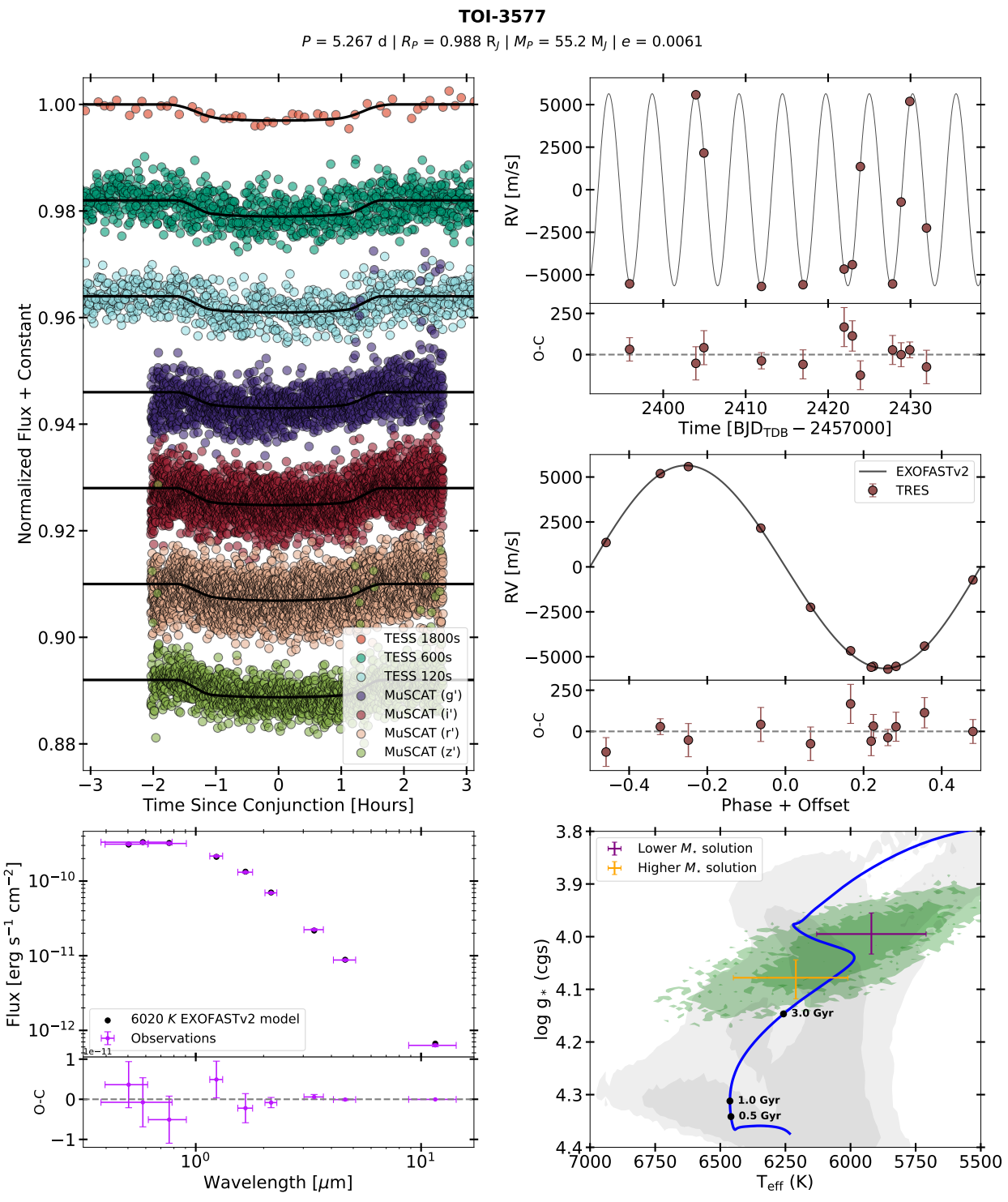

Figure 4.8 Same as Figure 4.6 except for TOI-3577. TOI-3577's fit resulted in a bimodal solution. We characterized both solutions independently as described in §4.4, and they are both are shown in the **bottom right** plot.

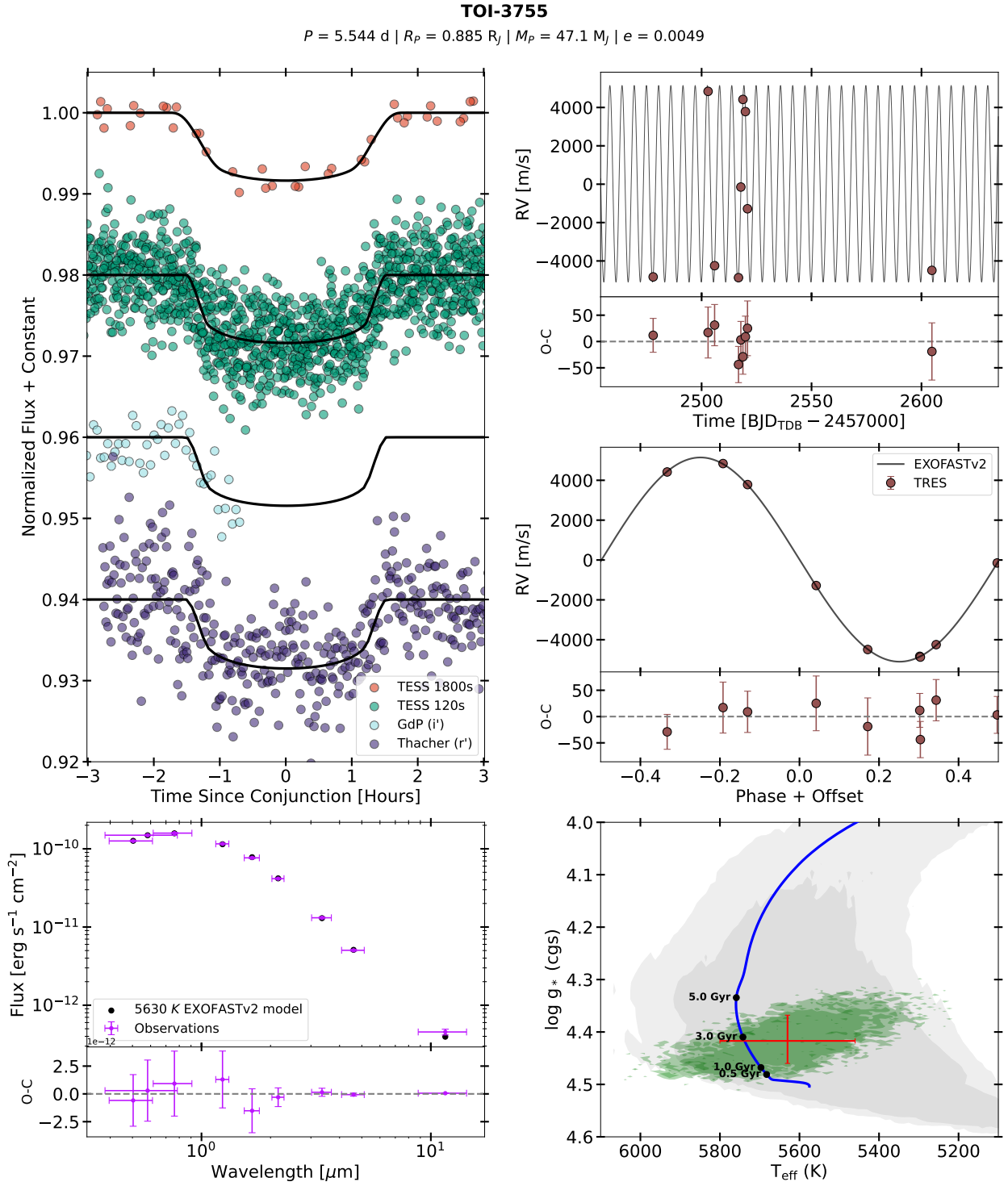

Figure 4.9 Same as Figure 4.6 except for TOI-3755.

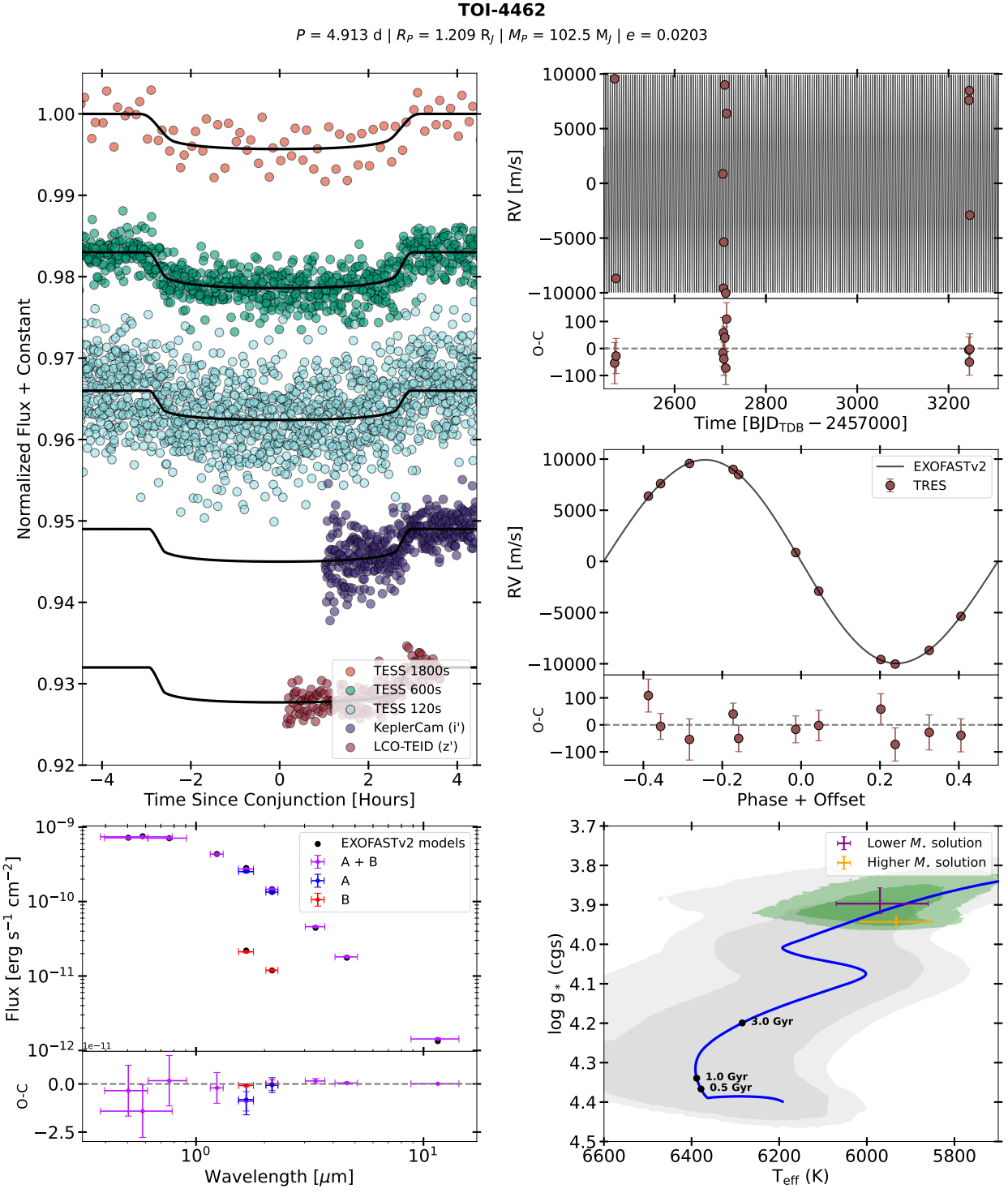

Figure 4.10 Same as Figure 4.8 except for TOI-4462. Both TOI-4462 A and B are shown in the **bottom left**. The `EXOFASTv2` models for TOI-4462 A and B are 5970 *K* and and 4660 *K* respectively.

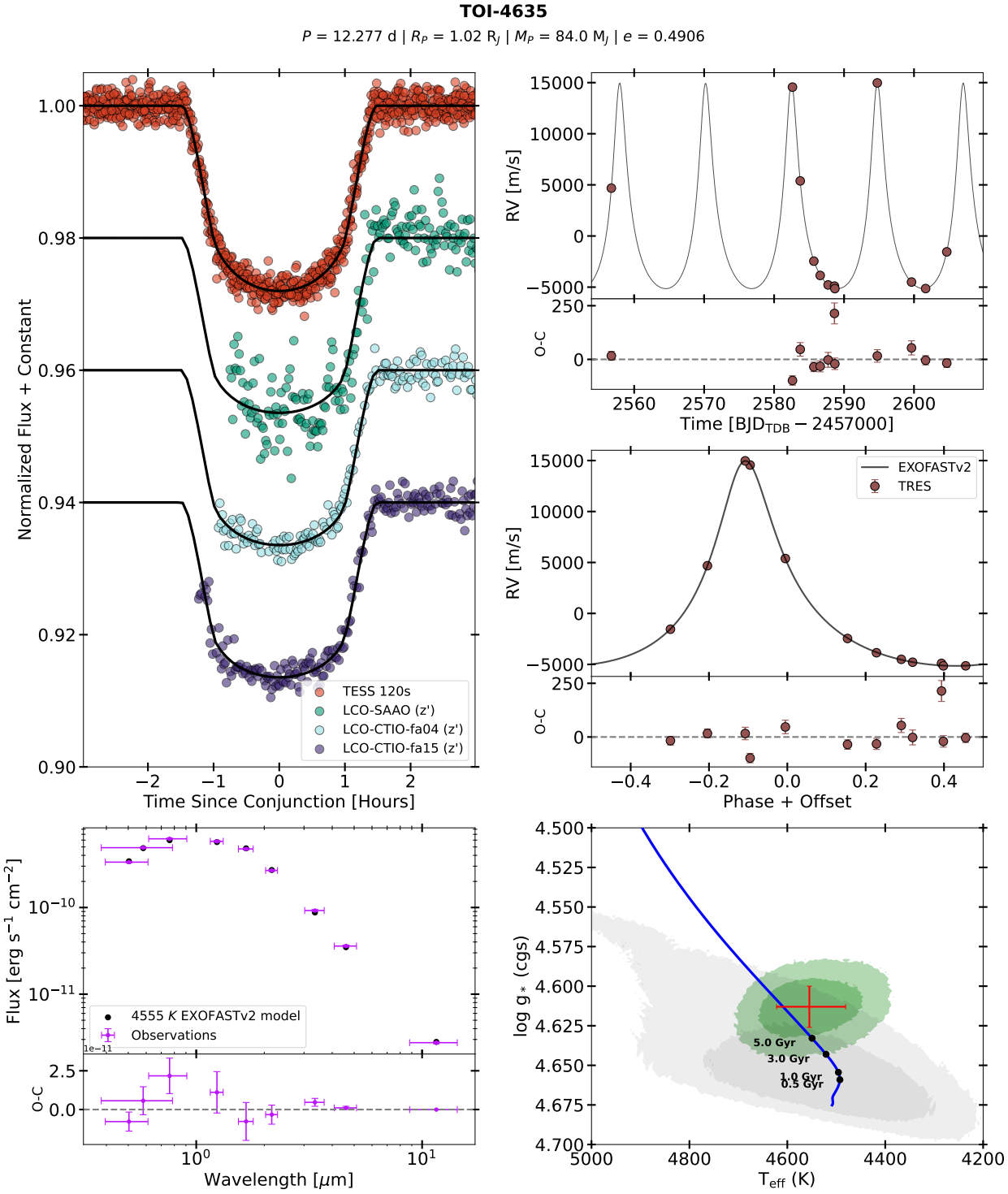

Figure 4.11 Same as Figure 4.6 except for TOI-4635.

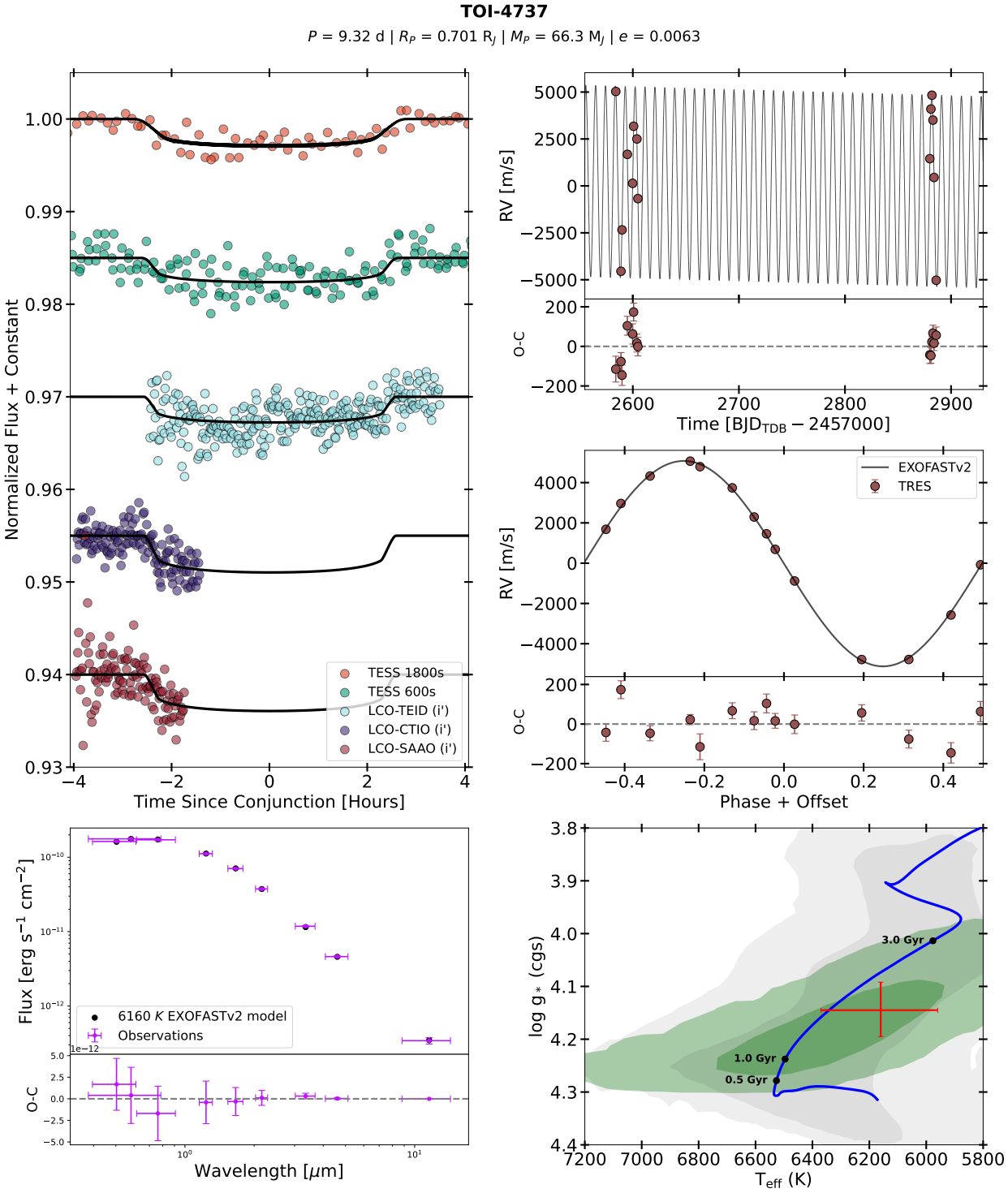

Figure 4.12 Same as Figure 4.6 except for TOI-4737.

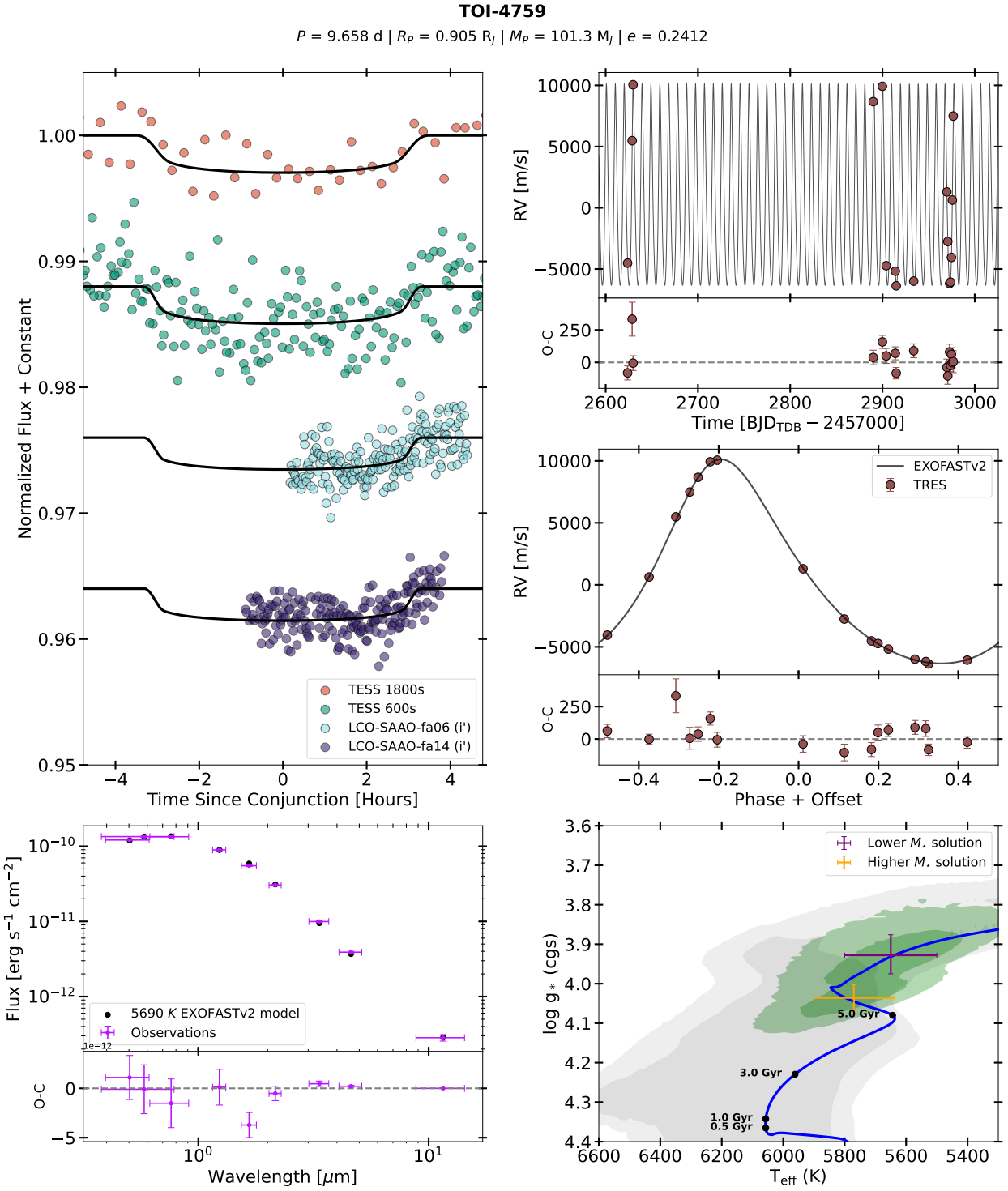

Figure 4.13 Same as Figure 4.8 except for TOI-4759.

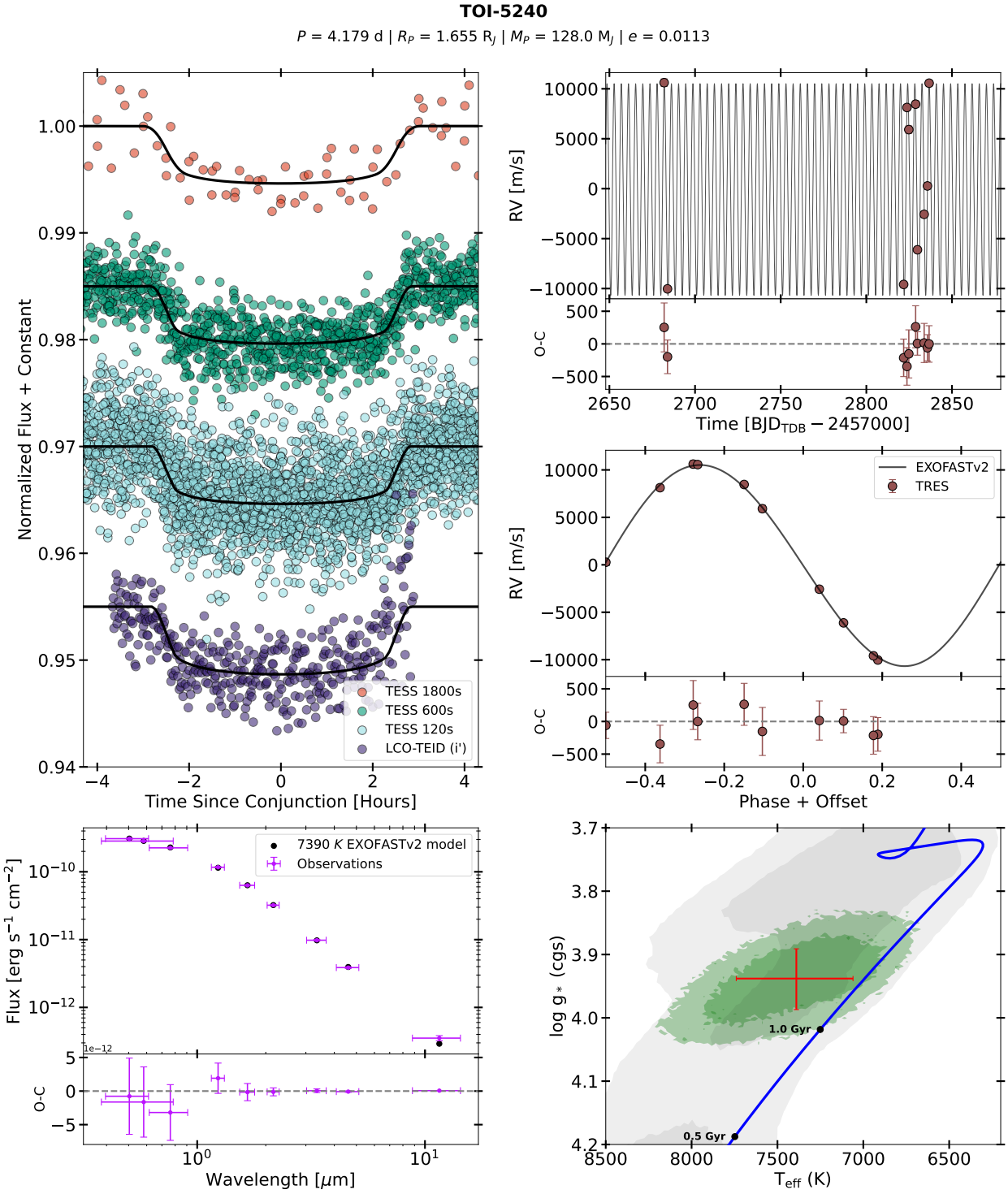

Figure 4.14 Same as Figure 4.6 except for TOI-5240.

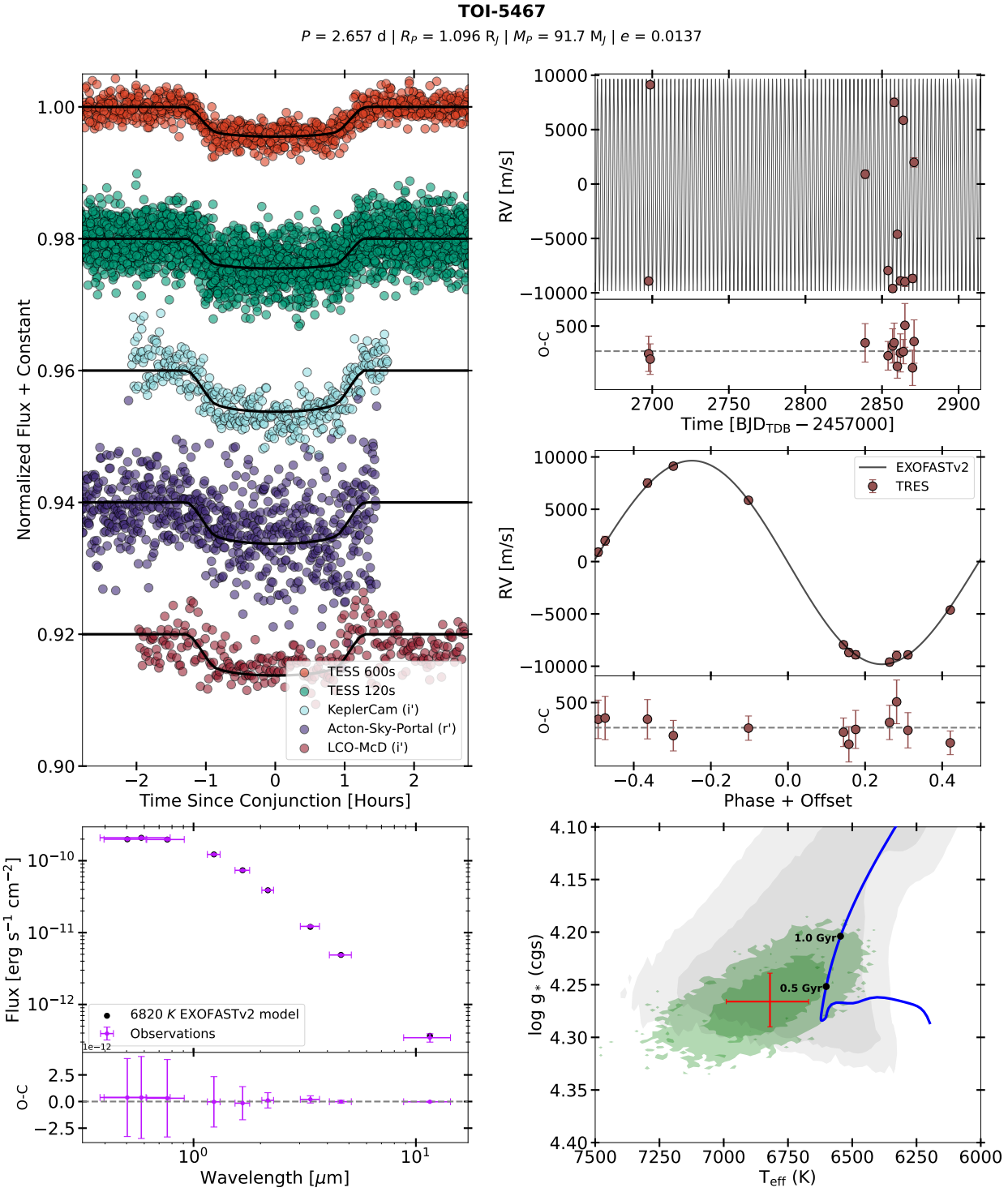

Figure 4.15 Same as Figure 4.6 except for TOI-5467.

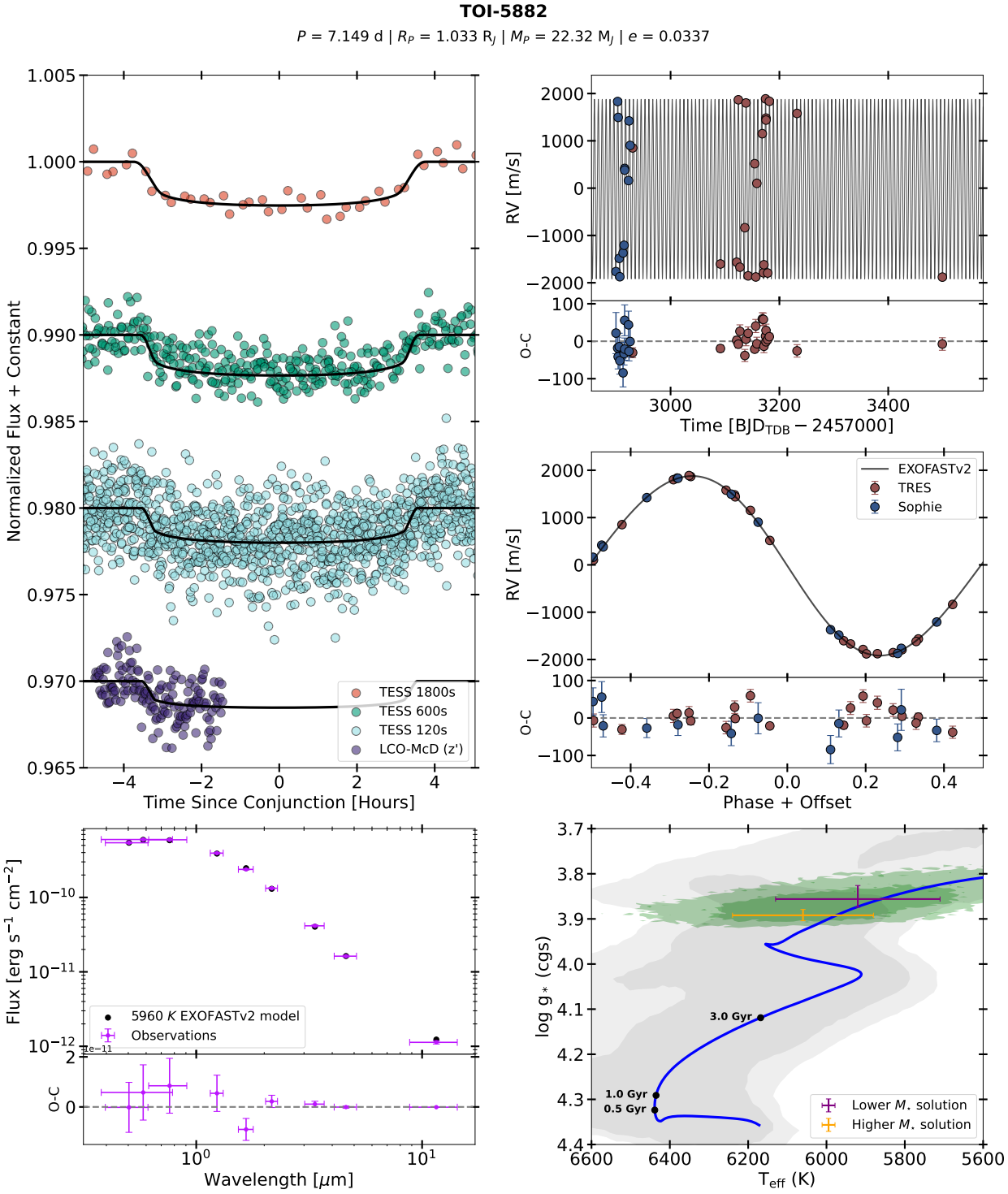

Figure 4.16 Same as Figure 4.8, except for TOI-5882.

CHAPTER 5

CONCLUSIONS AND FUTURE WORK

5.1 Conclusions

This thesis is ultimately motivated by the question: "How big can a planet be?" and conversely, "How small could a star be?". Theory predicts that the formation mechanisms behind these objects overlap in the mass regime occupied by BDs. Historical demographic studies of BDs have suggested a wide range of potential transition points between planets and stars, but have been fraught with small number statistics, heterogeneous samples, and observational degeneracies. This work aims provide new constraints on the planetary-stellar boundary, leveraging a newly cultivated sample of BDs that transit their host stars, significantly mitigating the limitations of previous studies. The following sections summarize each chapter of this thesis and their contributions towards this goal. Finally, we conclude by outlining the next steps for this work and discussing how it may be expanded to include astrometrically detected brown dwarf companions, a particularly timely prospect given the imminent release of Gaia Data Release 4 (DR4).

5.1.1 Chapter 2: HIP 33609 b Discovery

Here we presented the discovery and confirmation of a new benchmark transiting BD, HIP 33609 b. We outlined the discovery process utilizing photometric and spectroscopic follow-up to rule out false positive scenarios, and we described combining all available datasets to characterize the system using the `EXOFASTv2` software. We found that this is a $M_b = 68\ M_J$, $R_b = 1.5\ R_J$ transiting BD on a 39 day eccentric orbit. It orbits a 10,400 K star with a V-band magnitude of 7.3. It is among the most eccentric and largest transiting BDs discovered, and its host star is both the hottest and brightest to host a transiting BD. These properties, combined with a precisely measured age, make HIP 33609 an ideal benchmark system for future characterization efforts.

We also found that HIP 33609 is a member of a previously undiscovered comoving group of stars, MELANGE-6. We confirmed and characterized the stellar association through a combined kinematic, photometric, and rotation period analysis estimating the age of the cluster to be 150 ± 25 Myr. We explained that precise age measurements for transiting BDs are extremely valuable

since they allow us to break the degeneracies between mass, radius, and age present in substellar models. With precise, model independent measurements on these three parameters we conducted a comparative analysis to substellar evolutionary models showing that HIP 33609 b is only slightly inflated, as it is consistent with a 150 Myr isochrone within 3σ.

5.1.2 Chapter 3: The Stellar Obliquity of HIP 33609 b

Chapter 3 presented our measurement of HIP 33609 b's stellar obliquity. We used Doppler tomography to constrain the relative misalignment of the BD's orbit to its host star. We measured a sky-projected stellar obliquity of $|\lambda| = 12.7 \pm 1.3°$. We then combined this measurement with our previous characterization of the system to provide a holistic picture of HIP 33609 b's formation and evolutionary history. We showed that the BD's mass alone ($M_b = 68\ M_J$) makes a planetary formation history highly unlikely meaning that this BD likely formed via fragmentation. We also showed that it's orbital architecture is most consistent with a coplanar high-eccentricity migration mechanism. It's high eccentricity makes disk-driven migration improbable and the low stellar obliquity similarly rules out dynamically hot migration pathways that result in high-eccentricity tidal migration (e.g. planet-planet scattering, or Kozai-Lidov cycles).

We then zoomed out to examine the stellar obliquities of all transiting BDs for which these measurements have been made. While the sample is still small ($N = 11$), it clearly distinct from the stellar obliquity distribution of hot Jupiters, perhaps implying a distinct evolutionary pathway. To explore this, we qualitatively compared the stellar obliquity distributions of transiting hot Jupiters, warm Jupiters, and BDs. We found that the BDs more closely resembled warm Jupiter stellar obliquities, which have been shown to consistent with a dynamically quiescent migration mechansim. We suggested that this may imply a shared migration history where transiting BDs also migrate quiescently, and suggest paths forward for testing this hypothesis, including a systematic search for smaller planetary companions orbiting at separations near a transiting BD.

5.1.3 Chapter 4: 11 More Transiting BDs and Low-Mass Stars

In Chapter 4, we described the discovery and characterization of 11 new transiting BDs and low-mass stellar companions. We employed the same discovery and characterization techniques

discussed in Chapter 2 to homogeneously analyze each system, increasing the known transiting BD population 54 systems. Armed with a more statistically robust sample of transiting BDs, we performed a comparative analysis to the results of Ma & Ge (2014), citing that the bulk the recent transiting BD literature has claimed support for the 43 M_J transition proposed by Ma & Ge (2014). We showed for the first time that the transiting BD sample does not in fact support this 43 M_J transition by statistically analyzing transiting BD eccentricities and metallicities. Previous work had claimed that transiting BDs with $M_b < 43\ M_J$ were less eccentric than those with $M_b > 43\ M_J$ which supports the idea that it represents the transition from planetary to stellar formation. However, we explained that any truly astrophysical features in the eccentricity-companion mass distribution should also show up in eccentricity-mass ratio distribution since mass ratio is the more fundamental parameter that governs orbital architecture. We then showed that the eccentricity dichotomy is not present when plotted against mass-ratio and thus not indicative of a transition in formation mechanism. We also showed that there was no statistical difference in transiting BD metallicities above and below the 43 M_J threshold, providing even more evidence against this supposed transition.

Chapter 4 also presented a deeper characterization of a particularly interesting transiting BD: TOI-5882. This brown dwarf resides in the most barren part of the BD desert at $M_b = 22\ M_J$, and its host star displayed an anomalous amount of Li in its atmosphere. We estimated the strength of this Li feature by measuring the equivalent width of the of the 6707.8 Å absorption line. Since Li absorption features are typically associated with young stars, we followed up with deeper dive into the physical, spatial, and kinematic properties of the host star in order to determine the age of the star. We analyzed the rotation, local stellar neighborhood, kinematics, and other spectroscopic features of TOI-5882 in search of other signs of youth from which we could estimate the age of the system. However, we found that each of these features were not consistent with the young age suggested by the Li feature, and were instead more indicative of a older host star just beginning disembark from the main sequence. We ultimately suggested that these features may instead be due to the ingestion of planetary material by the evolving host star.

5.2 Future Work

We have shown in Chapter 3 how stellar obliquity can be a powerful tool for informing us about BD evolutionary histories. However, it remains difficult to make these inferences for the current sample of BDs with obliquity measurements due to the influence of tidal forces. Nearly every system measured so far have orbital periods $P < 10$ days where tidal realignment and recircularization are expected to erase the architectural signatures of formation and migration. The natural extension of this work is to push for more stellar obliquity measurements in systems where the influence of tides can be neglected. We conclude by outlining a path forward for these efforts.

First, we should aim to extend the current sample of transiting BDs stellar obliquity measurements to longer orbital periods. There are currently 8 suitable transiting BDs in the literature that are accessible to these measurements (i.e. orbital period > 10 days, and $V < 13.5$ mag). These longer period transiting systems are close enough that their transits are accessible from the ground yet distant enough that they have not undergone significant tidal realignment (Albrecht et al., 2012). By determining the sky-projected obliquity of their host stars, we can directly test whether the alignment trend observed for short-period brown dwarfs continues at longer periods. A well aligned sample in this regime would support the idea that transiting brown dwarfs migrate quiescently without being perturbed onto highly misaligned orbits. Any detection of significant misalignment, on the other hand, would be the first of its kind if found in a single star system and would indicate a more dynamically violent migration history. This result would contradict our current understanding of brown dwarf migration.

Next, we should attempt to disentangle BD migration from formation. To do this we need to target brown dwarf companions on wider orbits that have not undergone significant migration. We can soon do this by pursuing BDs that have been identified astrometrically in the upcoming Gaia DR4. Gaia's astrometry can directly detect the wobble of stars caused by orbiting companions, and DR4 (expected in December 2026) will extend the Gaia baseline to 66 months while providing epoch astrometry, radial velocities, and photometry for all sources. Holl et al. (2022) showed that Gaia will excel at detecting brown dwarfs in range of 100 - 1000 day orbital periods over its

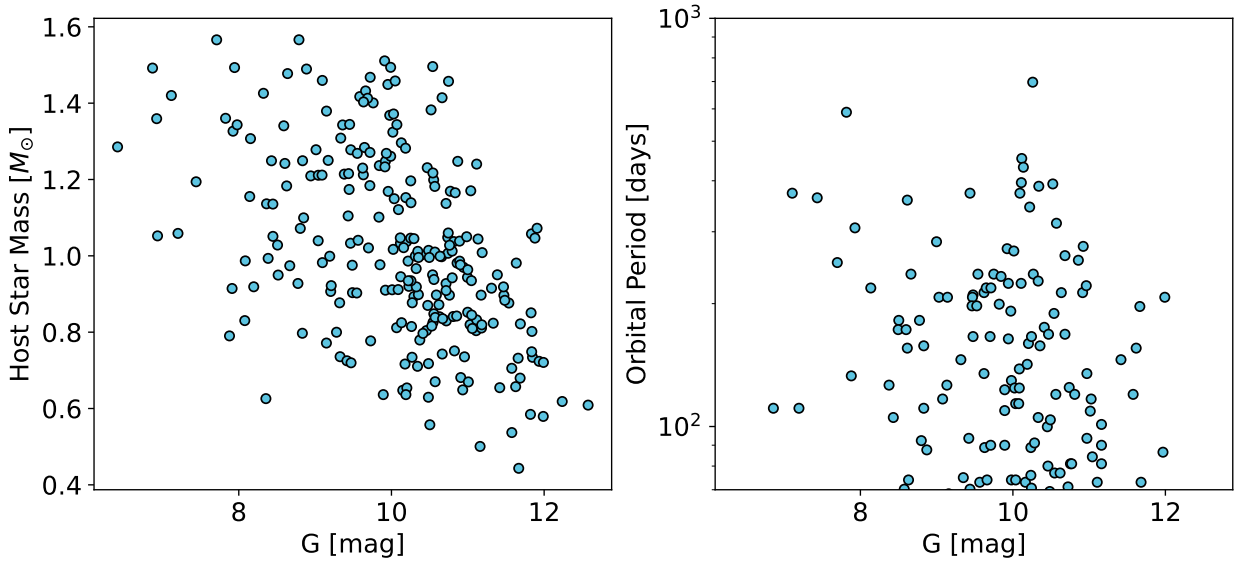

Figure 5.1 This figure adapted from Holl et al. (2022) depicts simulated brown dwarf companions that will be discovered and characterized by Gaia astrometry during its nominal 5 year mission (note: Gaia DR4 encompasses 66 months of data, slightly longer than the nominal mission predicted here). These simulated detections are also the systems that are predicted the highest quality astrometric solutions, precise enough to constrain the orbital parameters to better than 10%. **Left:** depicts this sample in host star mass versus brightness in G [mag]. **Right:** shows the same simulated detections in orbital period versus brightness in G [mag]. There will be ample brown dwarf companions around FGK type stars with orbital periods 100 – 1000 days in order to perform this work.

nominal 5 year mission (see; Figure 5.1). These brown dwarfs are too far from their stars to have undergone significant migration and thus their stellar obliquities are likely primordial. We could constrain the spin-orbit alignment in these systems by combining Gaia's orbital information with measurements of the host star's rotation axis (see; Fabrycky & Winn, 2009) in order to probe the primordial alignment of BDs. If the rotation axes of these BD host stars are aligned with their widely separated companions, it would suggest that BDs even at tens of AU generally form in the same plane as their star's circumstellar disk. On the other hand, frequent misalignments would imply formation with random orientations, as expected from turbulent cloud fragmentation.

Looking further ahead, upcoming (and ongoing) facilities promise substantial advances in BD science. The recently launched James Webb Space Telescope (JWST) will enable unprecedented detail for atmospheric studies of BDs, ideally allowing us to search for chemical tracers of formation. The Legacy Survey of Space and Time with the Vera Rubin Observatory will directly image

widely separated and isolated BDs with decade long baselines providing exquisite astrometrically constrained architectures, parallaxes, and proper motions enabling dynamical constraints on planetary and stellar formation mechanisms. The Nancy Grace Roman Space Telescope is predicted to discover hundreds of thousands of transiting planets (Wilson et al., 2023) and thousands of microlensing planets (Penny et al., 2019) through the Galactic Bulge Time-Domain Survey. These two samples will undoubtedly contain BDs enabling the first insights into BD demographics as a function of galactic position. Combined, these surveys and facilities represent a bright future for BD astronomy enabling deeper characterization of individual systems with facilities like JWST and more robust population level demographics with the ability of Gaia/Roman/Rubin to cultivate larger, more homogeneous BD populations. These advances will bring us even closer to a more complete understanding of the transition between planet-like and star-like formation.

BIBLIOGRAPHY

Abe, L., Gonçalves, I., Agabi, A., et al. 2013, A&A, 553, A49, doi: 10.1051/0004-6361/20122035110.48550/arXiv.1303.0973

Adams, F. C., & Laughlin, G. 2006, ApJ, 649, 1004, doi: 10.1086/506145

Adams, F. C., Ruden, S. P., & Shu, F. H. 1989, ApJ, 347, 959, doi: 10.1086/168187

Addison, B. C., Knudstrup, E., Wong, I., et al. 2021, AJ, 162, 292, doi: 10.3847/1538-3881/ac224e

Albrecht, S., Winn, J. N., Johnson, J. A., et al. 2012, ApJ, 757, 18, doi: 10.1088/0004-637X/757/1/18

Anderson, D. R., Temple, L. Y., Nielsen, L. D., et al. 2018, arXiv e-prints, arXiv:1809.04897. https://arxiv.org/abs/1809.04897

Andrews, J. J., Curtis, J. L., Chanamé, J., et al. 2022, AJ, 163, 275

Auvergne, M., Bodin, P., Boisnard, L., et al. 2009, A&A, 506, 411, doi: 10.1051/0004-6361/200810860

Bakos, G. Á., Torres, G., Pál, A., et al. 2010, ApJ, 710, 1724, doi: 10.1088/0004-637X/710/2/1724

Baraffe, I., Chabrier, G., Allard, F., & Hauschildt, P. H. 1998, A&A, 337, 403

—. 2002, A&A, 382, 563, doi: 10.1051/0004-6361:20011638

Baraffe, I., Chabrier, G., Barman, T. S., Allard, F., & Hauschildt, P. H. 2003, A&A, 402, 701, doi: 10.1051/0004-6361:20030252

Baranne, A., Queloz, D., Mayor, M., et al. 1996, A&AS, 119, 373

Barber, M. G., Mann, A. W., Bush, J. L., et al. 2022, arXiv e-prints, arXiv:2206.08383

Barnes, J. W. 2009, ApJ, 705, 683, doi: 10.1088/0004-637X/705/1/683

Barnes, S. A. 2003, ApJ, 586, 464

Bate, M. R. 2012, MNRAS, 419, 3115, doi: 10.1111/j.1365-2966.2011.19955.x

Bate, M. R., Lodato, G., & Pringle, J. E. 2010, MNRAS, 401, 1505, doi: 10.1111/j.1365-2966.2009.15773.x

Beatty, T. G., Morley, C. V., Curtis, J. L., et al. 2018, AJ, 156, 168, doi: 10.3847/1538-3881/aad697

Beatty, T. G., Collins, K. A., Fortney, J., et al. 2014, ApJ, 783, 112, doi: 10.1088/0004-637X/783/2/112

Bento, J., Hartman, J. D., Bakos, G. Á., et al. 2018, MNRAS, 477, 3406, doi: 10.1093/mnras/sty726

Bodenheimer, P., Lin, D. N. C., & Mardling, R. A. 2001, ApJ, 548, 466, doi: 10.1086/318667

Boksenberg, A., Evans, R. G., Fowler, R. G., et al. 1973, MNRAS, 163, 291, doi: 10.1093/mnras/163.3.291

Bonomo, A. S., Sozzetti, A., Santerne, A., et al. 2015, A&A, 575, A85, doi: 10.1051/0004-6361/201323042

Borucki, W. J., Koch, D., Basri, G., et al. 2010, Science, 327, 977, doi: 10.1126/science.1185402

Bouchy, F., Díaz, R. F., Hébrard, G., et al. 2013, A&A, 549, A49, doi: 10.1051/0004-6361/201219979

Bouchy, F., Hebrard, G., Udry, S., Delfosse, X., & Boisse, I. 2009, arXiv e-prints, arXiv:0907.3559, doi: 10.48550/arXiv.0907.3559

Bouchy, F., Deleuil, M., Guillot, T., et al. 2011, A&A, 525, A68, doi: 10.1051/0004-6361/201015276

Bouma, L. G., Palumbo, E. K., & Hillenbrand, L. A. 2023, ApJL, 947, L3, doi: 10.3847/2041-8213/acc589

Bowler, B. P., Blunt, S. C., & Nielsen, E. L. 2020, AJ, 159, 63, doi: 10.3847/1538-3881/ab5b11

Bowler, B. P., Tran, Q. H., Zhang, Z., et al. 2023, AJ, 165, 164, doi: 10.3847/1538-3881/acbd34

Brady, M., Bean, J. L., Stefánsson, G., et al. 2025, AJ, 169, 64, doi: 10.3847/1538-3881/ad9c66

Bressan, A., Marigo, P., Girardi, L., et al. 2012, MNRAS, 427, 127

Briceño, C., Calvet, N., Hernández, J., et al. 2019, AJ, 157, 85, doi: 10.3847/1538-3881/aaf79b

Brown, T. M., Baliber, N., Bianco, F. B., et al. 2013, PASP, 125, 1031, doi: 10.1086/673168

Buchhave, L. A., Bakos, G. Á., Hartman, J. D., et al. 2010, ApJ, 720, 1118, doi: 10.1088/0004-637X/720/2/1118

Buchhave, L. A., Latham, D. W., Carter, J. A., et al. 2011, ApJS, 197, 3, doi: 10.1088/0067-0049/197/1/3

Buchhave, L. A., Latham, D. W., Johansen, A., et al. 2012, Nature, 486, 375, doi: 10.1038/nature11121

Burgasser, A. J., Kirkpatrick, J. D., Brown, M. E., et al. 2002, ApJ, 564, 421, doi: 10.1086/324033

Burrows, A., Hubbard, W. B., Lunine, J. I., & Liebert, J. 2001, Reviews of Modern Physics, 73, 719, doi: 10.1103/RevModPhys.73.719

Burrows, A. S. 2014, Nature, 513, 345, doi: 10.1038/nature13782

Butler, R. P., Marcy, G. W., Williams, E., et al. 1996, PASP, 108, 500, doi: 10.1086/133755

Cañas, C. I., Bender, C. F., Mahadevan, S., et al. 2018, ApJL, 861, L4, doi: 10.3847/2041-8213/aacbc5

Caldwell, D. A., Tenenbaum, P., Twicken, J. D., et al. 2020, Research Notes of the American Astronomical Society, 4, 201, doi: 10.3847/2515-5172/abc9b3

Carmichael, T. W., Quinn, S. N., Mustill, A. J., et al. 2020, AJ, 160, 53, doi: 10.3847/1538-3881/ab9b84

Carmichael, T. W., Quinn, S. N., Zhou, G., et al. 2021, AJ, 161, 97, doi: 10.3847/1538-3881/abd4e1

Carmichael, T. W., Irwin, J. M., Murgas, F., et al. 2022, MNRAS, 514, 4944, doi: 10.1093/mnras/stac1666

Carmichael, T. W., Giacalone, S., Vowell, N., et al. 2025, arXiv e-prints, arXiv:2506.18971, doi: 10.48550/arXiv.2506.18971

Castelli, F., & Kurucz, R. L. 2003, in IAU Symposium, Vol. 210, Modelling of Stellar Atmospheres, ed. N. Piskunov, W. W. Weiss, & D. F. Gray, A20, doi: 10.48550/arXiv.astro-ph/0405087

Cayrel, R. 1988, in IAU Symposium, Vol. 132, The Impact of Very High S/N Spectroscopy on Stellar Physics, ed. G. Cayrel de Strobel & M. Spite, 345

Cegla, H. M., Lovis, C., Bourrier, V., et al. 2016, A&A, 588, A127, doi: 10.1051/0004-6361/201527794

Chabrier, G., Johansen, A., Janson, M., & Rafikov, R. 2014, in Protostars and Planets VI, ed. H. Beuther, R. S. Klessen, C. P. Dullemond, & T. Henning, 619–642, doi: 10.2458/azu_uapress_9780816531240-ch027

Chandrasekhar, S. 1939, An introduction to the study of stellar structure

Chatterjee, S., Ford, E. B., Matsumura, S., & Rasio, F. A. 2008, ApJ, 686, 580, doi: 10.1086/590227

Choi, J., Dotter, A., Conroy, C., et al. 2016, ApJ, 823, 102, doi: 10.3847/0004-637X/823/2/102

Ciardi, D. R., Beichman, C. A., Horch, E. P., & Howell, S. B. 2015, ApJ, 805, 16, doi: 10.1088/0004-637X/805/1/16

Claret, A. 2016, VizieR Online Data Catalog, J/A+A/600/A30

—. 2017, A&A, 600, A30, doi: 10.1051/0004-6361/201629705

Collier Cameron, A., Guenther, E., Smalley, B., et al. 2010, MNRAS, 407, 507, doi: 10.1111/j.1365-2966.2010.16922.x

Collins, K. A., Kielkopf, J. F., Stassun, K. G., & Hessman, F. V. 2017, AJ, 153, 77, doi: 10.3847/1538-3881/153/2/77

Collins, K. A., Collins, K. I., Pepper, J., et al. 2018, AJ, 156, 234, doi: 10.3847/1538-3881/aae582

Cooke, B. F., Pollacco, D., Almleaky, Y., et al. 2020, AJ, 159, 255, doi: 10.3847/1538-3881/ab88db

Cortés-Zuleta, P., Rojo, P., Wang, S., et al. 2020, A&A, 636, A98, doi: 10.1051/0004-6361/201936279

Cotten, T. H., & Song, I. 2016, ApJS, 225, 15, doi: 10.3847/0067-0049/225/1/15

Crane, J. D., Shectman, S. A., & Butler, R. P. 2006, in Society of Photo-Optical Instrumentation Engineers (SPIE) Conference Series, Vol. 6269, Ground-based and Airborne Instrumentation for Astronomy, ed. I. S. McLean & M. Iye, 626931, doi: 10.1117/12.672339

Crane, J. D., Shectman, S. A., Butler, R. P., et al. 2010, in Society of Photo-Optical Instrumentation Engineers (SPIE) Conference Series, Vol. 7735, Ground-based and Airborne Instrumentation for Astronomy III, ed. I. S. McLean, S. K. Ramsay, & H. Takami, 773553, doi: 10.1117/12.857792

Crane, J. D., Shectman, S. A., Butler, R. P., Thompson, I. B., & Burley, G. S. 2008, in Society of Photo-Optical Instrumentation Engineers (SPIE) Conference Series, Vol. 7014, Ground-based and Airborne Instrumentation for Astronomy II, ed. I. S. McLean & M. M. Casali, 701479, doi: 10.1117/12.789637

Cushing, M. C., Kirkpatrick, J. D., Gelino, C. R., et al. 2011, ApJ, 743, 50, doi: 10.1088/0004-637X/743/1/50

Cutri, R. M., Wright, E. L., T., C., & at al. 2012, VizieR Online Data Catalog, 2311, 0

Cutri, R. M., Skrutskie, M. F., van Dyk, S., et al. 2003, VizieR Online Data Catalog, 2246, 0

Dahm, S. E. 2015, ApJ, 813, 108

Dalba, P. A., Kane, S. R., Isaacson, H., et al. 2024, ApJS, 271, 16, doi: 10.3847/1538-4365/ad18c3

D'Angelo, G., Kley, W., & Henning, T. 2003, ApJ, 586, 540, doi: 10.1086/367555

David, T. J., Hillenbrand, L. A., Gillen, E., et al. 2019, ApJ, 872, 161, doi: 10.3847/1538-4357/aafe09

Davis, Y. T., Triaud, A. H. M. J., Freckelton, A. V., et al. 2024, MNRAS, 530, 2565, doi: 10.1093/mnras/stae842

Dawson, R. I., & Johnson, J. A. 2018, Annual Review of Astronomy and Astrophysics, 56, 175, doi: 10.1146/annurev-astro-081817-051853

Deleuil, M., Deeg, H. J., Alonso, R., et al. 2008, A&A, 491, 889, doi: 10.1051/0004-6361:200810625

Delfosse, X., Tinney, C. G., Forveille, T., et al. 1997, A&A, 327, L25

Donati, J.-F., Semel, M., Carter, B. D., Rees, D. E., & Collier Cameron, A. 1997, MNRAS, 291, 658, doi: 10.1093/mnras/291.4.658

Dong, J., Huang, C. X., Zhou, G., et al. 2022, ApJL, 926, L7, doi: 10.3847/2041-8213/ac4da0

Dorval, P., Talens, G. J. J., Otten, G. P. P. L., et al. 2020, A&A, 635, A60, doi: 10.1051/0004-6361/201935611

Dotter, A. 2016, ApJS, 222, 8, doi: 10.3847/0067-0049/222/1/8

Dotter, A., Chaboyer, B., Jevremović, D., et al. 2008, ApJS, 178, 89

Doyle, L., Cañas, C. I., Libby-Roberts, J. E., et al. 2025, MNRAS, 536, 3745, doi: 10.1093/mnras/stae2819

Earl, N., Tollerud, E., O'Steen, R., et al. 2022, astropy/specutils: v1.9.1, v1.9.1, Zenodo, doi: 10.5281/zenodo.7348235

Eastman, J., Gaudi, B. S., & Agol, E. 2013, PASP, 125, 83, doi: 10.1086/669497

Eastman, J. D., Diamond-Lowe, H., & Tayar, J. 2023, AJ, 166, 132, doi: 10.3847/1538-3881/aceda2

Eastman, J. D., Rodriguez, J. E., Agol, E., et al. 2019, arXiv e-prints, arXiv:1907.09480. https://arxiv.org/abs/1907.09480

Eberhardt, J., Hobson, M. J., Henning, T., et al. 2023, AJ, 166, 271, doi: 10.3847/1538-3881/ad06bc

El-Badry, K., Burdge, K. B., van Roestel, J., & Rodriguez, A. C. 2023, The Open Journal of Astrophysics, 6, 33, doi: 10.21105/astro.2307.15729

Esteves, L. J., De Mooij, E. J. W., & Jayawardhana, R. 2015, ApJ, 804, 150, doi: 10.1088/0004-637X/804/2/150

Fabrycky, D., & Tremaine, S. 2007, ApJ, 669, 1298, doi: 10.1086/521702

Fabrycky, D. C., & Winn, J. N. 2009, ApJ, 696, 1230, doi: 10.1088/0004-637X/696/2/1230

Fan, X., Knapp, G. R., Strauss, M. A., et al. 2000, AJ, 119, 928, doi: 10.1086/301224

Feiden, G. A., & Chaboyer, B. 2012, ApJ, 761, 30

Ferreira dos Santos, T., Rice, M., Wang, X.-Y., & Wang, S. 2024, AJ, 168, 145, doi: 10.3847/1538-3881/ad6b7f

Fischer, D. A., & Valenti, J. 2005, ApJ, 622, 1102, doi: 10.1086/428383

Foreman-Mackey, D., Hogg, D. W., Lang, D., & Goodman, J. 2013, PASP, 125, 306, doi: 10.1086/670067

Gaia Collaboration, Vallenari, A., Brown, A. G. A., et al. 2022, arXiv e-prints, arXiv:2208.00211. https://arxiv.org/abs/2208.00211

—. 2023, A&A, 674, A1, doi: 10.1051/0004-6361/202243940

Gaudi, B. S., Stassun, K. G., Collins, K. A., et al. 2017, Nature, 546, 514, doi: 10.1038/nature22392

Gavel, D., Kupke, R., Dillon, D., et al. 2014, in Society of Photo-Optical Instrumentation Engineers (SPIE) Conference Series, Vol. 9148, Adaptive Optics Systems IV, ed. E. Marchetti, L. M. Close, & J.-P. Vran, 914805, doi: 10.1117/12.2055256

Giacalone, S., Dressing, C. D., García Muñoz, A., et al. 2022, ApJL, 935, L10, doi: 10.3847/2041-8213/ac80f4

Giacalone, S., Dai, F., Zanazzi, J. J., et al. 2024, AJ, 168, 189, doi: 10.3847/1538-3881/ad785a

Gill, S., Ulmer-Moll, S., Wheatley, P. J., et al. 2022, MNRAS, 513, 1785, doi: 10.1093/mnras/stac798

Gillen, E., Hillenbrand, L. A., David, T. J., et al. 2017, ApJ, 849, 11, doi: 10.3847/1538-4357/aa84b3

Gonzalez, G. 1997, MNRAS, 285, 403, doi: 10.1093/mnras/285.2.403

Gray, D. F. 2005, The Observation and Analysis of Stellar Photospheres

Grether, D., & Lineweaver, C. H. 2006, ApJ, 640, 1051, doi: 10.1086/500161

Grieves, N., Bouchy, F., Lendl, M., et al. 2021, A&A, 652, A127, doi: 10.1051/0004-6361/202141145

Guerrero, N. M., Seager, S., Huang, C. X., et al. 2021, ApJS, 254, 39, doi: 10.3847/1538-4365/abefe1

Guillot, T. 2005, Annual Review of Earth and Planetary Sciences, 33, 493, doi: 10.1146/annurev.earth.32.101802.120325

—. 2010, A&A, 520, A27, doi: 10.1051/0004-6361/200913396

Guillot, T., & Morel, P. 1995, A&AS, 109, 109

Guillot, T., Abe, L., Agabi, A., et al. 2015, Astronomische Nachrichten, 336, 638, doi: 10.1002/asna.20151217410.48550/arXiv.1506.06009

Hattori, S., Foreman-Mackey, D., Hogg, D. W., et al. 2021, arXiv e-prints, arXiv:2106.15063

Hayward, T. L., Brandl, B., Pirger, B., et al. 2001, PASP, 113, 105, doi: 10.1086/317969

Heidari, N., Boisse, I., Hara, N. C., et al. 2024, A&A, 681, A55, doi: 10.1051/0004-6361/202347897

Heidari, N., Hébrard, G., Martioli, E., et al. 2025, A&A, 694, A36, doi: 10.1051/0004-6361/202451519

Hellier, C., Anderson, D. R., Barkaoui, K., et al. 2019, MNRAS, 490, 1479, doi: 10.1093/mnras/stz2713

Henderson, B. A., Casewell, S. L., Jordán, A., et al. 2024a, MNRAS, 533, 2823, doi: 10.1093/mnras/stae1940

Henderson, B. A., Casewell, S. L., Goad, M. R., et al. 2024b, MNRAS, 530, 318, doi: 10.1093/mnras/stae508

Hoeijmakers, H. J., Ehrenreich, D., Heng, K., et al. 2018, Nature, 560, 453, doi: 10.1038/s41586-018-0401-y

Høg, E., Fabricius, C., Makarov, V. V., et al. 2000, A&A, 355, L27

Hogg, D. W., Bovy, J., & Lang, D. 2010, arXiv e-prints, arXiv:1008.4686

Holl, B., Perryman, M., Lindegren, L., Segransan, D., & Raimbault, M. 2022, A&A, 661, A151, doi: 10.1051/0004-6361/201936393

Hooton, M. J., Hoyer, S., Kitzmann, D., et al. 2022, A&A, 658, A75, doi: 10.1051/0004-6361/202141645

Howell, S. B., Everett, M. E., Sherry, W., Horch, E., & Ciardi, D. R. 2011, AJ, 142, 19, doi: 10.1088/0004-6256/142/1/19

Howell, S. B., & Furlan, E. 2022, Frontiers in Astronomy and Space Sciences, 9, 871163, doi: 10.3389/fspas.2022.871163

Howell, S. B., Scott, N. J., Matson, R. A., et al. 2021, Frontiers in Astronomy and Space Sciences, 8, 165, doi: 10.3389/fspas.2021.696011

Howell, S. B., Sobeck, C., Haas, M., et al. 2014, PASP, 126, 398, doi: 10.1086/676406

Huang, C., Wu, Y., & Triaud, A. H. M. J. 2016, ApJ, 825, 98, doi: 10.3847/0004-637X/825/2/98

Huang, C. X., Vanderburg, A., Pál, A., et al. 2020a, Research Notes of the American Astronomical Society, 4, 204, doi: 10.3847/2515-5172/abca2e

—. 2020b, Research Notes of the American Astronomical Society, 4, 206, doi: 10.3847/2515-5172/abca2d

Jenkins, J. M., Twicken, J. D., McCauliff, S., et al. 2016, in Proc. SPIE, Vol. 9913, Software and Cyberinfrastructure for Astronomy IV, 99133E, doi: 10.1117/12.2233418

Johnson, M. C., Rodriguez, J. E., Zhou, G., et al. 2018, AJ, 155, 100, doi: 10.3847/1538-3881/aaa5af

Kipping, D. M. 2013, MNRAS, 435, 2152, doi: 10.1093/mnras/stt1435

Kirkpatrick, J. D., Beichman, C. A., & Skrutskie, M. F. 1997, ApJ, 476, 311, doi: 10.1086/303613

Kirkpatrick, J. D., Reid, I. N., Liebert, J., et al. 1999, ApJ, 519, 802, doi: 10.1086/307414

Kounkel, M., & Covey, K. 2019, AJ, 158, 122, doi: 10.3847/1538-3881/ab339a

Kozai, Y. 1962, AJ, 67, 591, doi: 10.1086/108790

Kraft, R. P. 1967, ApJ, 150, 551, doi: 10.1086/149359

Kratter, K., & Lodato, G. 2016, ARA&A, 54, 271, doi: 10.1146/annurev-astro-081915-023307

Kumar, S. S. 1963, ApJ, 137, 1121, doi: 10.1086/147589

Kunimoto, M., Huang, C., Tey, E., et al. 2021, Research Notes of the American Astronomical Society, 5, 234, doi: 10.3847/2515-5172/ac2ef0

Kunimoto, M., Daylan, T., Guerrero, N., et al. 2022, ApJS, 259, 33, doi: 10.3847/1538-4365/ac5688

Kupke, R., Gavel, D., Roskosi, C., et al. 2012, in Society of Photo-Optical Instrumentation Engineers (SPIE) Conference Series, Vol. 8447, Adaptive Optics Systems III, ed. B. L. Ellerbroek, E. Marchetti, & J.-P. Véran, 84473G, doi: 10.1117/12.926470

Kurucz, R. L. 1992, in IAU Symposium, Vol. 149, The Stellar Populations of Galaxies, ed. B. Barbuy & A. Renzini, 225

Lambert, M., Bender, C. F., Kanodia, S., et al. 2023, AJ, 165, 218, doi: 10.3847/1538-3881/acc651

Latham, D. W., Stefanik, R. P., Mazeh, T., Torres, G., & Carney, B. W. 1998, in Astronomical Society of the Pacific Conference Series, Vol. 134, Brown Dwarfs and Extrasolar Planets, ed. R. Rebolo, E. L. Martin, & M. R. Zapatero Osorio, 178

Lester, K. V., Matson, R. A., Howell, S. B., et al. 2021, AJ, 162, 75, doi: 10.3847/1538-3881/ac0d06

Li, J., & Lai, D. 2023, ApJ, 956, 17, doi: 10.3847/1538-4357/aced89

Lidov, M. L. 1962, Planet. Space Sci., 9, 719, doi: 10.1016/0032-0633(62)90129-0

Lightkurve Collaboration, Cardoso, J. V. d. M., Hedges, C., et al. 2018, Lightkurve: Kepler and TESS time series analysis in Python, Astrophysics Source Code Library. http://ascl.net/1812.013

Lindegren, L., Hernández, J., Bombrun, A., et al. 2018, A&A, 616, A2, doi: 10.1051/0004-6361/201832727

Lindegren, L., Bastian, U., Biermann, M., et al. 2021, A&A, 649, A4, doi: 10.1051/0004-6361/202039653

Lomb, N. R. 1976, Ap&SS, 39, 447, doi: 10.1007/BF00648343

Low, C., & Lynden-Bell, D. 1976, MNRAS, 176, 367, doi: 10.1093/mnras/176.2.367

Lund, M. B., Rodriguez, J. E., Zhou, G., et al. 2017, AJ, 154, 194, doi: 10.3847/1538-3881/aa8f95

Ma, B., & Ge, J. 2014, MNRAS, 439, 2781, doi: 10.1093/mnras/stu134

Mandel, K., & Agol, E. 2002, ApJL, 580, L171, doi: 10.1086/345520

Mann, A. W., Wood, M. L., Schmidt, S. P., et al. 2022, AJ, 163, 156

Marcy, G. W., Butler, R. P., Williams, E., et al. 1997, ApJ, 481, 926, doi: 10.1086/304088

Matson, R. A., Howell, S. B., Horch, E. P., & Everett, M. E. 2018, AJ, 156, 31, doi: 10.3847/1538-3881/aac778

Mayor, M., & Queloz, D. 1995, Nature, 378, 355, doi: 10.1038/378355a0

McGurk, R., Rockosi, C., Gavel, D., et al. 2014, in Society of Photo-Optical Instrumentation Engineers (SPIE) Conference Series, Vol. 9148, Adaptive Optics Systems IV, ed. E. Marchetti, L. M. Close, & J.-P. Vran, 91483A, doi: 10.1117/12.2057027

McKee, C. F., & Ostriker, E. C. 2007, ARA&A, 45, 565, doi: 10.1146/annurev.astro.45.051806.110602

McLaughlin, D. B. 1924, ApJ, 60, doi: 10.1086/142826

Moe, M., & Di Stefano, R. 2017, ApJS, 230, 15, doi: 10.3847/1538-4365/aa6fb6

Mordasini, C., Alibert, Y., & Benz, W. 2009, A&A, 501, 1139, doi: 10.1051/0004-6361/200810301

Mordasini, C., Alibert, Y., Benz, W., Klahr, H., & Henning, T. 2012, A&A, 541, A97, doi: 10.1051/0004-6361/201117350

Morton, T. D., Bryson, S. T., Coughlin, J. L., et al. 2016, ApJ, 822, 86, doi: 10.3847/0004-637X/822/2/86

Moutou, C., Bonomo, A. S., Bruno, G., et al. 2013, A&A, 558, L6, doi: 10.1051/0004-6361/201322201

Mugrauer, M., & Michel, K.-U. 2020, Astronomische Nachrichten, 341, 996, doi: 10.1002/asna.202013825

—. 2021, Astronomische Nachrichten, 342, 840, doi: 10.1002/asna.202113972

Narita, N., Fukui, A., Kusakabe, N., et al. 2019, Journal of Astronomical Telescopes, Instruments, and Systems, 5, 015001, doi: 10.1117/1.JATIS.5.1.015001

NASA Exoplanet Archive. 2022, Planetary Systems, Version: 2022-06-06 11:10, NExScI-Caltech/IPAC, doi: 10.26133/NEA12

Newton, E. R., Mann, A. W., Tofflemire, B. M., et al. 2019, ApJL, 880, L17, doi: 10.3847/2041-8213/ab2988

NExScI. 2022, Exoplanet Follow-up Observing Program Web Service, IPAC, doi: 10.26134/EXOFOP5

Nowak, G., Palle, E., Gandolfi, D., et al. 2017, AJ, 153, 131, doi: 10.3847/1538-3881/aa5cb6

Offner, S. S. R., Dunham, M. M., Lee, K. I., Arce, H. G., & Fielding, D. B. 2016, ApJL, 827, L11, doi: 10.3847/2041-8205/827/1/L11

Oppenheimer, B. R., Kulkarni, S. R., Matthews, K., & Nakajima, T. 1995, Science, 270, 1478, doi: 10.1126/science.270.5241.1478

Page, E., Pepper, J., Wright, D., et al. 2024, AJ, 167, 109, doi: 10.3847/1538-3881/ad1a18

Paredes, L. A., Henry, T. J., Quinn, S. N., et al. 2021, AJ, 162, 176, doi: 10.3847/1538-3881/ac082a

Parviainen, H., Gandolfi, D., Deleuil, M., et al. 2014, A&A, 562, A140, doi: 10.1051/0004-6361/201323049

Parviainen, H., Tingley, B., Deeg, H. J., et al. 2019, A&A, 630, A89, doi: 10.1051/0004-6361/201935709

Patel, J. A., & Espinoza, N. 2022, AJ, 163, 228, doi: 10.3847/1538-3881/ac5f55

Paxton, B., Bildsten, L., Dotter, A., et al. 2011, ApJS, 192, 3, doi: 10.1088/0067-0049/192/1/3

Paxton, B., Cantiello, M., Arras, P., et al. 2013, ApJS, 208, 4, doi: 10.1088/0067-0049/208/1/4

Paxton, B., Marchant, P., Schwab, J., et al. 2015, ApJS, 220, 15, doi: 10.1088/0067-0049/220/1/15

Penny, M. T., Gaudi, B. S., Kerins, E., et al. 2019, ApJS, 241, 3, doi: 10.3847/1538-4365/aafb69

Pepe, F., Mayor, M., Galland, F., et al. 2002, A&A, 388, 632, doi: 10.1051/0004-6361:20020433

Perruchot, S., Kohler, D., Bouchy, F., et al. 2008, in Society of Photo-Optical Instrumentation Engineers (SPIE) Conference Series, Vol. 7014, Ground-based and Airborne Instrumentation for Astronomy II, ed. I. S. McLean & M. M. Casali, 70140J, doi: 10.1117/12.787379

Petrovich, C. 2015, ApJ, 805, 75, doi: 10.1088/0004-637X/805/1/75

Phillips, M. W., Tremblin, P., Baraffe, I., et al. 2020, A&A, 637, A38, doi: 10.1051/0004-6361/201937381

Pollack, J. B., Hubickyj, O., Bodenheimer, P., et al. 1996, Icarus, 124, 62, doi: 10.1006/icar.1996.0190

Psaridi, A., Bouchy, F., Lendl, M., et al. 2022, A&A, 664, A94, doi: 10.1051/0004-6361/202243454

Quinn, S. N., White, R. J., Latham, D. W., et al. 2012, ApJL, 756, L33, doi: 10.1088/2041-

8205/756/2/L33

Rampalli, R., Agüeros, M. A., Curtis, J. L., et al. 2021, ApJ, 921, 167

Rasio, F. A., & Ford, E. B. 1996, Science, 274, 954, doi: 10.1126/science.274.5289.954

Rebolo, R., Zapatero Osorio, M. R., & Martín, E. L. 1995, Nature, 377, 129, doi: 10.1038/377129a0

Rebull, L. M., Stauffer, J. R., Bouvier, J., et al. 2016, AJ, 152, 113

Rees, M. J. 1976, MNRAS, 176, 483, doi: 10.1093/mnras/176.3.483

Reipurth, B., & Schneider, N. 2008, in Handbook of Star Forming Regions, Volume I, ed. B. Reipurth, Vol. 4, 36

Rice, M., Wang, S., & Laughlin, G. 2022a, ApJL, 926, L17, doi: 10.3847/2041-8213/ac502d

Rice, M., Wang, S., Wang, X.-Y., et al. 2022b, AJ, 164, 104, doi: 10.3847/1538-3881/ac8153

Richert, A. J. W., Getman, K. V., Feigelson, E. D., et al. 2018, MNRAS, 477, 5191, doi: 10.1093/mnras/sty949

Ricker, G. R., Winn, J. N., Vanderspek, R., et al. 2015, Journal of Astronomical Telescopes, Instruments, and Systems, 1, 014003, doi: 10.1117/1.JATIS.1.1.014003

Rodriguez, J. E., Quinn, S. N., Vanderburg, A., et al. 2023, MNRAS, 521, 2765, doi: 10.1093/mnras/stad595

Romanova, M. M., Koldoba, A. V., Ustyugova, G. V., Lai, D., & Lovelace, R. V. E. 2023, MNRAS, 523, 2832, doi: 10.1093/mnras/stad987

Rossiter, R. A. 1924, ApJ, 60, doi: 10.1086/142825

Rusznak, J., Wang, X.-Y., Rice, M., & Wang, S. 2025, ApJL, 983, L42, doi: 10.3847/2041-8213/adc129

Safonov, B. S., Lysenko, P. A., & Dodin, A. V. 2017, Astronomy Letters, 43, 344, doi: 10.1134/S1063773717050036

Santos, N. C., Israelian, G., Mayor, M., Rebolo, R., & Udry, S. 2003, A&A, 398, 363, doi: 10.1051/0004-6361:20021637

Saumon, D., & Marley, M. S. 2008, ApJ, 689, 1327, doi: 10.1086/592734

Schlafly, E. F., & Finkbeiner, D. P. 2011, ApJ, 737, 103, doi: 10.1088/0004-637X/737/2/103

Schlaufman, K. C. 2010, ApJ, 719, 602, doi: 10.1088/0004-637X/719/1/602

—. 2018, ApJ, 853, 37, doi: 10.3847/1538-4357/aa961c

Schlegel, D. J., Finkbeiner, D. P., & Davis, M. 1998, ApJ, 500, 525, doi: 10.1086/305772

Schmidt, S. P., Schlaufman, K. C., Ding, K., et al. 2023, AJ, 166, 225, doi: 10.3847/1538-3881/ad0135

Schulte, J., Rodriguez, J. E., Bieryla, A., et al. 2024, AJ, 168, 32, doi: 10.3847/1538-3881/ad4a57

Scott, N. J., Howell, S. B., Horch, E. P., & Everett, M. E. 2018, PASP, 130, 054502, doi: 10.1088/1538-3873/aab484

Scott, N. J., Howell, S. B., Gnilka, C. L., et al. 2021, Frontiers in Astronomy and Space Sciences, 8, 138, doi: 10.3389/fspas.2021.716560

Sebastian, D., Guenther, E. W., Deleuil, M., et al. 2022, MNRAS, doi: 10.1093/mnras/stac2131

Serna, J., Hernandez, J., Kounkel, M., et al. 2021, ApJ, 923, 177, doi: 10.3847/1538-4357/ac300a

Shporer, A., O'Rourke, J. G., Knutson, H. A., et al. 2014, ApJ, 788, 92, doi: 10.1088/0004-637X/788/1/92

Siverd, R. J., Beatty, T. G., Pepper, J., et al. 2012, ApJ, 761, 123, doi: 10.1088/0004-637X/761/2/123

Skrutskie, M. F., Cutri, R. M., Stiening, R., et al. 2006, AJ, 131, 1163, doi: 10.1086/498708

Smith, J. C., Stumpe, M. C., Van Cleve, J. E., et al. 2012, PASP, 124, 1000, doi: 10.1086/667697

Soderblom, D. R., Hillenbrand, L. A., Jeffries, R. D., Mamajek, E. E., & Naylor, T. 2014, in Protostars and Planets VI, ed. H. Beuther, R. S. Klessen, C. P. Dullemond, & T. Henning, 219–241, doi: 10.2458/azu_uapress_9780816531240-ch010

Southworth, J. 2011, MNRAS, 417, 2166, doi: 10.1111/j.1365-2966.2011.19399.x

Spiegel, D. S., Burrows, A., & Milsom, J. A. 2011, ApJ, 727, 57, doi: 10.1088/0004-637X/727/1/57

Stangret, M., Pallé, E., Casasayas-Barris, N., et al. 2021, A&A, 654, A73, doi: 10.1051/0004-6361/202040100

Stassun, K. G., Collins, K. A., & Gaudi, B. S. 2017, AJ, 153, 136, doi: 10.3847/1538-3881/aa5df3

Stassun, K. G., & Torres, G. 2016, AJ, 152, 180, doi: 10.3847/0004-6256/152/6/180

—. 2018, ApJ, 862, 61, doi: 10.3847/1538-4357/aacafc

—. 2021, ApJL, 907, L33, doi: 10.3847/2041-8213/abdaad

Stassun, K. G., Oelkers, R. J., Pepper, J., et al. 2018, AJ, 156, 102, doi: 10.3847/1538-3881/aad050

Stassun, K. G., Oelkers, R. J., Paegert, M., et al. 2019, AJ, 158, 138, doi: 10.3847/1538-3881/ab3467

Stevens, D. J., Gaudi, B. S., & Stassun, K. G. 2018, ApJ, 862, 53, doi: 10.3847/1538-4357/aaccf5

Stevens, D. J., Zhou, G., Johnson, M. C., et al. 2020, MNRAS, 499, 3775, doi: 10.1093/mnras/staa3142

Strakhov, I. A., Safonov, B. S., & Cheryasov, D. V. 2023, Astrophysical Bulletin, 78, 234, doi: 10.1134/S1990341323020104

Strauss, M. A., Fan, X., Gunn, J. E., et al. 1999, ApJL, 522, L61, doi: 10.1086/312218

Stumpe, M. C., Smith, J. C., Catanzarite, J. H., et al. 2014, PASP, 126, 100, doi: 10.1086/674989

Stumpe, M. C., Smith, J. C., Van Cleve, J. E., et al. 2012, PASP, 124, 985, doi: 10.1086/667698

Swayne, M. I., Maxted, P. F. L., Triaud, A. H. M. J., et al. 2024, MNRAS, 528, 5703, doi: 10.1093/mnras/stad3866

Swift, J. J., Andersen, K., Arculli, T., et al. 2022, PASP, 134, 035005, doi: 10.1088/1538-3873/ac5aca

Talens, G. J. J., Albrecht, S., Spronck, J. F. P., et al. 2017, A&A, 606, A73, doi: 10.1051/0004-6361/201731282

Tarter, J. 1975, Doctoral dissertation, University of California, Berkeley

Thompson, G. I., Nandy, K., Jamar, C., et al. 1978, Catalogue of stellar ultraviolet fluxes : a compilation of absolute stellar fluxes measured by the Sky Survey Telescope (S2/68) aboard the ESRO satellite TD-1 /

Thorngren, D. P., & Fortney, J. J. 2018, AJ, 155, 214, doi: 10.3847/1538-3881/aaba13

Tingley, B., Endl, M., Gazzano, J. C., et al. 2011, A&A, 528, A97, doi: 10.1051/0004-6361/201015480

Tofflemire, B. M., Rizzuto, A. C., Newton, E. R., et al. 2021, AJ, 161, 171

Tokovinin, A. 2018, PASP, 130, 035002, doi: 10.1088/1538-3873/aaa7d9

Tokovinin, A., Fischer, D. A., Bonati, M., et al. 2013, PASP, 125, 1336, doi: 10.1086/674012

Torres, G., Andersen, J., & Giménez, A. 2010, A&A Rev., 18, 67, doi: 10.1007/s00159-009-0025-1

Triaud, A. H. M. J. 2018, in Handbook of Exoplanets, ed. H. J. Deeg & J. A. Belmonte, 2, doi: 10.1007/978-3-319-55333-7_2

Triaud, A. H. M. J., Queloz, D., Bouchy, F., et al. 2009, A&A, 506, 377, doi: 10.1051/0004-6361/200911897

Triaud, A. H. M. J., Hebb, L., Anderson, D. R., et al. 2013, A&A, 549, A18, doi: 10.1051/0004-6361/201219643

Twicken, J. D., Catanzarite, J. H., Clarke, B. D., et al. 2018, PASP, 130, 064502, doi: 10.1088/1538-3873/aab694

Vanderburg, A., & Johnson, J. A. 2014, PASP, 126, 948, doi: 10.1086/678764

Vanderburg, A., Huang, C. X., Rodriguez, J. E., et al. 2019, ApJL, 881, L19, doi: 10.3847/2041-8213/ab322d

von Essen, C., Mallonn, M., Piette, A., et al. 2021, A&A, 648, A71, doi: 10.1051/0004-6361/202038524

Vowell, N., Rodriguez, J. E., Quinn, S. N., et al. 2023, AJ, 165, 268, doi: 10.3847/1538-3881/acd197

Vowell, N., Rodriguez, J. E., Latham, D. W., et al. 2025, arXiv e-prints, arXiv:2501.09795, doi: 10.48550/arXiv.2501.09795

Vowell, N., Dong, J., Rodriguez, J. E., et al. 2026, MNRAS, 545, staf2161, doi: 10.1093/mnras/staf2161

Šubjak, J., Sharma, R., Carmichael, T. W., et al. 2020, AJ, 159, 151, doi: 10.3847/1538-3881/ab7245

Wang, X.-Y., Rice, M., Wang, S., et al. 2024, ApJL, 973, L21, doi: 10.3847/2041-8213/ad7469

Whitworth, A. P., & Stamatellos, D. 2006, A&A, 458, 817, doi: 10.1051/0004-6361:20065806

Wilson, R. F., Barclay, T., Powell, B. P., et al. 2023, ApJS, 269, 5, doi: 10.3847/1538-4365/acf3df

Winn, J. N., Fabrycky, D., Albrecht, S., & Johnson, J. A. 2010a, ApJL, 718, L145, doi: 10.1088/2041-8205/718/2/L145

—. 2010b, ApJL, 718, L145, doi: 10.1088/2041-8205/718/2/L145

Wright, E. L., Eisenhardt, P. R. M., Mainzer, A. K., et al. 2010, AJ, 140, 1868, doi: 10.1088/0004-6256/140/6/1868

Wu, D.-H., Rice, M., & Wang, S. 2023, AJ, 165, 171, doi: 10.3847/1538-3881/acbf3f

Wu, Y., & Lithwick, Y. 2011a, ApJ, 735, 109, doi: 10.1088/0004-637X/735/2/109

—. 2011b, ApJ, 735, 109, doi: 10.1088/0004-637X/735/2/109

Yan, F., & Henning, T. 2018, Nature Astronomy, 2, 714, doi: 10.1038/s41550-018-0503-3

Yee, S. W., Winn, J. N., Hartman, J. D., et al. 2022, AJ, 164, 70, doi: 10.3847/1538-3881/ac73ff

Zahn, J. P. 1975, A&A, 41, 329

—. 1977, A&A, 57, 383

Zanazzi, J. J., Dewberry, J., & Chiang, E. 2024, ApJL, 967, L29, doi: 10.3847/2041-8213/ad4644

Zhou, G., Rodriguez, J. E., Collins, K. A., et al. 2016, AJ, 152, 136, doi: 10.3847/0004-6256/152/5/136

Zhou, G., Rodriguez, J. E., Vanderburg, A., et al. 2018, AJ, 156, 93, doi: 10.3847/1538-3881/aad085

Zhou, G., Huang, C. X., Bakos, G. Á., et al. 2019a, AJ, 158, 141, doi: 10.3847/1538-3881/ab36b5

Zhou, G., Bakos, G. Á., Bayliss, D., et al. 2019b, AJ, 157, 31, doi: 10.3847/1538-3881/aaf1bb

Zhou, G., Winn, J. N., Newton, E. R., et al. 2020, ApJL, 892, L21, doi: 10.3847/2041-8213/ab7d3c

Ziegler, C., Tokovinin, A., Briceño, C., et al. 2020, AJ, 159, 19, doi: 10.3847/1538-3881/ab55e9